Astronomy & Astrophysics manuscript no. output
January 21, 2026

Euclid preparation

6×2pt analysis of *Euclid*'s spectroscopic and photometric data sets

Euclid Collaboration: L. Paganin[1], M. Bonici[⋆2], C. Carbone[2], S. Camera[3,4,5], I. Tutusaus[6,7,8,9], S. Davini[10], J. Bel[11], S. Tosi[12,10,13], D. Sciotti[14,15,16], S. Di Domizio[12,10], I. Risso[1], G. Testera[10], D. Sapone[17], Z. Sakr[18,6,19], A. Amara[20], S. Andreon[13], N. Auricchio[21], C. Baccigalupi[22,23,24,25], M. Baldi[26,21,27], S. Bardelli[21], P. Battaglia[21], R. Bender[28,29], F. Bernardeau[30,31], A. Biviano[23,25], C. Bodendorf[28], D. Bonino[5], E. Branchini[12,10,13], M. Brescia[32,33,34], J. Brinchmann[35], V. Capobianco[5], V. F. Cardone[15,16], J. Carretero[36,37], S. Casas[38], M. Castellano[15], G. Castignani[39,21], S. Cavuoti[33,34], G. Cañas-Herrera[40,41], K. C. Chambers[42], A. Cimatti[43], C. Colodro-Conde[44], G. Congedo[45], C. J. Conselice[46], L. Conversi[47,48], Y. Copin[49], L. Corcione[5], A. Costille[50], F. Courbin[51], H. M. Courtois[52], M. Crocce[8,53], M. Cropper[54], A. Da Silva[55,56], H. Degaudenzi[57], G. De Lucia[23], A. M. Di Giorgio[58], J. Dinis[56,55], H. Dole[59], F. Dubath[57], C. A. J. Duncan[46,60], X. Dupac[48], S. Dusini[61], A. Ealet[49], S. Escoffier[62], M. Farina[58], R. Farinelli[21], S. Farrens[63], S. Ferriol[49], F. Finelli[21,64], M. Frailis[23], E. Franceschi[21], S. Galeotta[23], B. Garilli[⋆⋆2], K. George[29], W. Gillard[62], B. Gillis[45], C. Giocoli[21,65], J. Graciá-Carpio[28], A. Grazian[66], F. Grupp[28,29], L. Guzzo[67,13,68], S. V. H. Haugan[69], W. Holmes[70], I. Hook[71], F. Hormuth[72], A. Hornstrup[73,74], S. Ilić[75,76,6], K. Jahnke[77], B. Joachimi[78], E. Keihänen[79], S. Kermiche[62], A. Kiessling[70], M. Kilbinger[63], T. Kitching[54], B. Kubik[49], M. Kümmel[29], M. Kunz[7], H. Kurki-Suonio[80,81], S. Ligori[5], P. B. Lilje[69], V. Lindholm[80,81], I. Lloro[82], G. Mainetti[83], D. Maino[67,2,68], E. Maiorano[21], O. Mansutti[23], O. Marggraf[84], K. Markovic[70], M. Martinelli[15,16], N. Martinet[50], F. Marulli[39,21,27], R. Massey[85], H. J. McCracken[31], E. Medinaceli[21], S. Mei[86], Y. Mellier[⋆⋆⋆87,31], M. Meneghetti[21,27], E. Merlin[15], G. Meylan[51], M. Moresco[39,21], L. Moscardini[39,21,27], E. Munari[23], S.-M. Niemi[40], J. W. Nightingale[88,85], C. Padilla[36], S. Paltani[57], F. Pasian[23], K. Pedersen[89], W. J. Percival[90,91,92], V. Pettorino[63], S. Pires[63], G. Polenta[93], M. Poncet[76], L. A. Popa[94], L. Pozzetti[21], F. Raison[28], R. Rebolo[44,95], A. Renzi[96,61], J. Rhodes[70], G. Riccio[33], E. Romelli[23], M. Roncarelli[21], E. Rossetti[26], R. Saglia[29,28], B. Sartoris[29,23], P. Schneider[84], T. Schrabback[97], M. Scodeggio[2], A. Secroun[62], G. Seidel[77], S. Serrano[9,8,98], C. Sirignano[96,61], G. Sirri[27], L. Stanco[61], J.-L. Starck[63], J. Steinwagner[28], C. Surace[50], P. Tallada-Crespí[99,37], D. Tavagnacco[23], A. N. Taylor[45], I. Tereno[55,100], N. Tessore[78], S. Toft[74,101,102], R. Toledo-Moreo[103], F. Torradeflot[37,99], E. A. Valentijn[104], L. Valenziano[21,64], J. Valiviita[80,81], T. Vassallo[29,23], A. Veropalumbo[13,10], Y. Wang[105], J. Weller[29,28], A. Zacchei[23,25], G. Zamorani[21], J. Zoubian[62], E. Zucca[21], A. Boucaud[86], E. Bozzo[57], C. Burigana[106,64], M. Calabrese[107,2], D. Di Ferdinando[27], G. Fabbian[108,109], N. Mauri[43,27], V. Scottez[87,110], M. Tenti[27], M. Viel[25,23,22,24,111], M. Wiesmann[69], Y. Akrami[112,113], V. Allevato[33], S. Anselmi[61,96,114], M. Ballardini[115,116,21], A. Blanchard[6], S. Borgani[117,25,23,24], S. Bruton[118], R. Cabanac[6], A. Calabro[15], A. Cappi[21,119], C. S. Carvalho[100], T. Castro[23,24,25,111], S. Contarini[39,27,21], A. R. Cooray[120], J. Coupon[57], G. Desprez[121], A. Díaz-Sánchez[122], J. A. Escartin Vigo[28], P. G. Ferreira[60], I. Ferrero[69], F. Fornari[64], L. Gabarra[60], K. Ganga[86], J. García-Bellido[112], E. Gaztanaga[8,9,123], F. Giacomini[27], G. Gozaliasl[124,80], A. Gregorio[117,23,24], A. Hall[45], H. Hildebrandt[125], J. Hjorth[126], J. J. E. Kajava[127,128], V. Kansal[129,130,131], D. Karagiannis[132,133], C. C. Kirkpatrick[79], L. Legrand[7,134], A. Loureiro[135,136], J. Macias-Perez[137], G. Maggio[23], M. Magliocchetti[58], F. Mannucci[138], R. Maoli[14,15], C. J. A. P. Martins[139,35], S. Matthew[45], L. Maurin[59], R. B. Metcalf[39,21], M. Migliaccio[140,141], P. Monaco[117,23,24,25], G. Morgante[21], S. Nadathur[123], L. Patrizii[27], A. Pezzotta[28], V. Popa[94], C. Porciani[84], D. Potter[142], M. Pöntinen[80], P.-F. Rocci[59], M. Sahlén[143], A. Schneider[142], M. Schultheis[119], M. Sereno[21,27], C. Tao[62], R. Teyssier[144], A. Troja[96,61], M. Tucci[57], C. Valieri[27], D. Vergani[21], G. Verza[145,108], and P. Vielzeuf[62]

(Affiliations can be found after the references)

January 21, 2026

ABSTRACT

Aims. In this paper we present cosmological parameter forecasts for the so-called *Euclid* 6×2pt statistics, which include the galaxy clustering and weak lensing main probes together with previously neglected cross-covariance and cross-correlation signals between imaging/photometric and spectroscopic data. The aim is understanding the impact of such cross-terms on the expected *Euclid* performance.

Methods. We adopt the Fisher information matrix approach to produce 6×2pt cosmological forecasts from *Euclid*, considering two different techniques: the so-called *harmonic* and *hybrid* approaches, respectively. In the first, we treat all the different *Euclid* probes in the same way, i.e., we consider only angular 2pt-statistics for spectroscopic and photometric galaxy distributions, as well as for weak lensing, fully analysing all their possible cross-covariances and cross-correlations in the spherical harmonic domain. In the second, thanks to lessons learnt from the harmonic approach, we do not account for negligible cross-covariances between the 3D spectroscopic galaxy distribution and the 2D photometric/imaging data, but consider the combination of their cross-correlation with the auto-correlation signals.
Results. We find that both cross-covariances and cross-correlation signals between the two *Euclid* main probes, i.e., the spectroscopic galaxy sample and the photometric/imaging data, have a negligible impact on the cosmological parameter constraints and, therefore, on the *Euclid* performance. In the case of the hybrid approach, we attribute this result to the effect of the cross-correlation between weak lensing and photometric data, which is dominant with respect to other cross-correlation signals, and to the better performance of the full anisotropic 3D spectroscopic galaxy clustering with respect to the projected one. In the case of the 2D harmonic approach, we attribute this result to two main theoretical limitations of the 2D projected statistics implemented in this work according to the analysis of official *Euclid* forecasts: the high shot noise and the limited redshift range of the spectroscopic sample, with respect to the photometric one, together with the suppression of radial information from subdominant contributions such as redshift-space distortions and lensing magnification. Therefore, our analysis suggests that 2D and 3D *Euclid* data can be safely treated as independent, with a great saving in computational resources.

Key words. galaxy clustering–weak lensing–*Euclid* survey

1. Introduction

Euclid is a medium-sized ESA mission devoted to the investigation of the nature of dark matter (DM) and dark energy (DE) and the study of the galaxy formation and evolution (Laureijs et al. 2011; Euclid Collaboration: Mellier et al. 2024). The *Euclid* satellite was launched on July 1 2023 and will observe about one third of the sky, performing one of the largest galaxy surveys ever made. It will probe the last 10 billion years of the Universe expansion history via its main cosmological probes which are weak lensing (WL) and galaxy clustering (GC). Through WL measurements it is possible to probe the matter distribution of the Universe, as WL represents the slight deformation of galaxy images induced by the gravitational potential produced by such a distribution. GC consists in the determination of the statistical properties of the distribution of galaxies, the so-called *dark matter tracers*. In particular, it is characterized by the so-called baryon acoustic oscillations (BAO), whose scale can be adopted as a *standard ruler* and used to constrain the expansion rate of the Universe in different redshift bins. *Euclid* will study these probes with two instruments: the Visible Imager (VIS) (Cropper et al. 2016; Euclid Collaboration: Jahnke et al. 2024) and the Near-Infrared Spectro-Photometer (NISP) (Maciaszek et al. 2022; Euclid Collaboration: Cropper et al. 2024). VIS will provide high resolution images of around 1.5 billion galaxies for weak lensing measurements. NISP, used in the photometric mode, will allow measurements of the photometric redshifts of the same galaxies observed with VIS, when combined with ground-based photometry. When used in the spectroscopic mode, NISP will measure the spectroscopic redshifts of around 20 million Hα-emitting galaxies, with a precision better than a factor of 50 with respect to the photometric redshift determination. *Euclid* will therefore produce two galaxy samples, a photometric and a spectroscopic one. In this sense, the GC probe can be split into photometric galaxy clustering (GC_{ph}) and spectroscopic galaxy clustering (GC_{sp}). GC_{sp} and the so-called *Euclid* 3×2pt statistics (composed of WL, GC_{ph} and their cross-correlation) represent the two main probes of *Euclid*.

In this work, we present *Euclid* cosmological parameter forecasts which include the cross-correlations between GC_{sp} and 3×2pt statistics. The data analysis of the survey needs, in fact, to be accurately planned, and to this aim, pre-data forecasts of the expected scientific performance are needed. In a previous official *Euclid* forecast (Euclid Collaboration: Blanchard et al. 2020, hereafter 'EP-VII') it was shown that the cross-correlation (XC) between WL and GC_{ph} significantly improves the *Euclid* constraints on cosmological parameters. The aim of this work is to extend previous analyses which neglected the cross-correlations between the imaging/photometric probes and the spectroscopic probe, in order to understand their impact on the expected constraints of *Euclid*. In particular, we include the cross-correlations between GC_{sp} and GC_{ph} and between GC_{sp} and WL, which defines the so-called *Euclid* 6×2pt statistics, forecasting the impact of these cross-correlations on the *Euclid* performance. Several works in the literature have investigated how to analyze and combine photometric and spectroscopic surveys, studying different approaches to minimizing information loss (Asorey et al. 2012; Eriksen & Gaztanaga 2015; Joudaki et al. 2018; Camera et al. 2018; Loureiro et al. 2019; Grasshorn Gebhardt & Jeong 2020; Taylor et al. 2022). Recently, Taylor & Markovič (2022) also studied theoretical modeling of the cross-covariance between photometric and spectroscopic probes and their impact on the forecast of measurements of cosmological parameters.

This paper is organized as follows. In Sect. 2 we describe in detail the adopted modeling of the GC_{sp}, GC_{ph} and WL observables. In Sect. 3 we present the Fisher information matrix approach implemented to produce our 6×2pt cosmological parameter forecasts from *Euclid*; we adopt two different techniques: the so-called *harmonic* and *hybrid* approaches which we describe in the following. In Sect. 4 we present the results, and finally we draw our conclusions.

2. Cosmological model and observables

In this forecast the cosmological model investigated is a flat w_0w_aCDM cosmology. The DE equation of state is described by the CPL parameterization (Linder 2002; Chevallier & Polarski 2001)

$$w_{\rm DE}(z) = w_0 + w_a \frac{z}{1+z} , \quad (1)$$

and the Hubble factor hence takes the form

$$\frac{H^2(z)}{H_0^2} = \Omega_{\rm m}(1+z)^3 + (1-\Omega_{\rm m})(1+z)^{3(1+w_0+w_a)} \, {\rm e}^{-3w_a z/(1+z)} , \quad (2)$$

where $\Omega_{\rm m}$ denotes the present-day matter density parameter, w_0 represents the current value of the DE equation of state, and w_a describes its redshift-dependent evolution. The other cosmological parameters involved in this analysis are $\Omega_{\rm b}$, the present-day

⋆ e-mail: mbonici@uwaterloo.ca
⋆⋆ Deceased
⋆⋆⋆ Deceased

matter density, h, the reduced Hubble constant, n_s, the tilt of the primordial density fluctuations, σ_8, the matter fluctuations on a scale of $8\,h^{-1}$ Mpc, and M_ν, the sum of the neutrino mass eigenstates; they are summarized in Table 1, where the values in the reference cosmology are reported. The probes considered in this forecast are: the weak lensing (WL), the photometric galaxy clustering (GC_{ph}), and the spectroscopic galaxy clustering (GC_{sp}). For the WL and GC_{ph} probes, the observable employed is the tomographic angular power spectrum $C_{ij}(\ell)$. For the GC_{sp} probe, both the usual power spectrum in Fourier space and the harmonic power spectrum have been considered as observables. The Fourier power spectrum approach is the same followed as in EP-VII and briefly summarized in Sect. 2.3.

An angular power spectrum is essentially the harmonic transform of a two-point angular correlation function. Each cosmological probe A (in a given redshift bin) can be associated with a field $f^A(\hat{n})$ projected on the sky, which can be expanded in the spherical harmonics orthonormal basis $Y_{\ell m}$[1],

$$f^A(\hat{n}) = \sum_{\ell=0}^{\infty} \sum_{m=-\ell}^{\ell} a^A_{\ell m}\, Y_{\ell m}(\hat{n}) \,. \tag{3}$$

The $a^A_{\ell m}$ are the coefficients of the f^A spherical harmonics transform,

$$a^A_{\ell m} = \int \mathrm{d}\Omega\, Y^*_{\ell m}(\hat{n})\, f^A(\hat{n}) \,. \tag{4}$$

This forecast employs 10 tomographic redshift bins for the WL and GC_{ph} probes, and 4 bins for the GC_{sp} probe. The tomographic angular correlation between the probe A, at the redshift bin i (A_i), and the probe B, at the redshift bin j (B_j), is then defined as the implicit relation

$$\left\langle a^{Ai}_{\ell m} \left(a^{Bj}_{\ell' m'}\right)^* \right\rangle = C^{AB}_{ij}(\ell)\, \delta_{\ell\ell'}\, \delta_{mm'} \,, \tag{5}$$

where the angular brackets denote the theoretical expectation value.

In this forecast, we compute the angular power spectra following the Limber approximation (Kaiser 1992),

$$C^{AB}_{ij}(\ell) \simeq \int_{z_{\min}}^{z_{\max}} \frac{c\,\mathrm{d}z}{H(z)} \frac{W^A_i(z)\, W^B_j(z)}{r^2(z)} P_{\delta\delta}\left[k = \frac{\ell + 1/2}{r(z)}, z\right] \,, \tag{6}$$

where c is the speed of light, $r(z)$ is the radial comoving distance for a flat cosmology, W^A_i is the weight (or window) function for the probe A in the i-th bin, k is the wave number, and $P_{\delta\delta}$ is the total matter power spectrum. The power spectra are the same used in EP-VII, obtained from the `CAMB` Boltzmann code. The nonlinear correction model employed in $P_{\delta\delta}$ is a revised version of the `halofit` recipe (Takahashi et al. 2012), modified to correctly consider the massive neutrinos contributions (Bird et al. 2012).

The functional form of the weight function W^A_i depends on the probe A. The weight functions for the probes considered in the forecast are shown in Fig. 1.

The fundamental ingredient for the computation of W^A_i is the redshift distribution per unit solid angle, $\mathrm{d}N^A(z)/\mathrm{d}z/\mathrm{d}\Omega$. The redshift distribution has been modeled analytically for the WL and GC_{ph} probes, and obtained via simulations for the GC_{sp} probe.

[1] For an all-sky analysis, the spherical harmonics are replaced by the spin-spherical harmonics (Stebbins 1996).

The normalized redshift density of the probe A in the i-th bin can be computed from the redshift distribution as

$$\tilde{n}^A_i(z) = \int_{z_i^-}^{z_i^+} \mathrm{d}z_\mathrm{p}\, \frac{\mathrm{d}N^A}{\mathrm{d}z\,\mathrm{d}\Omega}(z)\, p_A\left(z_\mathrm{p}|z\right) \,, \tag{7}$$

$$n^A_i(z) = \tilde{n}^A_i(z) \left[\int_{z_{\min}}^{z_{\max}} \mathrm{d}z\, \tilde{n}^A_i(z)\right]^{-1} \,, \tag{8}$$

where the function $p_A(z_\mathrm{p}|z)$ is the probability that a galaxy with true redshift z will be measured with a redshift z_p.

Formally, the redshift integration range extends from $z_{\min} = 0$ to $z_{\max} = +\infty$; however, given the shape of the integrand functions, the integration range has been truncated at $z_{\min} = 0.001$ and $z_{\max} = 3$ in this work. The tomographic bin edges z_i^- and z_i^+ for WL, GC_{ph}, and GC_{sp} are reported in Table 2.

This probability distribution $p_A(z_\mathrm{p}|z)$ models the redshift measurement errors for the probe A. The model chosen is the same of EP-VII:

$$\begin{aligned} p_A(z_\mathrm{p}|z) = {} & \frac{1 - f_\mathrm{out}}{\sqrt{2\,\pi}\,(1+z)\,\sigma_\mathrm{b}} \exp\left\{-\frac{1}{2}\left[\frac{z - c_\mathrm{b}\, z_\mathrm{p} - z_\mathrm{b}}{(1+z)\,\sigma_\mathrm{b}}\right]^2\right\} \\ & + \frac{f_\mathrm{out}}{\sqrt{2\,\pi}\,(1+z)\,\sigma_\mathrm{o}} \exp\left\{-\frac{1}{2}\left[\frac{z - c_\mathrm{o}\, z_\mathrm{p} - z_0}{(1+z)\,\sigma_\mathrm{o}}\right]^2\right\} \,. \end{aligned} \tag{9}$$

This model includes multiplicative and additive biases in the redshift determination, both for a fraction $(1 - f_\mathrm{out})$ of sources with well measured redshifts, and for a fraction (f_out) of catastrophic outliers, i.e., galaxies with severely incorrect estimate of the redshift. Different parameters of f_out and the biases have been used, depending on whether the redshift measurement is photometric or spectroscopic; in particular, f_out is taken to be zero for GC_{sp}, $\sigma_\mathrm{b} = 0.05$ for GC_{ph}, and $\sigma_\mathrm{b} = 0.001$ for GC_{sp}. The values of the parameters for $p_A(z_\mathrm{p}|z)$, which are kept fixed in our analysis, are summarized in Table 3.

The (true) redshift distribution of the photometric samples is modeled as in the *Euclid* redbook (Laureijs et al. 2011)

$$\frac{\mathrm{d}N^\mathrm{ph}}{\mathrm{d}z\,\mathrm{d}\Omega}(z) = N_0^\mathrm{ph} \left(\frac{z}{z_0}\right)^2 \exp\left[-\left(\frac{z}{z_0}\right)^{3/2}\right] \,, \tag{10}$$

where $z_0 = 0.9/\sqrt{2}$ and the normalization factor N_0^ph is chosen such that the surface density of galaxies is equal to 30 galaxies per square arcminute, corresponding to an expected total number of galaxies of about 1.6×10^9.

In the next subsections we give a short description of the probes involved in this analysis and their theoretical modeling.

2.1. Weak lensing

The gravitational field of large-scale cosmic structure deflects the path of light rays emitted by distant galaxies, distorting the images of the galaxies detected by the observers (Kaiser et al. 2000; Bacon et al. 2000; Kitching et al. 2017; Lemos et al. 2017). At the linear level these distortions can be decomposed locally into convergence κ and a (complex) shear γ, which are respectively related to the size and shape distortion of the image.

In this work we only consider the shear signal γ, following EP-VII. The corresponding weight function for cosmic shear in Eq. (6) is

$$W^\gamma_i(z) = \frac{3}{2} \left(\frac{H_0}{c}\right)^2 \Omega_\mathrm{m}\,(1+z)\, r(z) \int_z^{z_{\max}} \mathrm{d}z'\, n^\mathrm{ph}_i(z')\, \frac{r(z') - r(z)}{r(z')} \,.$$

Table 1: Values of the cosmological parameters considered of the reference cosmology.

Parameter	Ω_b	Ω_m	w_0	w_a	h	n_s	σ_8	M_ν[eV]
Fiducial value	0.05	0.32	−1	0	0.67	0.96	0.816	0.06

Notes. All the parameters are let free to vary except for the sum of the neutrino masses, which has been fixed to its reference value $M_\nu = 0.06\,\mathrm{eV}$.

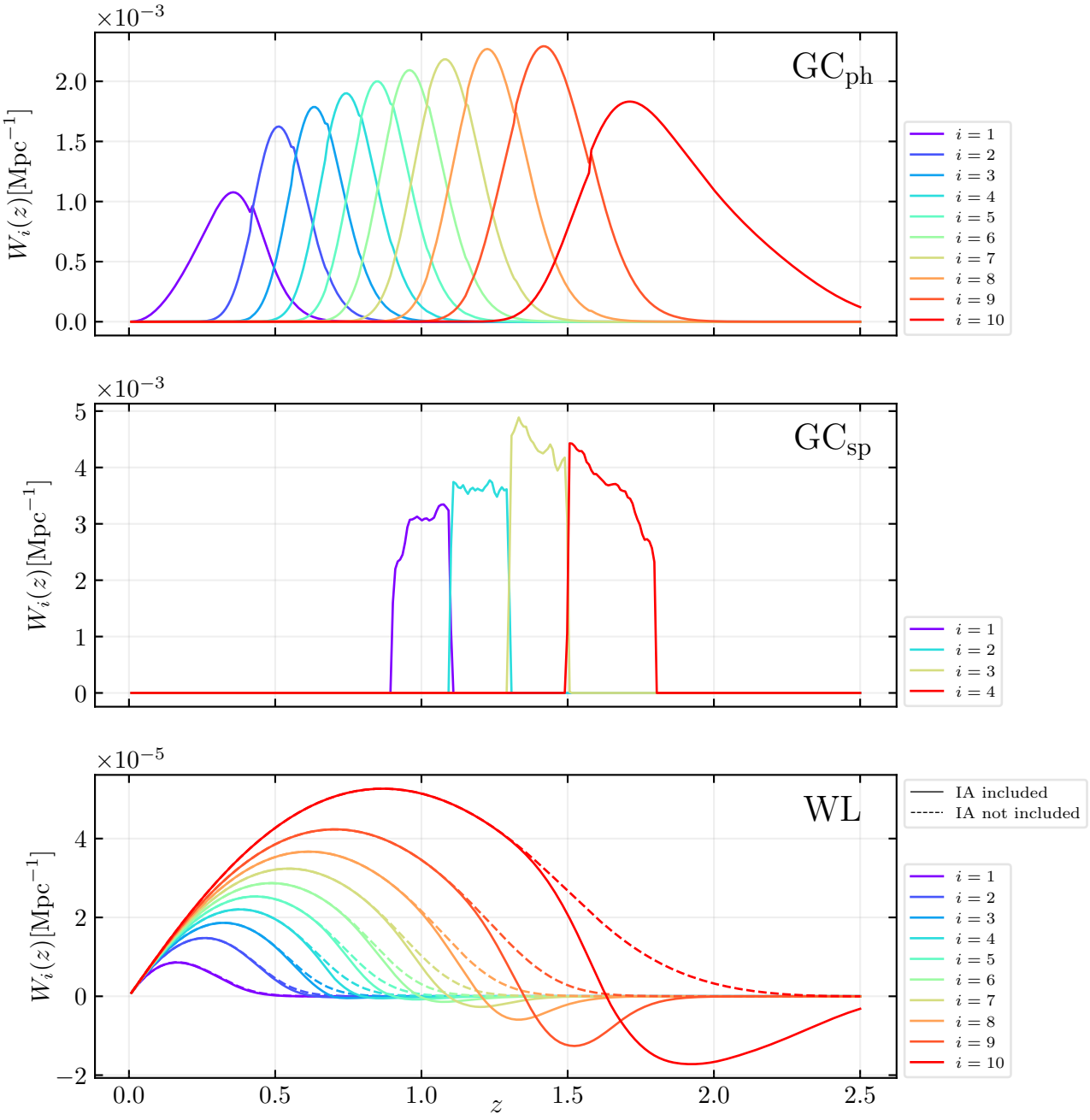

Fig. 1: Weight functions for the three probes considered in the forecast. For WL at high redshift bins, the weight function Eq. (12) (solid line) becomes negative, due to the contribution of intrinsic alignment (IA). The shear weight function Eq. (11) (dashed line) remains instead always positive as it should be.

(11)

The integral makes it clear that weak lensing is a cumulative effect: the detected shapes of galaxies are influenced by all the matter along the line of sight.

The forecast also includes the intrinsic alignment (IA), which is one of the main observable effects altering weak lensing measurements (Joachimi et al. 2015; Kiessling et al. 2015; Kirk et al. 2015). IA refers to the alignments of nearby galaxies caused by tidal interactions which occur during galaxy formation and evo-

Table 2: Tomographic bin edges and galaxy biases.

z_i^-	0.001	0.418	0.560	0.678	0.789	0.900	1.019	1.155	1.324	1.576
z_i^+	0.418	0.560	0.678	0.789	0.900	1.019	1.155	1.324	1.576	2.500
$b_i^{\rm ph}$	1.100	1.220	1.272	1.317	1.358	1.400	1.445	1.497	1.565	1.743

z_i^-	0.90	1.10	1.30	1.50
z_i^+	1.10	1.30	1.50	1.80
$b_i^{\rm sp}$	1.46	1.61	1.75	1.90

Notes. The left table shows the tomographic bin edges for weak lensing (WL) and photometric galaxy clustering ($\mathrm{GC_{ph}}$), while the right table shows the spectroscopic galaxy clustering ($\mathrm{GC_{sp}}$) bin edges. The corresponding galaxy biases for photometric ($b_i^{\rm ph}$) and spectroscopic ($b_i^{\rm sp}$) galaxy clustering are also reported.

Table 3: Parameters for the photometric redshift probability distributions.

probe	$c_{\rm b}$	$z_{\rm b}$	$\sigma_{\rm b}$	$c_{\rm o}$	$z_{\rm o}$	$\sigma_{\rm o}$	$f_{\rm out}$
WL, $\mathrm{GC_{ph}}$	1.0	0.0	0.050	1.0	0.1	0.05	0.1
$\mathrm{GC_{sp}}$	1.0	0.0	0.001	–	–	–	0

Notes. Values of the parameters adopted for the probability distributions $p_A(z_{\rm p}|z)$ defined in Eq. (9). The uncertainty $\sigma_{\rm b}$ on the correctly measured (not catastrophic) redshifts has been chosen from the *Euclid* design requirements (Laureijs et al. 2011). For $\mathrm{GC_{sp}}$ the outlier parameters are not reported since they are irrelevant, being the outliers fraction $f_{\rm out} = 0$.

lution. This produces spurious correlations in addition to those due to cosmic shear. The IA effect can be included in the lensing angular power spectrum. A possible way is by using the extended nonlinear alignment model (Bridle & King 2007) which consists of the following addition to the cosmic shear weight function

$$W_i^{\rm wl}(z) = W_i^{\gamma}(z) - \mathcal{A}_{\rm IA}\, C_{\rm IA}\, \Omega_{\rm m} \frac{H(z)\,\mathcal{F}_{\rm IA}(z)}{D(z)\,c}\, n_i^{\rm ph}(z)\,. \tag{12}$$

In the above equation, $D(z)$ is the linear scale-independent growth factor. The function $\mathcal{F}_{\rm IA}$ is defined as

$$\mathcal{F}_{\rm IA}(z) = (1+z)^{\eta_{\rm IA}} \left[\frac{\langle L\rangle(z)}{L_\star(z)}\right]^{\beta_{\rm IA}}\,, \tag{13}$$

where $\langle L\rangle(z)$ and $L_\star(z)$ are the mean and characteristic luminosity functions respectively. The intrinsic alignment parameters $\mathcal{A}_{\rm IA}, \eta_{\rm IA}, \beta_{\rm IA}$ are treated as nuisance parameters in the analysis. The reference values for the IA parameters are the same as in EP-VII, namely $\{\mathcal{A}_{\rm IA} = 1.72, \eta_{\rm IA} = -0.41, \beta_{\rm IA} = 2.17\}$. The parameter $C_{\rm IA} = 0.0134$ is fixed, since it is completely degenerate with $\mathcal{A}_{\rm IA}$.

2.2. Photometric galaxy clustering

The Galaxy Clustering probes exploit the statistical properties of the galaxy distribution. For the $\mathrm{GC_{ph}}$ probe, $W_i^{\rm ph}(z)$ in Eq. (6) is the galaxy clustering weight function

$$W_i^{\rm ph}(z) = b^{\rm ph}(z)\,\frac{H(z)}{c}\,n_i^{\rm ph}(z)\,, \tag{14}$$

where b is the galaxy bias and $n_i^{\rm ph}(z)$ is defined through Eqs. (8) and (10).

Galaxies are biased tracers of the dark matter distribution; the former are related to the latter through the galaxy bias b:

$$\delta^{\rm g}(k,z) = b(z)\,\delta(k,z)\,, \tag{15}$$

with k being the wavenumber. In general the galaxy bias is a function of z and k, but in this work the k-dependence has been neglected, following the treatment of EP-VII. Moreover, as in EP-VII, we neglect subdominant contributions to clustering such as *redshift-space distortions* (RSD) and lensing magnification.

The redshift evolution of the galaxy bias is modeled as in EP-VII: for $\mathrm{GC_{ph}}$ a piecewise function is employed such that

$$b^{\rm ph}(z) = b_i^{\rm ph} = \sqrt{1+\bar{z}_i}\,, \qquad z_i^- < z < z_i^+\,, \tag{16}$$

where $\bar{z}_i = (z_i^- + z_i^+)/2$ is the mean redshift of the ith bin. Such bin edges, z_i^- and z_i^+, are defined in Table 2, where we also report the values of $b_i^{\rm ph}$. Following the approach of EP-VII, we marginalize over their values.

2.3. Spectroscopic galaxy clustering

The *Euclid* mission will employ both its photometric and spectroscopic samples to study galaxy clustering. Spectroscopic redshift determination in *Euclid* is based on Hα-emitting galaxies in the redshift range $z \in [0.9, 1.8]$. The total number of galaxies in the spectroscopic sample is about 2×10^7, which is smaller by a factor ~ 80 than the total number of photometric galaxies. Despite the lack of counting statistics, a sample based on precise spectroscopic redshifts allows us to go beyond projected 2D statistics, exploiting the information in the full 3D galaxy distribution.

The spectroscopic galaxy clustering is usually treated by using the 3D Fourier galaxy power spectrum. In this work, we also treated the $\mathrm{GC_{sp}}$ probe in the harmonic domain.

The 3D Fourier approach can model several physical effects, such as RSD, the Alcock-Paczynski (AP) projection effects, the nonlinear damping of the Baryon Acoustic Oscillations (BAO), and the residual shot noise. The full nonlinear model for the 3D power spectrum of the Hα galaxies employed in *Euclid* is described in Sec. 3.2 of EP-VII.

The harmonic approach is based on Eq. (6), with the $\mathrm{GC_{sp}}$ weight function given by

$$W_i^{\rm sp}(z) = b^{\rm sp}(z)\,\frac{H(z)}{c}\,n_i^{\rm sp}(z)\,. \tag{17}$$

The plot of these functions for the reference cosmology is shown in the middle panel of Fig. 1.

Both for the 3D Fourier power spectrum and angular power spectra, the underlying redshift distribution $\mathrm{d}N^{sp}(z)/\mathrm{d}z/\mathrm{d}\Omega$ is

obtained from private communication with the GC-E2E work package group; the galaxy density has been obtained according to Model 3 from Pozzetti et al. (2016). However, unlike the 3D case, for the 2D projected GC_{sp} we neglect contributions from AP and RSD. While some residual RSD information could, in principle, remain in the projected 2D spectra, especially for thinner tomographic bins, we neglect RSD in this analysis; however, a previous study that included RSD found similar results (Taylor & Markovič 2022), suggesting that any impact on our conclusions is minimal. Furthermore, if one were to carry out a harmonic analysis for the GCsp sample as we suggest here, it is possible to make the measurement with an approach similar to Nock et al. (2010); such an approach reduces the RSD signal in the measured summary statistics, hence removing a possible mismatch between data and modeling. We leave a detailed investigation of RSD effects to future work, which will leverage a dedicated suite of simulations incorporating all relevant observational effects.

The spectroscopic redshift distribution is convolved with the probability $p_{sp}(z_p|z)$ in Eq. (9), with redshift uncertainty σ_b set to 0.001 and the fraction of outliers f_{out} set to zero, as specified in the *Euclid* scientific requirements (Laureijs et al. 2011). The other parameters in Eq. (9) are summarized in Table 3. The convolution mitigates the sharpness of the boundaries of the spectroscopic bins, and prevents potential numerical instabilities in the computation of the redshift integrals.

The spectroscopic galaxy bias $b^{sp}(z)$ is modeled as a piecewise constant function, and the values b_i^{sp} in the bins are summarized in Table 2 along with the bin edges. Both the bias values and the bins are the same that have been used in EP-VII. In this work, also a finer binning has been considered, in particular 12, 24 and 40 equally spaced bins in the range $0.9 < z < 1.8$. The values of the bias for finer binning are obtained by linear interpolation of the values listed in Table 2.

3. Fisher information matrix

The Fisher information matrix is defined as the expectation value of the Hessian of the log-likelihood:

$$F_{\alpha\beta} = -\left\langle \frac{\partial^2 \ln L}{\partial\theta_\alpha \partial\theta_\beta} \right\rangle , \tag{18}$$

where α and β are the model parameter indices, including both cosmological and nuisance parameters. The expected parameter covariance matrix is the inverse of the Fisher matrix:

$$C_{\alpha\beta} = \left(F^{-1}\right)_{\alpha\beta} . \tag{19}$$

The marginalized $1\,\sigma$ uncertainties, where σ is the Gaussian standard deviation, on the model parameters are the square roots of the diagonal elements of the parameter covariance matrix:

$$\sigma_\alpha = \sqrt{C_{\alpha\alpha}} . \tag{20}$$

One of the metrics used to assess the scientific performance of *Euclid* is the w_0-w_a Figure-of-Merit (FoM) which has been defined as in EP-VII

$$\mathrm{FoM} \equiv \sqrt{\det\left(\tilde{F}_{w_0 w_a}\right)} = \left[\sigma^2_{w_0}\,\sigma^2_{w_a} - C^2_{w_0 w_a}\right]^{-1/2} . \tag{21}$$

The symbol $\tilde{F}_{w_0 w_a}$ denotes the Fisher information matrix relative to the dark energy equation of state parameters w_0 and w_a, see Eq. (1), marginalized over all the other free parameters. The FoM is inversely proportional to the area of the $1\,\sigma$ marginalized contour ellipse in the w_0-w_a plane. Tighter constraints on w_0 and w_a lead to smaller ellipses, which in turn means higher FoMs.

In this work we assume that the data vector $\mathcal{D}$, which contains the values of the $C(\ell)$'s or the $P(k)$'s considered, is distributed according to a multivariate Gaussian. Under this assumption, the Fisher matrix element $F_{\alpha\beta}$ can be calculated as

$$F_{\alpha\beta} = \frac{\partial \mathcal{D}^{\mathrm{T}}}{\partial\theta_\alpha}\,\mathrm{Cov}^{-1}\left[\mathcal{D},\mathcal{D}\right]\frac{\partial \mathcal{D}}{\partial\theta_\beta} , \tag{22}$$

where $\mathrm{Cov}\left[\mathcal{D},\mathcal{D}\right]$ represents the covariance matrix.

The scenarios and settings considered in the Fisher computations of this work are summarized in Table 4.

The following subsections describe the data vectors and the covariance matrices used in the approaches considered in this work, as well as the shot noise implementation.

3.1. Harmonic space approach

The assumption that the $a^A_{\ell m}$ coefficients of the observed fields follow a Gaussian distribution leads to the analytical expression for the Fisher matrix presented in Eq. (22). In this case the Gaussian covariance matrix for the harmonic power spectra $C^{AB}_{ij}(\ell)$ is

$$\mathrm{Cov}\left[C^{AB}_{ij}(\ell), C^{CD}_{km}(\ell')\right] = \frac{\delta_{\ell\ell'}}{2\,\ell+1} \times \left[\Sigma^{AC}_{ik}(\ell)\,\Sigma^{BD}_{jm}(\ell') + \Sigma^{AD}_{im}(\ell)\,\Sigma^{BC}_{jk}(\ell')\right] , \tag{23}$$

with $\delta_{\ell\ell'}$ the Kronecker delta symbol. Under the assumption that we account for the partial sky coverage only through the observed fraction of the sky f_{sky}, the masking effects are negligible, and the galaxy counts are affected by Poisson shot noise only, the matrices $\Sigma^{AB}_{ij}(\ell)$ can be expressed by

$$\Sigma^{AB}_{ij}(\ell) = \frac{1}{\sqrt{f_{sky}\,\Delta\ell}}\left(C^{AB}_{ij}(\ell) + N^{AB}_{ij}(\ell)\right) , \tag{24}$$

where $N^{AB}_{ij}(\ell)$ is the Poisson shot noise matrix described later in Sect. 3.4 and $\Delta\ell$ is the spacing between the multipoles in which the $C(\ell)$ are sampled.

The data-vector in the harmonic space approach contains the independent values of the $C(\ell)$'s to be included in the computation. Since the tomographic angular power spectra are matrices, it is convenient to vectorize them. In this context the term "vectorize" refers to matrix vectorization. In this paragraph we are providing some examples of matrix vectorization for our probes; a formal description can be found in Sect. A.

Let us consider the GC_{ph} auto-correlation $C^{phph}_{ij}(\ell)$ at fixed multipole ℓ; this is usually represented as a 10×10 symmetric matrix with $10(10+1)/2 = 55$ independent components. This data vector can also be represented as a row vector of the independent components:

$$\mathbf{C}(\ell) = \{\mathbf{C}_1(\ell), \mathbf{C}_2(\ell), \ldots, \mathbf{C}_{55}(\ell)\} , \tag{25}$$

where the index of the vector enumerates the 55 independent components of $\mathbf{C}(\ell)$ considered in the analysis.

When considering three probes – WL, GC_{ph}, and GC_{sp} – there are 6 angular power spectra matrices:

– 3 auto-correlations: $\mathbf{C}^{wlwl}(\ell)$, $\mathbf{C}^{spsp}(\ell)$, $\mathbf{C}^{phph}(\ell)$;

Table 4: Forecast setting scenarios in the harmonic approach.

Forecast settings in the harmonic approach			
Multipoles settings	Optimistic	GC_{ph}	$10 \leq \ell \leq 3000$
		GC_{sp}	$10 \leq \ell \leq 3000$
		WL	$10 \leq \ell \leq 5000$
	Pessimistic	GC_{ph}	$10 \leq \ell \leq 750$
		GC_{sp}	$10 \leq \ell \leq 750$
		WL	$10 \leq \ell \leq 1500$
General settings	Baseline	GC_{ph}	all the 10 bins of Table 2
		GC_{sp}	shot noise of Eq. (37)
	Alternative	GC_{ph}	only 4 bins of Table 2 with $z_i^-, z_i^+ \in [0.9, 1.8]$
		GC_{sp}	reduced shot noise of Eq. (41)

Notes. Summary of the setting scenarios considered in the forecast. For WL the general settings are not reported since no distinction other than the multipole range has been made. The scenario in which the GC_{sp} shot noise is reduced is not intended to be realistic, and has been studied only to probe the theoretical limitations of the harmonic approach.

– 3 cross-correlations: $\mathbf{C}^{\rm wlph}(\ell)$, $\mathbf{C}^{\rm wlsp}(\ell)$, $\mathbf{C}^{\rm phsp}(\ell)$.

The angular power spectra are evaluated in a grid of N_ℓ multipoles; the full data-vector $\mathcal{D}$ also includes all the values of the power spectra evaluated over all multipoles, viz.

$$\mathcal{D} = \{\mathbf{C}(\ell_1), \mathbf{C}(\ell_2), \dots, \mathbf{C}(\ell_{N_\ell})\} \ . \tag{26}$$

The covariance matrix associated with this data-vector is block diagonal, since the Kronecker delta of Eq. (23) ensures that different multipoles are uncorrelated:

$$\mathrm{Cov}\left[\mathcal{D}, \mathcal{D}\right] = \begin{pmatrix} \mathrm{Cov}\left[\mathbf{C}(\ell_1), \mathbf{C}(\ell_1)\right] & 0 & 0 \\ 0 & \ddots & 0 \\ 0 & 0 & \mathrm{Cov}\left[\mathbf{C}(\ell_{N_\ell}), \mathbf{C}(\ell_{N_\ell})\right] \end{pmatrix} . \tag{27}$$

The diagonal blocks, $\mathrm{Cov}\left[\mathbf{C}(\ell), \mathbf{C}(\ell)\right]$, account for all the correlations between the $\mathbf{C}(\ell)$'s:

$$\mathrm{Cov}\left[\mathbf{C}(\ell), \mathbf{C}(\ell)\right] = \begin{pmatrix} \mathrm{Cov}\left[\mathbf{C}_1(\ell), \mathbf{C}_1(\ell)\right] & \cdots & \mathrm{Cov}\left[\mathbf{C}_1(\ell), \mathbf{C}_\mathcal{N}(\ell)\right] \\ \vdots & \ddots & \vdots \\ \mathrm{Cov}\left[\mathbf{C}_\mathcal{N}(\ell), \mathbf{C}_1(\ell)\right] & \cdots & \mathrm{Cov}\left[\mathbf{C}_\mathcal{N}(\ell), \mathbf{C}_\mathcal{N}(\ell)\right] \end{pmatrix} , \tag{28}$$

where the single blocks $\mathrm{Cov}\left[\mathbf{C}_i(\ell), \mathbf{C}_j(\ell)\right]$ are computed according to Eq. (23). With these definitions, the Fisher matrix element $F_{\alpha\beta}$ can be calculated from Eq. (22) as

$$F_{\alpha\beta} = \sum_{\ell=\ell_1}^{\ell_{N_\ell}} F_{\alpha\beta}(\ell) = \sum_{\ell=\ell_1}^{\ell_{N_\ell}} \frac{\partial \mathbf{C}(\ell)}{\partial \theta_\alpha}^T \mathrm{Cov}\left[\mathbf{C}(\ell), \mathbf{C}(\ell)\right]^{-1} \frac{\partial \mathbf{C}(\ell)}{\partial \theta_\beta} , \tag{29}$$

where the first equality follows from the block diagonal form of the covariance.

3.2. Naming conventions

For later convenience, here are reported the adopted conventions for naming the Fisher matrices that have been computed in this work:

1. The name of a Fisher matrix is representative of the data vector, and it is composed of different labels, which identify the $C(\ell)$'s contained in the data-vector itself.
2. Within the name of a Fisher matrix, the auto-correlation $C^{\rm AA}(\ell)$ of the probe A is labeled simply as A, while the cross-correlation $C^{\rm AB}(\ell)$ between the two probes A and B is denoted as XC(A, B).
3. Square brackets are used to delimit the data-vector extent.
4. The pairwise cross-covariances between the $C(\ell)$'s included in a given data-vector are always considered in the computation of the corresponding Fisher matrix.
5. The sum of two Fisher matrices $[F_1]$ and $[F_2]$ is simply denoted by $[F_1] + [F_2]$. This simple sum corresponds to combining $[F_1]$ and $[F_2]$ without taking into account the cross-covariances between their data-vectors, i.e., it is an independent sum.

Let us return to the example where only the auto-correlation of GC_{ph} is considered. In this case the data-vector at fixed ℓ is

$$\mathbf{C}(\ell) = \left\{\mathbf{C}^{\rm phph}(\ell)\right\} , \tag{30}$$

and ranges over 55 elements (assuming 10 tomographic bins). Consequently, the covariance matrix is made by a single 55×55 block:

$$\mathrm{Cov}\left[\mathbf{C}^{\rm phph}(\ell), \mathbf{C}^{\rm phph}(\ell)\right] , \tag{31}$$

which takes into account the auto-covariance of GC_{ph} only.

When considering two or more probes, multiple combinations can be constructed, depending on whether or not cross-covariances and cross-correlations are included in the computation. In this work we reserve the word "cross-covariance" to the off-diagonal blocks of the covariance matrix Eq. (28), e.g., the blocks $\mathrm{Cov}\left[\mathbf{C}_i^{ph}(\ell), \mathbf{C}_j^{wl}(\ell)\right]$. The term "cross-correlation" (signal) is instead used to denote the data-vector entry corresponding to the correlation between two probes, e.g., $\mathbf{C}^{\rm wlph}(\ell)$.

The possible combinations that can be constructed using two probes, A and B, are described in detail in Appendix A.

3.3. Hybrid approach

The harmonic space approach has both advantages and disadvantages. One of the main advantages of the harmonic space approach is the straightforward way to compute cross-covariances.

The main disadvantage of treating the clustering signal in the harmonic domain is that the projection on the celestial sphere results in a partial loss of information from the galaxy density distribution along the radial direction.

For $\mathrm{GC_{ph}}$, this loss is limited, since the redshift resolution is already hampered by large photometric errors. In the spectroscopic sample, the redshifts are measured with much better precision, therefore the 2D projection results in a larger loss of constraining power from $\mathrm{GC_{sp}}$. The tomographic technique can be employed in order to partially recover the radial information about the distances of the galaxies.

The natural approach to treating $\mathrm{GC_{sp}}$ is the "3D" or P_k. Directly using a 3D galaxy power spectrum allows us to naturally exploit the high redshift resolution of the spectroscopic sample. Nonetheless, in this case it is difficult to compute cross-correlations and cross-covariances between WL, $\mathrm{GC_{ph}}$, and $\mathrm{GC_{sp}}$.

In this work we therefore considered two approaches to combine $\mathrm{GC_{sp}}$ with WL and $\mathrm{GC_{ph}}$. The first is to treat all probes with the angular power spectra, as described in the previous section. In the second approach, the Fisher matrix contribution for the $\mathrm{GC_{sp}}$ auto-correlation is taken into account by adding a posteriori the Fisher matrix computed in the 3D approach of EP-VII, referred to here as $\mathrm{GC_{sp}}(P_k)$.

The core idea of the latter approach is to add the $\mathrm{GC_{sp}}$ auto-correlation using the 3D observable and its cross-correlations with the other probes, treating it as a 2D observable, in order to be able to compute the covariance matrix analytically: for this reason we dubbed it the hybrid approach.

The starting point of the hybrid approach is to include the harmonic $\mathrm{GC_{ph}}$ auto-correlation and the harmonic $\mathrm{GC_{ph}} \times \mathrm{GC_{sp}}$ cross-correlation in the data-vector

$$\mathbf{C}(\ell) = \left\{\mathbf{C}^{\mathrm{phph}}(\ell), \mathbf{C}^{\mathrm{phsp}}(\ell)\right\} , \tag{32}$$

with covariance matrix

$$\begin{pmatrix} \mathrm{Cov}\left[\mathrm{phph}, \mathrm{phph}\right] & \mathrm{Cov}\left[\mathrm{phph}, \mathrm{phsp}\right] \\ \mathrm{Cov}\left[\mathrm{phsp}, \mathrm{phph}\right] & \mathrm{Cov}\left[\mathrm{phsp}, \mathrm{phsp}\right] \end{pmatrix} , \tag{33}$$

where we have dropped $\mathbf{C}$ and the exponent in order to have a lighter notation.

We refer to the resulting Fisher matrix with the notation $[\mathrm{GC_{ph}} + \mathrm{XC}(\mathrm{GC_{ph}}, \mathrm{GC_{sp}})]$.

The Fisher matrix of $\mathrm{GC_{sp}}(P_k)$ is independently added:

$$\begin{aligned} F_{\alpha\beta}[\mathrm{GC_{ph}} + \mathrm{XC}(\mathrm{GC_{ph}}, \mathrm{GC_{sp}}) \; + \; \mathrm{GC_{sp}}(P_k)] \equiv \\ F_{\alpha\beta}[\mathrm{GC_{ph}} + \mathrm{XC}(\mathrm{GC_{ph}}, \mathrm{GC_{sp}})] + F_{\alpha\beta}[\mathrm{GC_{sp}}(P_k)] \; . \end{aligned} \tag{34}$$

This procedure is equivalent to neglecting the covariance terms between the $\mathrm{GC_{sp}}$ auto-correlation and the other observables. More details are elaborated in Appendix A.1.

3.4. Poisson shot noise

The Poisson shot noise (Baldauf et al. 2013) has been implemented similarly to what was done in EP-VII. It is assumed that only the auto-correlation $C(\ell)$'s in the same tomographic bin are affected by a shot noise, which is independent of the multipole:

$$N_{ij}^{AB}(\ell) = \delta_{AB}\, \delta_{ij}\, N_i^A \; . \tag{35}$$

The quantity N_i^A represents the shot noise associated with the probe A at tomographic bin i. For photometric and spectroscopic galaxy clustering in the harmonic domain this is simply given by

$$N_i^{\mathrm{ph}} \equiv \left[\int_{z_i^-}^{z_i^+} \mathrm{d}z \, \frac{\mathrm{d}\mathcal{N}^{\mathrm{ph}}}{\mathrm{d}z\mathrm{d}\Omega}\right]^{-1} , \tag{36}$$

$$N_i^{\mathrm{sp}} \equiv \left[\int_{z_i^-}^{z_i^+} \mathrm{d}z \, \frac{\mathrm{d}\mathcal{N}^{\mathrm{sp}}}{\mathrm{d}z\mathrm{d}\Omega}\right]^{-1} . \tag{37}$$

For WL the definition is instead given by the $\mathrm{GC_{ph}}$ shot noise multiplied by the variance σ_ϵ^2 of the intrinsic galaxy ellipticity

$$N_i^{\mathrm{wl}} \equiv \sigma_\epsilon^2 \left[\int_{z_i^-}^{z_i^+} \mathrm{d}z \, \frac{\mathrm{d}\mathcal{N}^{\mathrm{ph}}}{\mathrm{d}z\mathrm{d}\Omega}\right]^{-1} . \tag{38}$$

The value assumed for σ_ϵ is 0.3 as in EP-VII.

As the Kronecker delta δ_{AB} of Eq. (35) states, no shot noise has been considered for the cross-correlation $C(\ell)$'s. It is in fact commonly assumed for the noises of different tracers to be uncorrelated (EP-VII). This approximation is expected to work well for the cross-correlation between weak lensing and galaxy clustering, since these are different tracers of the same underlying dark matter distribution.

In the cross-correlation of $\mathrm{GC_{ph}}$ with $\mathrm{GC_{sp}}$ the tracers are the galaxies for both probes, so in principle a shot noise term in the cross power spectra (cross-noise) should be present. In this work we checked the δ_{phsp} approximation of Eq. (35) with the following approach. Given that the Poisson shot noise affecting the two-point function comes from the count of galaxy self-pairs – see the introduction of Baldauf et al. (2013) – the cross-noise is due to those galaxies which are both in the photometric and in the spectroscopic sample. The scenario with the highest noise is therefore the one in which the spectroscopic sample is a proper subset of the photometric one. So, assuming this worst case scenario, a subtraction of the spectroscopic galaxy distribution from the photometric one has been performed. After the subtraction there is no more overlap between the two samples, and their cross-noise becomes zero by construction. It has been checked that the constraints do not change appreciably after the subtraction, with the FoM and the marginalized uncertainties of the free parameters being negligibly affected. However, we point out that the removal of the spectroscopic galaxies from the photometric samples might cause a bias in the clustering signal approach; the approach we followed was just a way to quantify the impact of the shot noise in the worst case scenario.

The shot noise affects in a direct way the diagonal covariance blocks corresponding to the auto-correlation power spectra, as it enters in all the factors of Eq. (23). This is what happens for example in the case of the auto-covariance of $\mathrm{GC_{sp}}$

$$\begin{aligned} \mathrm{Cov}\left[C_{ij}^{\mathrm{spsp}}(\ell), C_{km}^{\mathrm{spsp}}(\ell)\right] \propto \left\{\left[C_{ik}^{\mathrm{spsp}} + N_{ik}^{\mathrm{spsp}}\right]\left[C_{jm}^{\mathrm{spsp}} + N_{jm}^{\mathrm{spsp}}\right]\right. \\ \left. + \left[C_{im}^{\mathrm{spsp}} + N_{im}^{\mathrm{spsp}}\right]\left[C_{jk}^{\mathrm{spsp}} + N_{jk}^{\mathrm{spsp}}\right]\right\} , \end{aligned} \tag{39}$$

where the ℓ dependence on the right-hand side (e.g., $N_{ik}^{\mathrm{spsp}}(\ell)$) has been omitted for compactness. However, the fact that the auto-correlation power spectra are contaminated by the shot noise indirectly also alters the other blocks of the covariance matrix. For example, the diagonal block corresponding to the auto-covariance of $\mathbf{C}^{\mathrm{phsp}}(\ell)$ reads

$$\begin{aligned} \mathrm{Cov}\left[C_{ij}^{\mathrm{phsp}}(\ell), C_{km}^{\mathrm{phsp}}(\ell)\right] \propto \left\{\left[C_{ik}^{\mathrm{phph}} + N_{ik}^{\mathrm{phph}}\right]\left[C_{jm}^{\mathrm{spsp}} + N_{jm}^{\mathrm{spsp}}\right]\right. \\ \left. + C_{im}^{\mathrm{phsp}}\, C_{jk}^{\mathrm{phsp}}\right\} . \end{aligned} \tag{40}$$

and therefore also the terms coming from the inclusion of the XC(GC_{ph}, GC_{sp}) are affected by the shot noise of both GC_{ph} and GC_{sp}. Moreover, since the number of galaxies in the spectroscopic sample is ~ 80 times smaller than the galaxies in the photometric one, from Eq. (37) it is clear that the GC_{sp} shot noise is larger than the one associated with GC_{ph}. In order to quantify the impact of the GC_{sp} noise, the forecasts have been performed also in an unrealistic alternative scenario, where this noise is artificially reduced as if the number of spectroscopic galaxies were equal to the number of photometric ones. This is done in practice by introducing an alternative reduced shot noise for GC_{sp}, defined as follows

$$\tilde{N}_i^{\rm sp} \equiv \frac{N_{\rm sp}^{\rm tot}}{N_{\rm ph}^{\rm tot}} N_i^{\rm sp} \,, \tag{41}$$

where $N_{\rm sp}^{\rm tot}$ ($N_{\rm ph}^{\rm tot}$) is the total number of spectroscopic (photometric) galaxies, computed by integrating the galaxy distribution over its redshift range. As it is discussed in Sect. 4 it turns out that the results in the harmonic approach drastically change using this reduced noise. We emphasize that this test was performed only to check what is the origin of the different GCsp and GCph constraints in the harmonic approach and it is not representative of any realistic survey scenario.

4. Results

In this section we present the results of the forecast. The results are mainly reported as marginalized relative 1–σ uncertainties on the FoM and the parameters in the reference cosmology in Table 1:

$$\delta X\,[\%] \equiv 100\,\frac{X_b - X_a}{X_a} \,, \tag{42}$$

where X generically denotes the FoM or the relative uncertainty $\sigma_\theta/\theta_{\rm fid}$. The subscript a denotes the Fisher matrix whose constraints are used as reference, while b is the Fisher matrix under examination, also referred to as the minuend in the following.

The scenarios considered in this forecast are summarized in Table 4. Concerning the multipole range, two scenarios have been studied: one optimistic and one pessimistic. In the optimistic scenario the multipole range for galaxy clustering is set to $\ell \in [10, 3000]$, while it is $\ell \in [10, 5000]$ for WL. In the pessimistic scenario, instead, the multipole range is $\ell \in [10, 750]$ for GC_{ph}, GC_{sp}, and $\ell \in [10, 1500]$ for WL.

In order to better understand the differences between GC_{ph} and GC_{sp} when both are treated in the harmonic domain, one more setting has been added, in which GC_{sp} employs the alternative reduced shot noise described in Sect. 3.4. We remark that this scenario is not meant to be realistic and it is considered only to investigate the different constraining power of the GC_{sp} and GC_{ph} probes.

For the same reason, in the case of GC_{ph} the forecast has been performed with an alternative tomographic binning, where only the 4 photometric bins in the redshift range $z \in [0.9, 1.8]$ are considered (see Table 2). This setting makes both GC_{ph} and XC(WL, GC_{ph}) comparable with GC_{sp} and XC(WL, GC_{sp}), respectively. In fact, apart from the shape of the galaxy distribution and the values of the galaxy bias, in the harmonic domain the two main differences between GC_{ph} and GC_{sp} are the shot noise and the redshift range of the galaxy catalog.

This section is organized as follows. In Sect. 4.1 the results from the combination of GC_{ph} and GC_{sp} are presented, including a comparison between GC_{ph} and GC_{sp} when treated in the harmonic domain. In Sect. 4.2 the results are reported for the combination of WL and GC_{sp}, also comparing the impact on the constraints from XC(WL, GC_{sp}) against XC(WL, GC_{ph}). In Sect. 5, the results of the so-called *Euclid* 6×2pt statistics are reported; this term refers to the combination of all possible two-point functions that can be constructed from WL, GC_{ph}, and GC_{sp}. The constraints coming from the combination of the full set of *Euclid* main probes are shown, focusing on the importance of cross-covariances and cross-correlations between them. We have checked the numerical stability of our results with respect to several hyperparameters, such as the k and z sampling of the matter power spectra; we find the variations of the marginalized errors and FoM to be negligible.

In the following, the term harmonic indicates that all the observables are treated using the angular power spectrum formalism. Instead, in the hybrid 6×2pt approach the data vector is entirely composed of $C(\ell)$'s except for the spectroscopic auto-correlation, whose contribution is included as described in Sect. 3.3 and in Sect. A.1.

4.1. Combining photometric and spectroscopic clustering

In this section we report the results for the combination of GC_{ph} and GC_{sp}. We take as reference values for the results the constraints coming from the independent combination of GC_{ph} and GC_{sp}, that is [GC_{ph}] + [GC_{sp}] in the harmonic approach and [GC_{ph}] + [$GC_{sp}(P_k)$] in the hybrid one. We remind that the notation [GC_{ph}] + [GC_{sp}] represents the simple sum of the Fisher matrices of the two probes, which does not account for their cross-covariance. The forecasts for this combination are reported in the optimistic scenario only for brevity.

4.1.1. Impact of the GC_{ph}-GC_{sp} cross-covariance on parameter constraints

Table 5 shows that, as expected, the cross-covariance slightly worsens the FoM. However, the contribution is always smaller than 3%, decreasing as the number of GC_{sp} bins increases. This trend can be understood as follows: the finer the tomographic binning of GC_{sp} the smaller the support of the integrand of the off-diagonal terms $\mathbf{C}^{\rm phsp}(\ell)$. Intuitively, the value of the integral over each of the 4 thick bins is diluted into a larger number of thinner bins when a finer binning is used. Hence the off-diagonal block Cov $\left[\mathbf{C}^{\rm phph}(\ell), \mathbf{C}^{\rm spsp}(\ell)\right]$ and its transposed counterpart become larger and sparser as the number of bins is increased, and therefore the cross-covariance contribution becomes smaller. Physically this could be understood considering that for 40 bins the loss of information due to the projection transversely to the line of sight is less severe than for 4 bins only.

The same trend is observed also for the marginalized uncertainties on the cosmological parameters, as can be seen by Fig. 2. The parameters mostly affected by the covariance are $\Omega_{\rm b}$ and h, whose constraints in the 4 bin setting worsen by 4% and 6% respectively. However, as soon as the binning is refined, the effect gets smaller, becoming about 0.9% for $\Omega_{\rm b}$ and 2.5% for h. The uncertainties on $\Omega_{\rm m}$, $n_{\rm s}$, and σ_8 are instead affected by less than 2% for all the binning settings. This outcome is confirmed also by Fig. 3, which reports the relative marginalized uncertainties and the FoM as horizontal bars. The [GC_{ph}+GC_{sp}] bars (in cyan) always have practically the same length as the [GC_{ph}] + [GC_{sp}] bars (in green), and they look more and more similar as the number of GC_{sp} bins increases.

Table 5: FoM for GC_{ph}, GC_{sp} and their cross-correlation.

$GC_{ph} \times GC_{sp}$ FoM forecasts				
GC_{sp} bins	Fisher matrix	FoM	ΔFoM	ΔFoM(%)
–	$[GC_{ph}]$	63.12	–	–
4	$[GC_{ph}] + [GC_{sp}(P_k)]$	230.27	–	–
	$[GC_{ph}+XC(GC_{ph}, GC_{sp})] + [GC_{sp}(P_k)]$	234.54	–	–
	$[GC_{ph}] + [GC_{sp}]$	65.69	–	–
	$[GC_{ph}+GC_{sp}]$	63.95	−1.75	−2.66%
	$[GC_{ph}+GC_{sp}+XC(GC_{ph}, GC_{sp})]$	69.63	+3.94	+6.00%
12	$[GC_{ph}] + [GC_{sp}]$	72.02	–	–
	$[GC_{ph}+GC_{sp}]$	70.48	−1.55	−2.15%
	$[GC_{ph}+GC_{sp}+XC(GC_{ph}, GC_{sp})]$	79.87	+7.85	+10.90%
24	$[GC_{ph}] + [GC_{sp}]$	85.02	–	–
	$[GC_{ph}+GC_{sp}]$	83.88	−1.13	−1.33%
	$[GC_{ph}+GC_{sp}+XC(GC_{ph}, GC_{sp})]$	108.35	+23.34	+27.45%
40	$[GC_{ph}] + [GC_{sp}]$	111.22	–	–
	$[GC_{ph}+GC_{sp}]$	110.39	−0.83	−0.75%
	$[GC_{ph}+GC_{sp}+XC(GC_{ph}, GC_{sp})]$	153.71	+42.48	+38.20%

Notes. The ΔFoM column contains the variation of the FoM with respect to the independent sum $[GC_{ph}] + [GC_{sp}]$ for the given number of bins. The ΔFoM (%) column is calculated by taking ΔFoM as a percentage of the FoM of $[GC_{ph}] + [GC_{sp}]$.

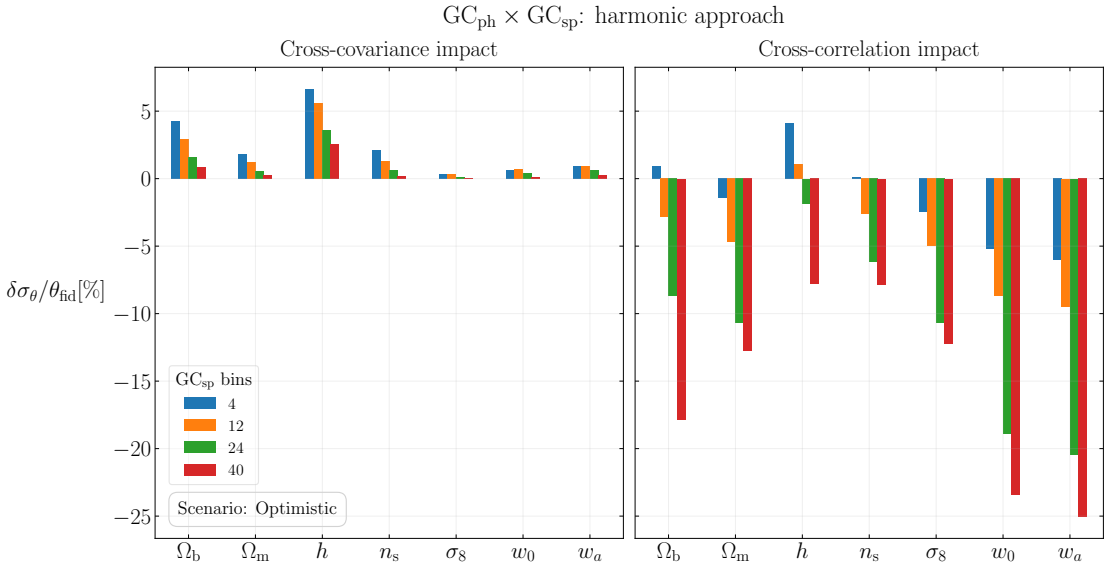

Fig. 2: Impact on $1\text{–}\sigma$ parameter errors of cross-covariance and cross-correlation in the harmonic approach for the combination of GC_{ph} and GC_{sp}. The left panel shows the impact of the cross-covariance, quantified with the percentage differences between $[GC_{ph} + GC_{sp}]$ and $[GC_{ph}] + [GC_{sp}]$. In the right panel the impact of the cross-correlation is reported, quantified by percentage differences of $[GC_{ph} + GC_{sp} + XC(GC_{ph}, GC_{sp})]$ with respect to $[GC_{ph}] + [GC_{sp}]$. Note the opposite sign of the percentage differences for FoM and uncertainties.

In conclusion, the cross-covariance between GC_{ph} and GC_{sp} can be considered negligible, as it does not change the uncertainties on the cosmological parameters by more than 6% and the FoM by more than 3%.

4.1.2. Impact of the $XC(GC_{ph}, GC_{sp})$ signal on parameter constraints

Harmonic approach In the harmonic approach the contribution to the FoM coming from the $XC(GC_{ph}, GC_{sp})$ cross-correlation is always positive, as reported in Table 5, and it is about 6% (38%) with 4 (40) bins for GC_{sp}. This gain is visible also in Fig. 3, where the FoM and the marginalized uncertainties from the $[GC_{ph} + GC_{sp} + XC(GC_{ph}, GC_{sp})]$ Fisher matrix are represented with orange bars. The improvements on the errors for w_0, w_a, and consequently on the FoM, are particularly visible for finer binnings.

The marginalized uncertainties on the cosmological parameters also improve, but the gain is more modest than that one on the FoM, as shown in the right panel of Fig. 2. In fact, the biggest improvements are for w_0 and w_a, whose uncertainties get

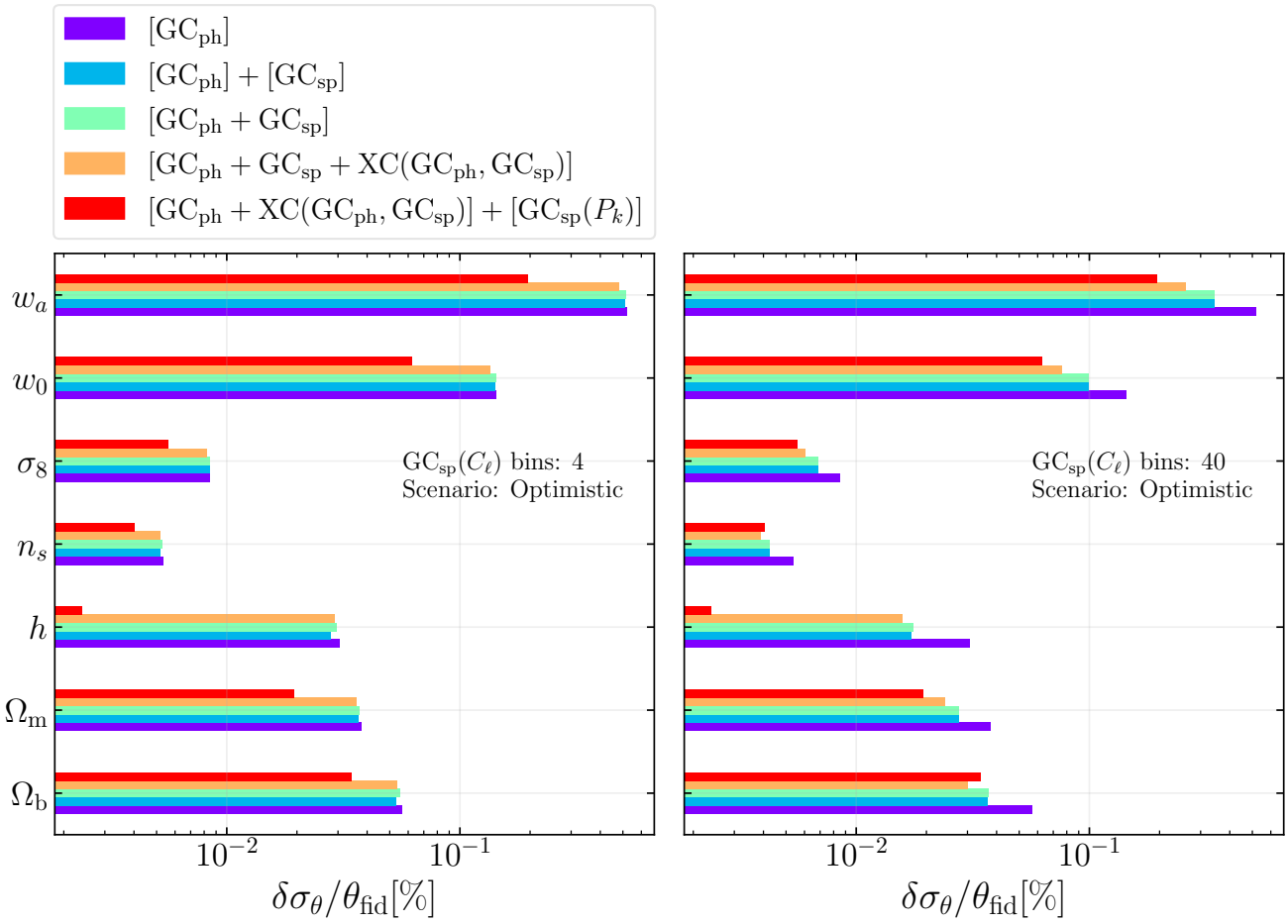

Fig. 3: Comparison between harmonic and hybrid harmonic-Fourier approaches for the case of $GC_{ph} \times GC_{sp}$.

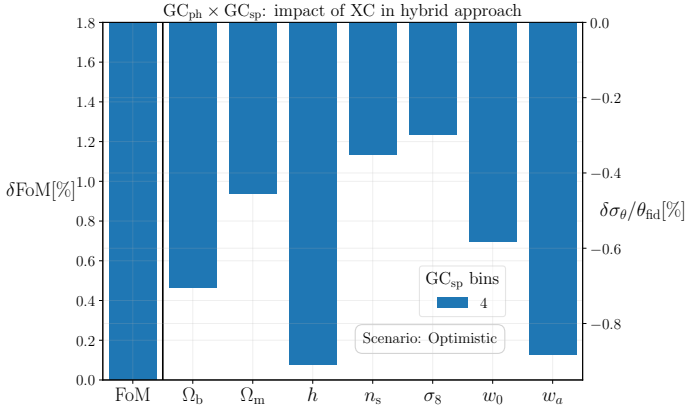

Fig. 4: Impact on FoM and marginalized 1–σ errors, of the $XC(GC_{ph}, GC_{sp})$ in the hybrid approach, for the optimistic scenario. The reference here are the constraints coming from $[GC_{ph}] + [GC_{sp}(P_k)]$, while the minuend for the percentage difference is $[GC_{ph} + XC(GC_{ph}, GC_{sp})] + [GC_{sp}(P_k)]$. In the hybrid approach only 4 tomographic bins were used to compute the $XC(GC_{ph}, GC_{sp})$ angular power spectra, for consistency with the Fourier power spectrum analysis. Note the opposite sign of the percentage differences for FoM and uncertainties.

smaller at most by 23% and 25%, respectively. Instead, the uncertainty on the baryon density parameter, Ω_b, slightly increases by about 1% with 4 bins and becomes smaller by 18% with 40 bins. The small worsening on this parameter in the case of 4 bins has been attributed to the contribution of the cross-covariances between the $C(\ell)$'s included in the data-vector of the Fisher matrix $[GC_{ph} + GC_{sp} + XC(GC_{ph}, GC_{sp})]$, which are not taken into account in the simple sum $[GC_{ph}] + [GC_{sp}]$. It is possible that with 4 bins the gain coming from the inclusion of the XC signal is compensated by the covariance contribution, producing a net (small) worsening. However, as soon as the number of GC_{sp} bins increases, the positive contribution of the cross-correlation signal starts to dominate, and the constraints on Ω_b to improve too. The uncertainties on the other parameters also improve, in particular Ω_m and σ_8 gain at most 12% when 40 bins are used, as well as h and n_s which improve by 7% at maximum.

Hybrid approach In the hybrid approach instead, the $XC(GC_{ph}, GC_{sp})$ has quite a small impact on the constraints: the marginalized uncertainties and FoM from the $[GC_{ph} + XC(GC_{ph}, GC_{sp})] + [GC_{sp}(P_k)]$ Fisher matrix are very similar to the ones from $[GC_{ph}] + [GC_{sp}(P_k)]$, as is qualitatively shown by the barplots of Fig. 3. The percentage variations on the constraints resulting from adding the $XC(GC_{ph}, GC_{sp})$ are shown in Fig. 4. The variation on the FoM is contained between +1.5% and +2%, so there is a very small improvement when including $XC(GC_{ph}, GC_{sp})$ in the hybrid approach. This is also the case for the marginalized uncertainties which improve less than 1%; however, we would like to point out that this behavior could be due to numerical uncertainty. Therefore, it can be concluded

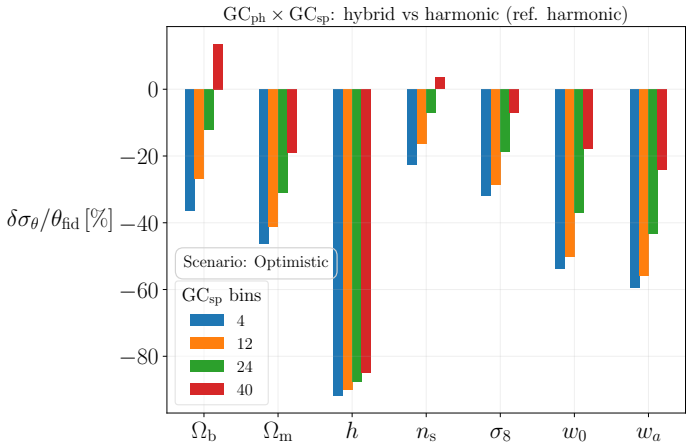

Fig. 5: Percentage difference between marginalized 1–σ errors of the hybrid and harmonic approaches, for the combination of GC$_{ph}$ and GC$_{sp}$ in the baseline optimistic scenario, when the cross-covariance is included. The percentage differences are normalized to the results of the harmonic approach.

that, in the hybrid approach, the inclusion of the XC(GC$_{ph}$, GC$_{sp}$) cross-correlation in the combination of GC$_{ph}$ and GC$_{sp}$ has a negligible impact on the results.

Hybrid approach vs harmonic approach As Fig. 5 shows, the hybrid approach performs better than the harmonic one in constraining almost all the cosmological parameters, even if the constraining power of the harmonic approach significantly improves with increasing the number of GC$_{sp}$ tomographic bins. The harmonic approach has a FoM of 69 (153) for 4 (40) spectroscopic bins, while the hybrid one provides a FoM of 234, which is 236% (52%) larger than in the former case. Thus the hybrid approach is better even when 40 spectroscopic bins are used for the harmonic one. In particular, this is true for the reduced Hubble constant h. In this case the hybrid approach performs remarkably better, with a gain on the marginalized uncertainty which is always between 75% and 100%, depending only slightly on the number of GC$_{sp}$ bins used for the harmonic approach. This is expected, since the hybrid approach takes advantage of the 3D power spectrum as an observable, in which radial BAO and RSD are included. The constraints on the other parameters appear instead quite sensitive to the GC$_{sp}$ binning. The differences on the w_0 and w_a uncertainties significantly decrease from more than 50% with 4 bins to about 20% with 40 bins, as it could be expected from the FoM differences between the hybrid approach and the harmonic one. For Ω_m and σ_8 the hybrid approach is still better than the harmonic one, even if the difference between the two approaches decreases significantly with the number of bins too.

The only exceptions are given by the baryon density, Ω_b, and the spectral index, n_s. In particular, the Ω_b uncertainty from the hybrid approach is more than 25% smaller than from the harmonic one with 4 spectroscopic bins, but the situation gets reversed with 40 bins. In the latter case the harmonic approach provides $\sim$ 10% better constraints on Ω_b than the hybrid one. The n_s uncertainty in the harmonic approach with 4 bins is about 20% larger than in the hybrid one. Instead, when 40 bins are used for the harmonic approach, the n_s uncertainty given by the hybrid approach is a few percents larger than the one given by the former.

To conclude, for the combination of GC$_{ph}$ and GC$_{sp}$, the hybrid approach always provides better constraints than the harmonic one. Increasing the number of bins in the harmonic approach improves its performances. Using 40 bins allows us to reach the performances of the hybrid approach for some parameters – n_s and Ω_b – but a large gap still remains for the other constraints, especially for h and the FoM.

4.1.3. Comparing photometric and spectroscopic clustering in the harmonic domain

In the harmonic approach, two alternative configurations have been considered, both for GC$_{ph}$ and GC$_{sp}$. The baseline configuration for GC$_{ph}$ consists in using all the 10 redshift bins reported in Table 2, while in the alternative configuration only the 4 bins strictly contained in the range [0.9, 1.8] are considered.

For spectroscopic clustering, the noise baseline settings correspond to using the shot noise as calculated from Eq. (37), while the alternative consists in using the artificially reduced version Eq. (41). In fact, from further investigation it turned out that a great limitation of the harmonic approach is due to the shot noise associated with the GC$_{sp}$ auto-correlation $C(\ell)$'s. This is in fact much higher than the one associated with GC$_{ph}$, since the expected number of Hα-emitting galaxies in the *Euclid* catalog ($\sim 2\times10^7$) is smaller than the expected number of galaxies in the photometric sample ($\sim 1.6\times10^9$). Therefore, in order to quantify the impact of the spectroscopic shot noise, the forecasts include also the artificially reduced shot noise setting, as explained in Sect. 3.4.

The results are shown in Fig. 6: in the left panel the standard GC$_{sp}$ shot noise of Eq. (37) is employed, while in the right one the reduced noise of Eq. (41) is used. Lowering the shot noise systematically boosts the results of the harmonic approach by about one order of magnitude, making its performance comparable or even better than in the hybrid case. In particular, as can be expected, the observable which most improves its performance is the harmonic GC$_{sp}$ auto-correlation.

Instead, when considering the behavior of the hybrid [GC$_{ph}$ + XC(GC$_{ph}$, GC$_{sp}$)] + [GC$_{sp}$(P_k)] Fisher matrix, as compared to the corresponding one in the harmonic domain, its performance remains stable against the change of the shot noise level, since the possible change of the latter would enter only GC$_{sp}$(P_k), which is fixed. Therefore, while in the harmonic case the survey performance increases with the noise reduction and the increasing of the number of spectroscopic bins, in the hybrid case the performance remains unchanged since both the noise level and the bin number are fixed.

The results of these scenarios are reported in Fig. 7. The constraints from GC$_{ph}$ only restricted to the 4 bins in the spectroscopic range (blue bars) are very close to the ones of GC$_{sp}$ when the shot noise is reduced (yellow bars). Thus in these special conditions the two probes are essentially equivalent. This is expected, since the functional form of the weight for galaxy clustering is the same, as in Eqs. (14) and (17), with the photometric function W_i^{ph} differing from the spectroscopic one W_i^{sp} only for the shape of the galaxy distribution and the values of the galaxy bias.

Fig. 7 shows also the two probes in the baseline configuration, in which 10 bins are used for GC$_{ph}$ and the more realistic shot noise of Eq. (37)) is used for GC$_{sp}$. On the one hand, the usage of all bins for GC$_{ph}$ reduces the uncertainties on cosmological parameters. On the other hand, the realistic shot noise of

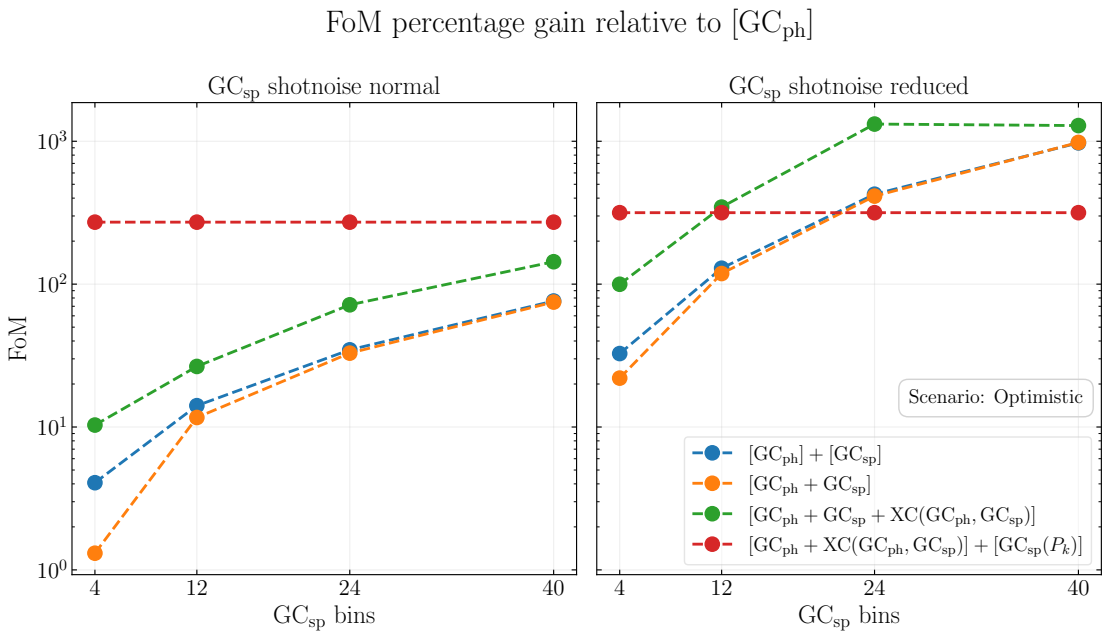

Fig. 6: Percentage gain on the FoM relative to photometric clustering alone ([GC_{ph}]). In the left panel the computation has been done using the standard GC_{sp} shot noise Eq. (37), while in the right panel the reduced version Eq. (41) has been used.

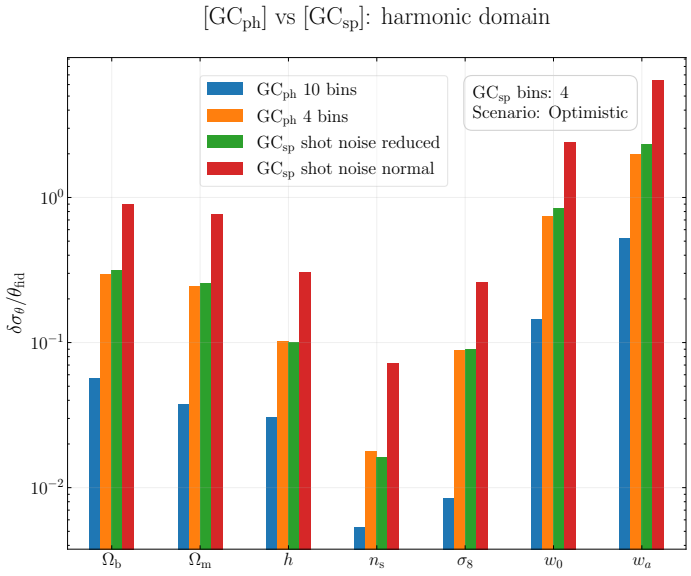

Fig. 7: Comparison between the constraints coming from [GC_{ph}] only and [GC_{sp}] only in the harmonic approach, in the different configurations described in Sect. 4. The vertical bars represent the values of the FoM and the relative marginal uncertainties.

GC_{sp} significantly affects its performances, making the uncertainties larger.

The conclusion is therefore that the shot noise and the redshift range of the galaxy sample are what make the difference between GC_{ph} and GC_{sp} in terms of constraining power, when both are treated in the harmonic domain. When GC_{ph} is restricted to the same range of GC_{sp} and the shot noise of the latter is reduced to the same level of the former, their constraints become comparable.

4.2. Combining weak lensing and spectroscopic clustering

In this section we report the results from the combination of WL and GC_{sp}. The Fisher matrix in the harmonic approach is [WL + GC_{sp} + XC(WL, GC_{sp})], while in the hybrid one it is [WL + XC(WL, GC_{sp})] + [$GC_{sp}(P_k)$]. We quantify the impact on parameter constraints of the WL-GC_{sp} cross-covariance and the XC(WL, GC_{sp}) cross-correlation. We take as reference values the results coming from the Fisher matrix corresponding to independent combination of WL and GC_{sp}, that is [WL]+[GC_{sp}] in the harmonic approach and [WL] + [$GC_{sp}(P_k)$] in the hybrid one. For brevity, the forecasts of this combination are reported in the optimistic scenario only.

4.2.1. Impact of the WL-GC_{sp} cross-covariance on parameter constraints

Table 6 reports the FoM values resulting from the combinations of WL and GC_{sp}. In this case the cross-covariance is even more negligible than in the GC_{ph}-GC_{sp} case, always impacting by less than 0.5% on the FoM. This effect gets smaller as the number of bins increases, starting from −0.47% with 4 spectroscopic bins up to +0.042% with 40 spectroscopic bins respectively. This last is unexpectedly positive, but the variation is so small that can be considered as a numerical fluctuation around zero.

The effect of the cross-covariance is very small also on the marginalized 1–σ uncertainties on the cosmological parameters, shown in the left panel of Fig. 8. The marginalized uncertainties affected the most are the ones on h and Ω_b, with variations of 0.7% and 0.3% respectively. The variations on all the other parameters are always well below 0.2%, and in all cases the absolute value of these variations decreases as the number of GC_{sp} bins increases, confirming the same trend observed for the FoM.

The conclusion here is that, when combining WL and GC_{sp} in the harmonic domain, their cross-covariance can be safely neglected. The limited impact of the WL-GC_{sp} cross-covariance might have been expected also considering the limited redshift

Table 6: FoM for WL, GC_{sp} and their cross-correlation.

$WL \times GC_{sp}$ FoM forecasts					
GC_{sp} bins		Fisher matrix	FoM	ΔFoM	ΔFoM (%)
4		[WL] + [$GC_{sp}(P_k)$]	158.13	–	–
		[WL+XC(WL, GC_{sp})] + [$GC_{sp}(P_k)$]	182.74	–	–
		[WL] + [GC_{sp}]	74.72	–	–
		[WL + GC_{sp}]	74.37	−0.35	−0.47%
		[WL + GC_{sp} + XC(WL, GC_{sp})]	103.56	+28.83	+38.59%
12		[WL] + [GC_{sp}]	92.90	–	–
		[WL + GC_{sp}]	92.77	−0.13	−0.14%
		[WL + GC_{sp} + XC(WL, GC_{sp})]	131.38	+38.47	+41.41%
24		[WL] + [GC_{sp}]	111.41	–	–
		[WL+GC_{sp}]	111.42	+0.01	+0.0021%
		[WL + GC_{sp} + XC(WL, GC_{sp})]	155.18	+43.76	+39.28%
40		[WL] + [GC_{sp}]	141.12	–	–
		[WL + GC_{sp}]	141.17	+0.06	+0.042%
		[WL + GC_{sp} + XC(WL, GC_{sp})]	188.45	+47.34	+33.55%

Notes. The ΔFoM column contains the variation of the figure of merit with respect to the independent sum [WL] + [GC_{sp}] for the given number of bins. The ΔFoM (%) column is calculated by taking ΔFoM as a percentage of the FoM of [WL] + [GC_{sp}].

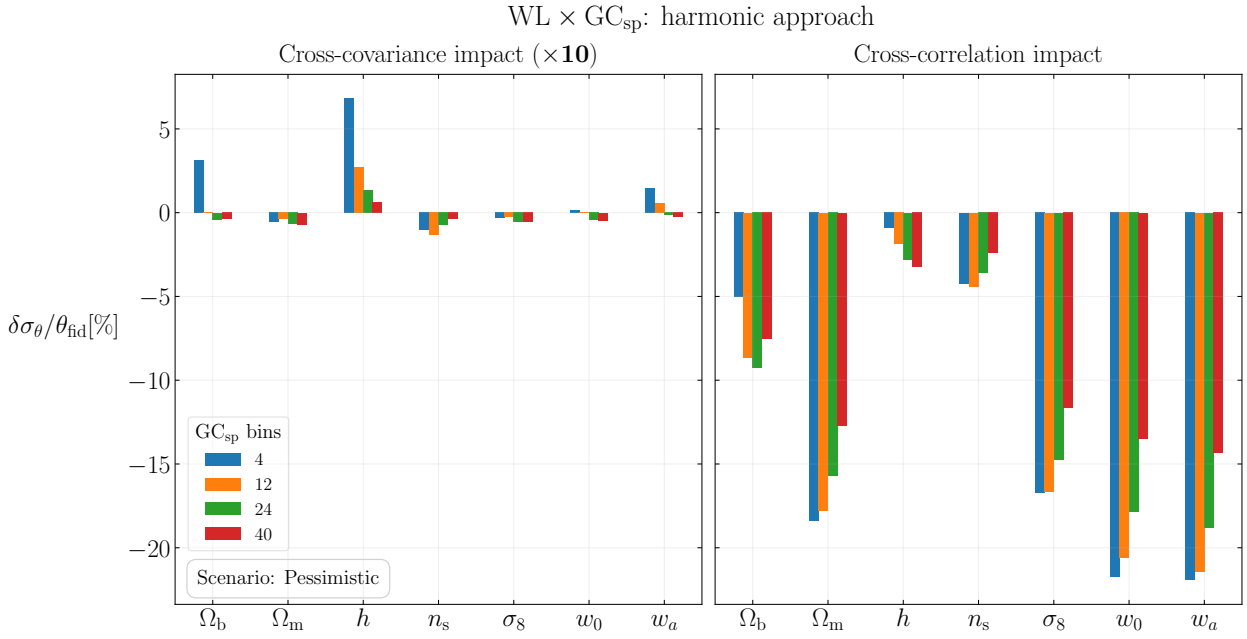

Fig. 8: Impact, on 1–σ parameter errors, of cross-covariance and cross-correlation in the harmonic approach for the combination of WL and GC_{sp}. The left panel shows the impact of the cross-covariance, quantified with the percentage differences between [WL+GC_{sp}] and [WL]+[GC_{sp}]. In the right panel the impact of the cross-correlation is reported, quantified by percentage differences of [WL + GC_{sp} + XC(WL, GC_{sp})] with respect to [WL] + [GC_{sp}]. The percentages on the left panel have been multiplied by 10 in order to make them visible with the same vertical scale of the right panel.

overlap of the two window functions, as can be seen in Fig.1. A similar result for another experiment other than *Euclid* has been obtained in Joachimi et al. (2021). Here the authors performed a joint data analysis combining weak lensing measurements from the Kilo-Degree Survey (KiDS-1000) and spectroscopic clustering from the Baryon Acoustic Oscillations Survey (BOSS) and 2-degree Field Lensing Survey (2dFLenS). The WL was treated using the harmonic power spectrum as an observable, as has been done in this work. Moreover, the cross-covariance matrix was computed in the harmonic domain, considering only the correlation between WL and the transverse component of GC_{sp}. The authors estimated the covariance matrix for the data through an analysis of over 20 000 fast full-sky mock galaxy catalogs, finding that the off-diagonal (cross-covariance) terms were negligible with respect to the diagonal (auto-covariance) ones.

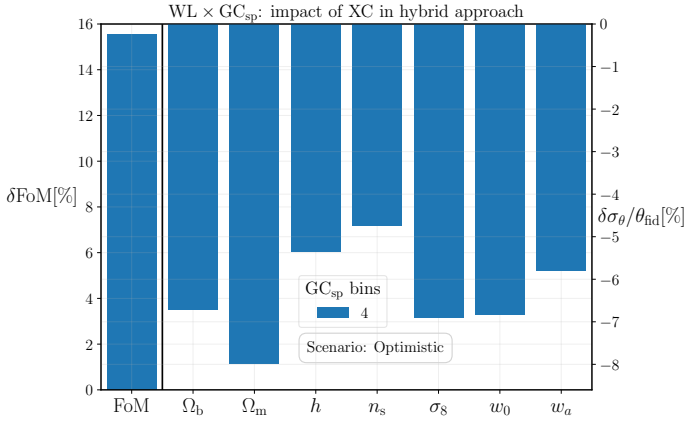

Fig. 9: Impact on FoM and marginalized 1–σ errors, of the XC(WL, GC_{sp}) in the hybrid approach, for the optimistic scenario. In the hybrid approach only 4 tomographic bins were used to compute the XC(WL, GC_{sp}) angular power spectra, for consistency with the Fourier power spectrum analysis. Note the opposite sign of the percentage differences for FoM and uncertainties.

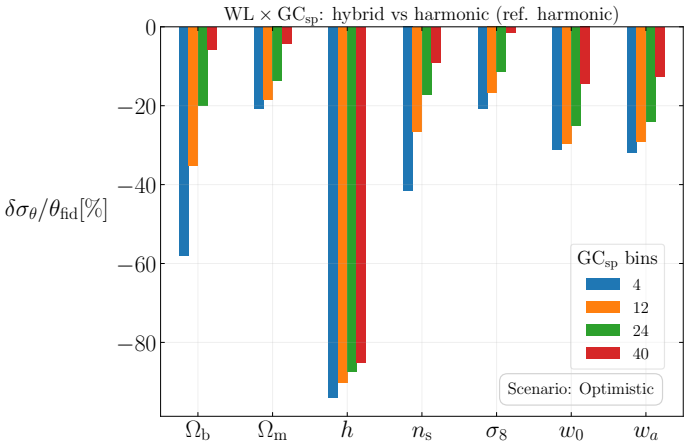

Fig. 10: Percentage difference between marginalized 1–σ errors of the hybrid and harmonic approaches, for the combination of WL and GC_{sp} in the baseline optimistic scenario. The percentage differences are normalized to the results of the harmonic approach.

4.2.2. Impact of the XC(WL, GC_{sp}) signal on parameter constraints

Harmonic approach When combining WL and GC_{sp}, the XC(WL, GC_{sp}) has a quite significant impact on the results of the harmonic approach, as Table 6 shows. The percentage gain on the FoM is always larger than +30%, and slightly depends on the number of spectroscopic bins used. The mild dependence on the number of GC_{sp} bins can be explained by observing that the WL weight functions of Eq. (12) have a broad support, which becomes larger as the tomographic index increases, as Fig. 1 shows. This suggests that increasing the radial resolution may not help in improving the constraints coming from the XC(WL, GC_{sp}).

It is also worth noting that the FoM percentage gain does not strictly increase with the number of spectroscopic bins. This not intuitive behavior is due to the normalization of the FoM percentage difference, which is the FoM of the [WL]+[GC_{sp}] Fisher matrix. This quantity depends on the number of spectroscopic bins, and it increases slightly faster than the variation induced by the cross-correlation in the FoM of the [WL+GC_{sp}+XC(WL, GC_{sp})] Fisher matrix. This can be seen from Table 6: the difference ΔFoM between the FoMs of the [WL + GC_{sp} + XC(WL, GC_{sp})] and [WL] + [GC_{sp}] Fisher matrices grows more slowly with the number of bins than the FoM of [WL] + [GC_{sp}] alone.

The marginalized 1–σ uncertainties decrease when the XC(WL, GC_{sp}) cross-correlation signal is included, especially the ones on w_0, w_a, σ_8 and Ω_m, as it can be seen from Fig. 8. For these parameters the improvement is always larger than 12% with 4 GC_{sp} bins, and it is about 20% at most when 40 bins are used. The gain on the Ω_b uncertainty is more modest, being contained between 5% and 10%. The gain on the uncertainties of the reduced Hubble constant h and the scalar spectral index n_s is always less than 5%.

The improvement in the marginalized uncertainties XC(WL, GC_{sp}) cross-correlation seems to decrease when increasing the number of spectroscopic bins, as happens for the FoM. Again, the reason for this behavior is that the performances of the Fisher matrix taken as reference – that is [WL] + [GC_{sp}] – improve faster than the relative contribution of the cross-correlation. This is true for all parameters except for h, which is the parameter affected the least.

Hybrid approach The impact on the constraints of the XC(WL, GC_{sp}) cross-correlation in the hybrid approach is less significant than in the harmonic one, as shown in Fig. 9. The FoM of the [WL + XC(WL, GC_{sp})] + [$GC_{sp}(P_k)$] Fisher matrix is 183, which is ∼ 15% higher than the one of the independent combination [WL] + [$GC_{sp}(P_k)$], which is 158. The improvements in the marginalized uncertainties are all contained between 5% and 7%, and there are no significant differences between the various parameters. The uncertainty on Ω_m is the most affected, gaining about 8%, while the least affected is the uncertainty on n_s, which is slightly lower than 5%.

4.2.3. Hybrid approach vs harmonic approach

When combining WL and GC_{sp}, the harmonic approach can reach the FoM of the hybrid one. This happens when 40 GC_{sp} bins are used to compute the harmonic Fisher matrix [WL + GC_{sp} + XC(WL, GC_{sp})]. The value reached by the FoM is 188, which is only 3% higher than the one given by the hybrid approach. Moreover, Fig. 10 shows that the marginalized uncertainties in w_0-w_a in the hybrid approach are smaller than their harmonic counterparts. Nonetheless, the FoM in the harmonic approach is slightly higher than the one in the hybrid approach. This is due to the correlation $C_{w_0 w_a}$ between the parameters, which enters the definition of the FoM in Eq. (21). The correlation is higher for the harmonic approach, and this compensates for the larger uncertainties, with a net result of a slightly higher FoM.

Regarding the marginalized uncertainties, Fig. 10 shows that the hybrid approach always performs better than the harmonic one. The reduced Hubble constant h is the parameter for which the difference is highest. In particular, the hybrid approach produces an uncertainty on h which is ∼ 90% (75%) smaller than the one given by the harmonic approach with 4 (40) spectroscopic bins. For the uncertainties on the other parameters the gap is smaller, and it reduces significantly as the number of spectroscopic bins increases. The most sensitive uncertainty is the one

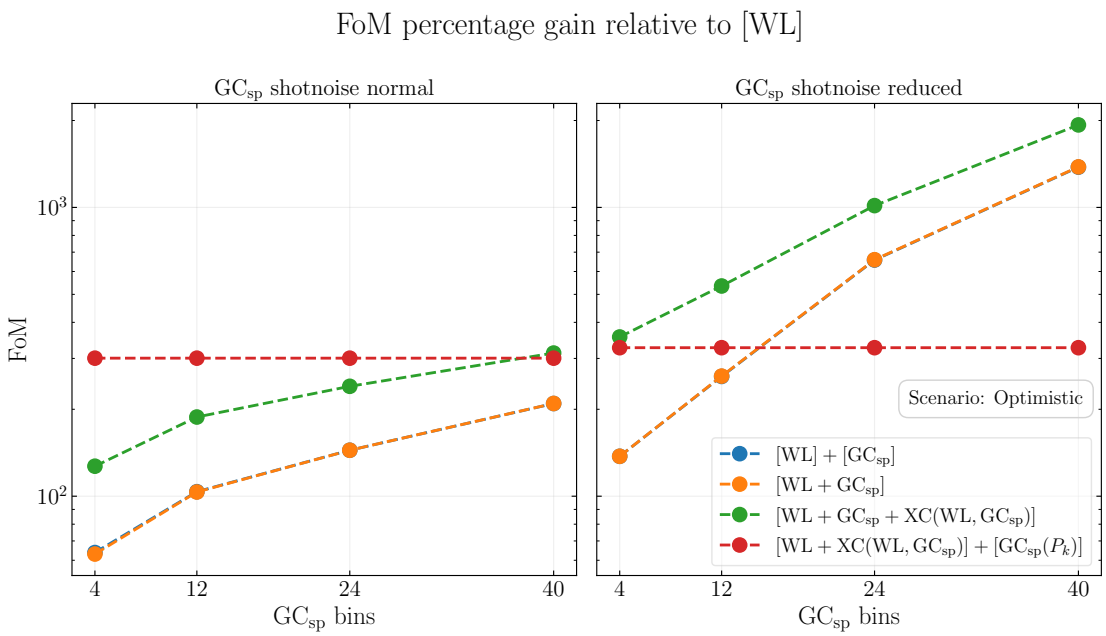

Fig. 11: Percentage gain on the FoM relative to weak lensing alone ([WL]). In the left panel the computation has been done using the standard GC_{sp} shot noise Eq. (37), while in the right panel the reduced version Eq. (41) has been used.

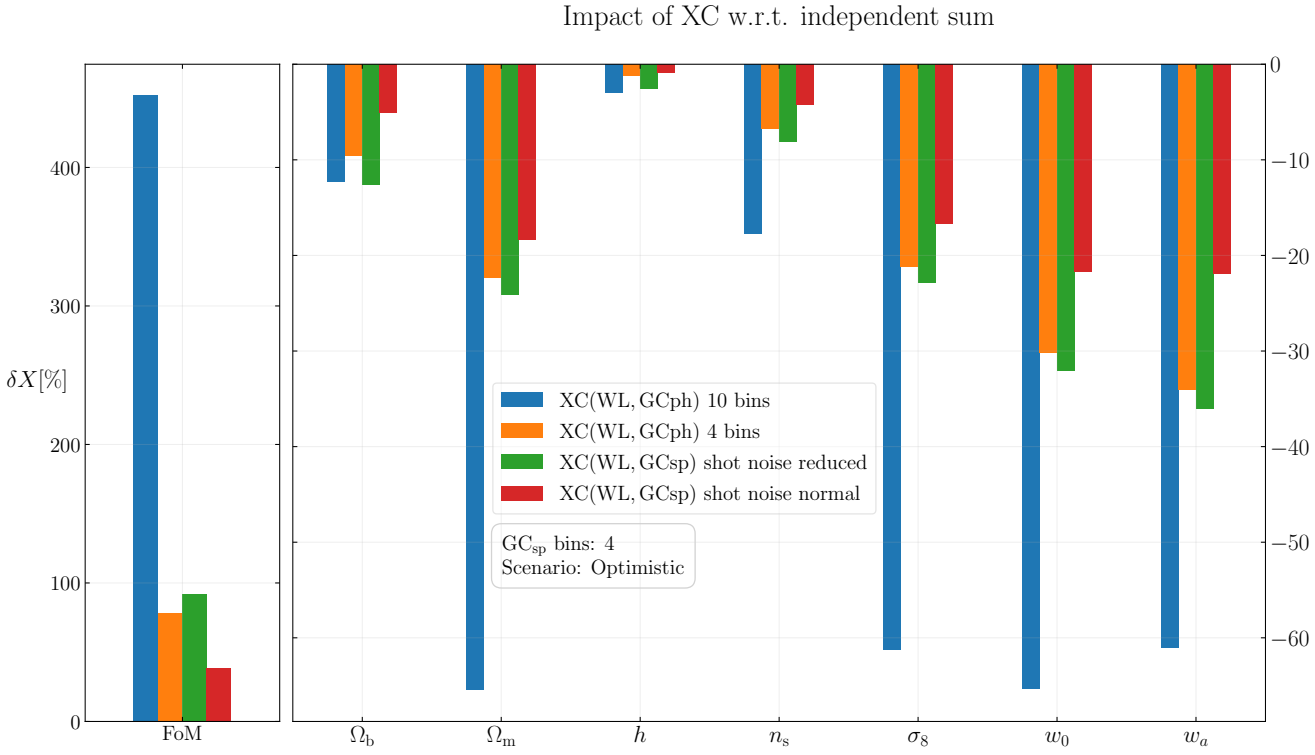

Fig. 12: Impact, on FoM and marginalized 1–σ uncertainties, of the XC(WL, GC_{ph}) and XC(WL, GC_{sp}) cross-correlations in different configurations. The vertical bars represent the percentage differences on the uncertainties normalized to the independent sum of the two probes. For XC(WL, GC_{ph}) the reference is [WL] + [GC_{ph}], while for XC(WL, GC_{sp}) is [WL] + [GC_{sp}]. Note the opposite sign of the percentage differences for FoM and uncertainties.

on Ω_b, for which the gap between the two approaches decreases from more than 50% to less than 10% when 4 and 40 bins are used for the harmonic approach respectively. The uncertainty on n_s is quite sensitive to the number of bins too, and the difference between the two approaches ranges from 40% to 10% when the number of bins of the harmonic approach increases from 4 to 40.

Finally, the differences on the marginalized uncertainties on Ω_m and σ_8 are smaller, ranging from 20% to less than 5%.

4.2.4. Comparing XC(WL, GC_{sp}) with XC(WL, GC_{ph})

In EP-VII it has been shown that the XC(WL, GC_{ph}) cross-correlation considerably improves the constraints on the cosmological parameters. We found the same result in this work: in the optimistic scenario the Fisher matrix [WL + GC_{ph} + XC(WL, GC_{ph})] yields a FoM which is a factor of $\sim$ 5 higher than the one given by the [WL] + [GC_{ph}] Fisher matrix. This means that the percentage gain induced by the cross-correlation signal is about 400%. The XC(WL, GC_{sp}) cross-correlation has a smaller impact on the constraints, as the [WL + GC_{sp} + XC(WL, GC_{sp})] Fisher matrix produces a FoM at most $\sim$ 40% higher than the one of the [WL] + [GC_{sp}] combination. This is what happens when both GC_{ph} and GC_{sp} are treated in the baseline settings, i.e., when the standard shot noise of Eq. (37) is used for GC_{sp} and 10 tomographic bins are used for GC_{ph}. The effect of the shot noise on GC_{sp} can be seen from Fig. 11, which displays the percentage gain on the FoM of various combinations with respect to WL alone. The left panel refers to the standard GC_{sp} shot noise, the right panel refers to the alternative reduced noise of Eq. (41). When the noise is reduced, the Fisher matrix of the harmonic approach with 4 bins is already competitive with the one of the hybrid approach, yielding a gain of $\sim$ 300% relative to WL alone. The observable gaining the most from the noise reduction is the GC_{sp} auto-correlation, as the two curves of [WL+GC_{sp}] and [WL+GC_{sp}+XC(WL, GC_{sp})] converge towards each other as the number of bins increases.

A direct comparison between the gain coming from XC(WL, GC_{ph}) and XC(WL, GC_{sp}) cross-correlations is shown in Fig. 12. When GC_{sp} and GC_{ph} have the same shot noise level and the same redshift range, the effect of the XC(WL, GC_{sp}) on the constraints becomes comparable with the one of XC(WL, GC_{ph}).

Finally, Fig. 13 shows a comparison between the harmonic and hybrid approach. As can be seen from the plot, when increasing the number of bins in the harmonic case, the constraints approach that of the hybrid case.

Therefore, the conclusion is the same as that drawn for the direct comparison between the GC_{ph} and GC_{sp} auto-correlations. The shot noise and the redshift range of the galaxy catalog are what makes the differences between XC(WL, GC_{ph}) and XC(WL, GC_{sp}) in terms of constraining power.

5. The *Euclid* 6×2pt statistics

This section contains the main results of our paper, the Euclid full 6×2pt pt constraints and its comparison with the other approaches. Here we present the results of the combination of all the *Euclid* main probes: WL, GC_{ph}, and GC_{sp}. The starting point is the (photometric) 3×2pt statistics, defined as

$$3\times2\text{pt} \equiv [\text{WL} + \text{GC}_{\text{ph}} + \text{XC}(\text{WL}, \text{GC}_{\text{ph}})] \,. \tag{43}$$

In terms of this combination, the 6×2pt statistics can be expressed as

$$[6\times2\text{pt (harmonic)}] = [3\times2\text{pt} + \text{GC}_{\text{sp}} + \text{XC}(\text{WL}, \text{GC}_{\text{sp}}) + \text{XC}(\text{GC}_{\text{ph}}, \text{GC}_{\text{sp}})] \,, \tag{44}$$

for the full harmonic approach, and

$$[6\times2\text{pt (hybrid)}] = [3\times2\text{pt} + \text{XC}(\text{WL}, \text{GC}_{\text{sp}}) + \text{XC}(\text{GC}_{\text{ph}}, \text{GC}_{\text{sp}})] + [\text{GC}_{\text{sp}}(P_k)] \,. \tag{45}$$

for the hybrid approach.

The discussion will be focused on two main points:

- the importance of the cross-covariance between GC_{sp} and the 3×2pt statistics;
- the contribution to the constraints of the XC(GC_{ph}, GC_{sp}) and XC(WL, GC_{sp}) cross-correlations.

The cross-covariance between GC_{sp} and 3×2pt statistics is studied only in the harmonic approach, since in the hybrid approach it is neglected. The effect of the cross-correlations is assessed for both the harmonic and the hybrid approaches, and in both the pessimistic and optimistic scenarios defined in Table 4.

5.1. Impact of the GC_{sp} cross-covariances on parameter constraints

The impact on the constraints of the cross-covariance between GC_{sp} and 3×2pt is shown in the two panels of Fig. 14. The plot compares the constraints from the [3×2pt + GC_{sp}] and [3×2pt] + [GC_{sp}] combinations: in the former the GC_{sp}-3×2pt cross-covariance is taken into account, while it is not in the latter. The impact of the cross-covariance is almost the same in all the scenarios and decreases as the number of GC_{sp} bins increases, confirming the same trend observed in the two pairwise combinations GC_{ph}-GC_{sp} and WL-GC_{sp}. The percentage variations on the constraints are always below 10% (5%) with 4 (40) spectroscopic bins. The covariance almost always worsens the constraints with respect to considering GC_{sp} and 3×2pt as independent. The parameters whose uncertainties are affected the most by the GC_{sp}-3×2pt cross-covariance are Ω_b and h, with variations of $\sim$ 8% with 4 bins. When 40 bins are used for GC_{sp} the variation reduces to $\sim$ 2% for both parameters.

One of the most evident differences between the optimistic and the pessimistic scenario is the impact on the FoM, which is slightly higher in the pessimistic than in the optimistic setting. However the percentage difference is always below 5%, the worst case being the pessimistic scenario with 4 bins, where it is $\sim$ 4%. The percentage variation on the Ω_m uncertainty is at the sub-percent level in the optimistic scenario, while it is about at the percent level in the pessimistic scenario. The uncertainty on σ_8 is always smaller than 1% in the optimistic scenario, while it ranges from 4% to 1% in the pessimistic scenario.

5.2. Impact of the XC signals on parameter constraints

Here we discuss the impact on the constraints of the XC(GC_{ph}, GC_{sp}) and XC(WL, GC_{sp}) cross-correlations. The results in the harmonic approach is shown in Figs. 15 and 16, while the hybrid approach result is displayed in Fig. 17. The figures show the effect of the inclusion of the XC(WL, GC_{sp}) cross-correlation, the impact of the XC(GC_{ph}, GC_{sp}) cross-correlation, and the impact of both cross-correlations.

Harmonic approach For the harmonic approach, two Fisher matrices have been used as reference for the percentage differences: [3×2pt] + [GC_{sp}], where the 3×2pt statistics and GC_{sp} are combined as independent, and [3×2pt + GC_{sp}], where the cross-covariance between the two is accounted for (see Sect. 3.1). As explained in the previous section, these two combinations do not produce the same constraints (see Fig. 14), as the independent combination yields slightly better constraints.

We consider the two different Fisher matrices above since, when the cross-correlations are added in the harmonic approach, the cross-covariance between GC_{sp} and the 3×2pt statistics is always accounted for. Thus, on the one hand,

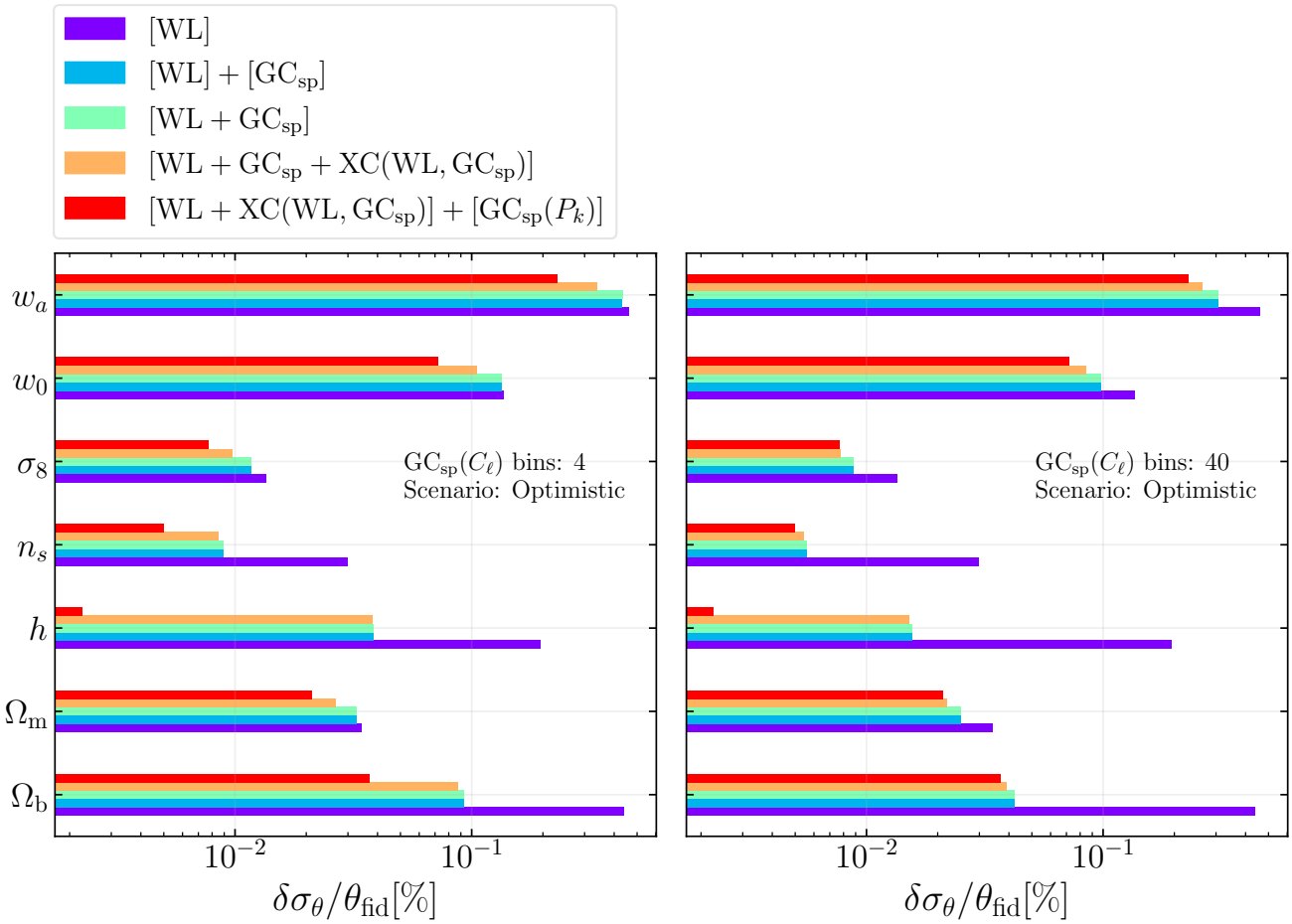

Fig. 13: Comparison between harmonic and hybrid harmonic-Fourier approaches for the case of WL × GC_{sp}.

we focus on the improvement due to the inclusion of the XC signals alone, and this is done when the Fisher matrix [3×2pt + GC_{sp} + XC(WL, GC_{sp})] is compared to the reference [3×2pt+GC_{sp}], and the same for [3×2pt+GC_{sp}+XC(WL, GC_{sp})] and [3×2pt + GC_{sp} + XC(WL, GC_{sp}) + XC(GC_{ph}, GC_{sp})] (see Fig. 15). In this case, the percentage differences are representative of the net effect of the cross-correlation signals on the constraints, which is expected to be always positive.

On the other hand, when the Fisher matrices comprising the XC's information are compared to the independent combination [3×2pt] + [GC_{sp}], we focus on the total effect, which not only contains the gain from the inclusion of the XC signals, but also the penalty from the cross-covariance between GC_{sp} and the 3×2pt statistics (see Fig. 16). This comparison is useful in order to evaluate the overall impact of the cross angular power spectra.

Harmonic approach – adding XC(WL, GC_{sp}) The net effect of the XC(WL, GC_{sp}) inclusion is shown in the left panels of Fig. 15, where the Fisher matrix [3×2pt+GC_{sp}+XC(WL, GC_{sp})] is compared to the reference [3×2pt + GC_{sp}]. The variation on the constraints due to the addition of XC(WL, GC_{sp}) is always about 0.01%-0.05%, with no significant differences between the optimistic and pessimistic scenarios. Therefore, it seems that this cross-correlation does not give any contribution to the constraints, i.e., it looks like the computation of the total [3×2pt + GC_{sp} + XC(WL, GC_{sp})] Fisher matrix is not useful to improve the *Euclid* performance. This might seem in contrast to what happens in the pairwise combination of WL and GC_{sp}, where the XC(WL, GC_{sp}) cross-correlation signal has a significant impact on the constraints. However, the latter case does not include the XC(WL, GC_{ph}) signal. Instead, in the case now under discussion of [3×2pt + GC_{sp} + XC(WL, GC_{sp})], the reference for the net effect here considered is [3×2pt + GC_{sp}], which contains the contribution of the XC(WL, GC_{ph}) cross-correlation, proven to be dominant.

From the above reasoning, it is also possible to infer the reason why the constraints from the [3×2pt+GC_{sp}+XC(WL, GC_{sp})] Fisher matrix are worse by 6% at most (see Fig. 16) than the ones from the independent combination [3×2pt] + [GC_{sp}]: the impact of the cross-correlation signal is so small that its possible improvements are completely dominated by the cross-covariance between GC_{sp} and the 3×2pt statistics (see Fig. 14), which is present when adding the cross signal, but not kept into account in the reference. Therefore, the total effect of the inclusion of XC(WL, GC_{sp}) in the combination of GC_{sp} with the 3×2pt statistic is to worsen the parameter constraints. However, while it has been just shown that the XC(WL, GC_{sp}) signal can be safely neglected, the cross-covariance between GC_{sp} and the 3×2pt statistic needs to be taken with caution.

Harmonic approach – adding XC(GC_{ph}, GC_{sp}) The middle panel of Fig. 15 shows the positive net effect of the XC(GC_{ph}, GC_{sp}) inclusion, which increases with the number of spectroscopic bins. This confirms the same behavior observed

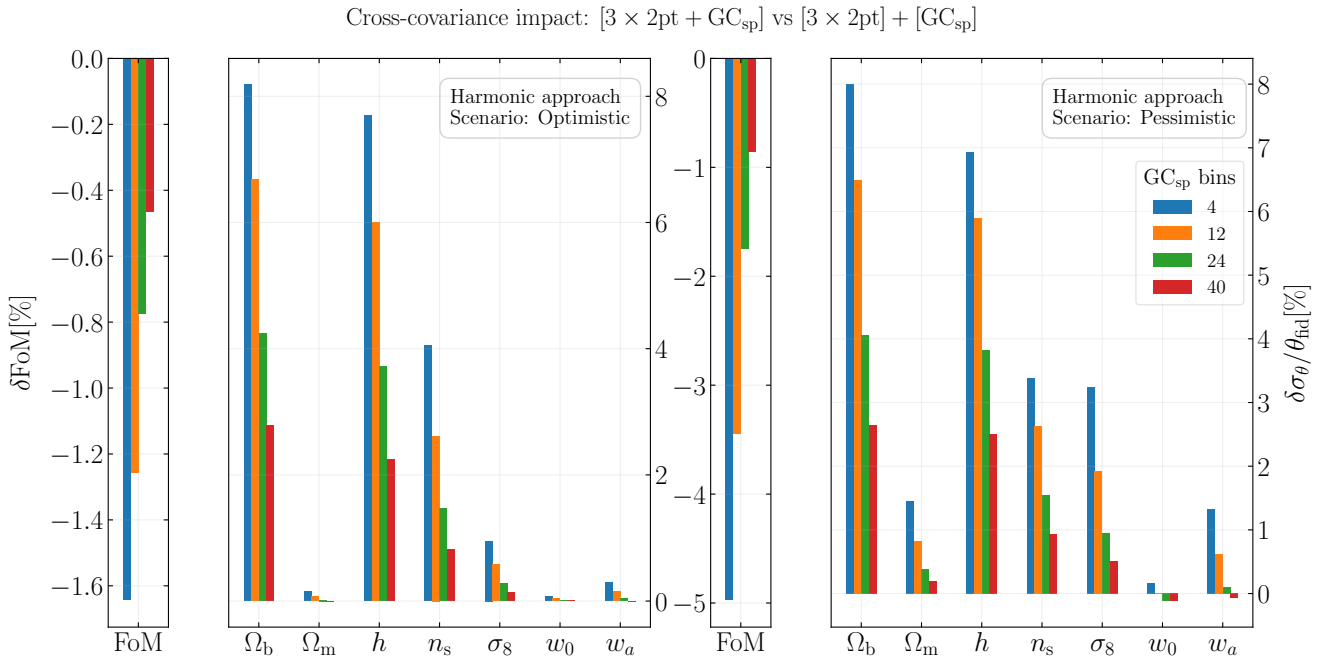

Fig. 14: Impact on FoM and marginalized 1-σ uncertainties, of cross covariances between GC$_{sp}$ and 3×2pt ([WL + GC$_{ph}$ + XC(WL, GC$_{ph}$)]), quantified with percentage differences on the constraints, in the optimistic (left) and pessimistic (right) scenarios. The reference for the percentage are the constraints of [3×2pt] + [GC$_{sp}$], where GC$_{sp}$ is considered as independent on the rest. Note the opposite sign of the percentage differences for FoM and uncertainties.

in the pairwise combination of GC$_{ph}$ and GC$_{sp}$. The gain on the FoM relative to the Fisher matrix [3×2pt + GC$_{sp}$] is about 1% for 4 bins, and increases up to 8-10% for 40 bins, with practically no differences between the optimistic and the pessimistic scenario. Fig. 16 shows that when the independent combination [3×2pt] + [GC$_{sp}$] is used as reference instead, the FoM variation due to the XC(GC$_{ph}$, GC$_{sp}$) inclusion is −2% (+7%) for 4 (40) GC$_{sp}$ bins. The small worsening at 4 bins is due to the fact that the positive contribution of the cross-correlation is canceled by the negative contribution of the GC$_{sp}$-3×2pt cross-covariance (see Fig. 14). In fact, this cross-covariance is taken into account in the Fisher matrix [3×2pt + GC$_{sp}$ + XC(GC$_{ph}$, GC$_{sp}$)], while it is not in the [3×2pt] + [GC$_{sp}$], which is used as the reference in this last case.

Analogously, the marginalized 1–σ uncertainties on the cosmological parameters exhibit a similar behavior, with no significant differences between the optimistic and the pessimistic scenarios. When using 4 spectroscopic bins the inclusion of the XC(GC$_{ph}$, GC$_{sp}$) cross-correlation produces a small improvement when the Fisher matrix [3×2pt + GC$_{sp}$] is used as reference. For a small number of bins, this positive contribution is in general compensated by cross-covariance effects when the percentage differences are referred to the [3×2pt] + [GC$_{sp}$] Fisher matrix. When using 40 spectroscopic bins the cross-correlation dominates and the cross-covariance effects become negligible, and the percentage differences become always positive, independently of the reference that is used. The parameters whose uncertainties decrease the most are Ω_b and h, gaining 15% and 10% respectively in the optimistic scenario, 10% and 5% in the pessimistic.

Therefore, the total effect of the inclusion of XC(GC$_{ph}$, GC$_{sp}$) in the combination of GC$_{sp}$ with the 3×2pt statistic depends on the chosen binning set, and may be dominant with respect to GC$_{sp}$-3×2pt cross-covariance effects for a large number of bins.

Harmonic approach – the 6×2pt statistics In the harmonic approach of Eq. (44), the constraints produced by the 6×2pt analysis are equivalent to the ones given by including the XC(GC$_{ph}$, GC$_{sp}$) alone. The percentage differences between the constraints from the 6×2pt Fisher matrix and the [3×2pt + GC$_{sp}$] Fisher matrix are reported in Fig. 15. These are indistinguishable from the ones which refer to the impact of the XC(GC$_{ph}$, GC$_{sp}$) cross-correlation only with respect to [3×2pt + GC$_{sp}$]. This is expected, since in the above paragraphs it has been shown that XC(WL, GC$_{sp}$) provides a negligible contribution with respect to XC(GC$_{ph}$, GC$_{sp}$).

Hybrid approach The contribution of the XC(WL, GC$_{sp}$) and XC(GC$_{ph}$, GC$_{sp}$) signals in the hybrid approach is reported in Fig. 17. In this case the reference used is always the independent combination [3×2pt] + [GC$_{sp}$(P_k)], since in the hybrid approach the cross-covariance between GC$_{sp}$(P_k) and the 3×2pt is neglected.

Hybrid approach – adding XC(WL, GC$_{sp}$) In the hybrid approach the impact of the XC(WL, GC$_{sp}$) cross-correlation on the constraints from [3×2pt + XC(WL, GC$_{sp}$)] + [GC$_{sp}$(P_k)], relative to [3×2pt] + [GC$_{sp}$(P_k)], is negligible, being always less than 0.05%, both in the optimistic and in the pessimistic scenarios. This result is similar to what is found with the harmonic approach, in which we consider the comparison of [3×2pt + GC$_{sp}$ + XC(WL, GC$_{sp}$)] with respect to [3×2pt + GC$_{sp}$], to isolate the impact of XC(WL, GC$_{sp}$). This is expected, since there are no differences in the 3×2pt between the two approaches, and, in particular, the XC(WL, GC$_{ph}$) cross-correlation is computed in the same way in the two cases.

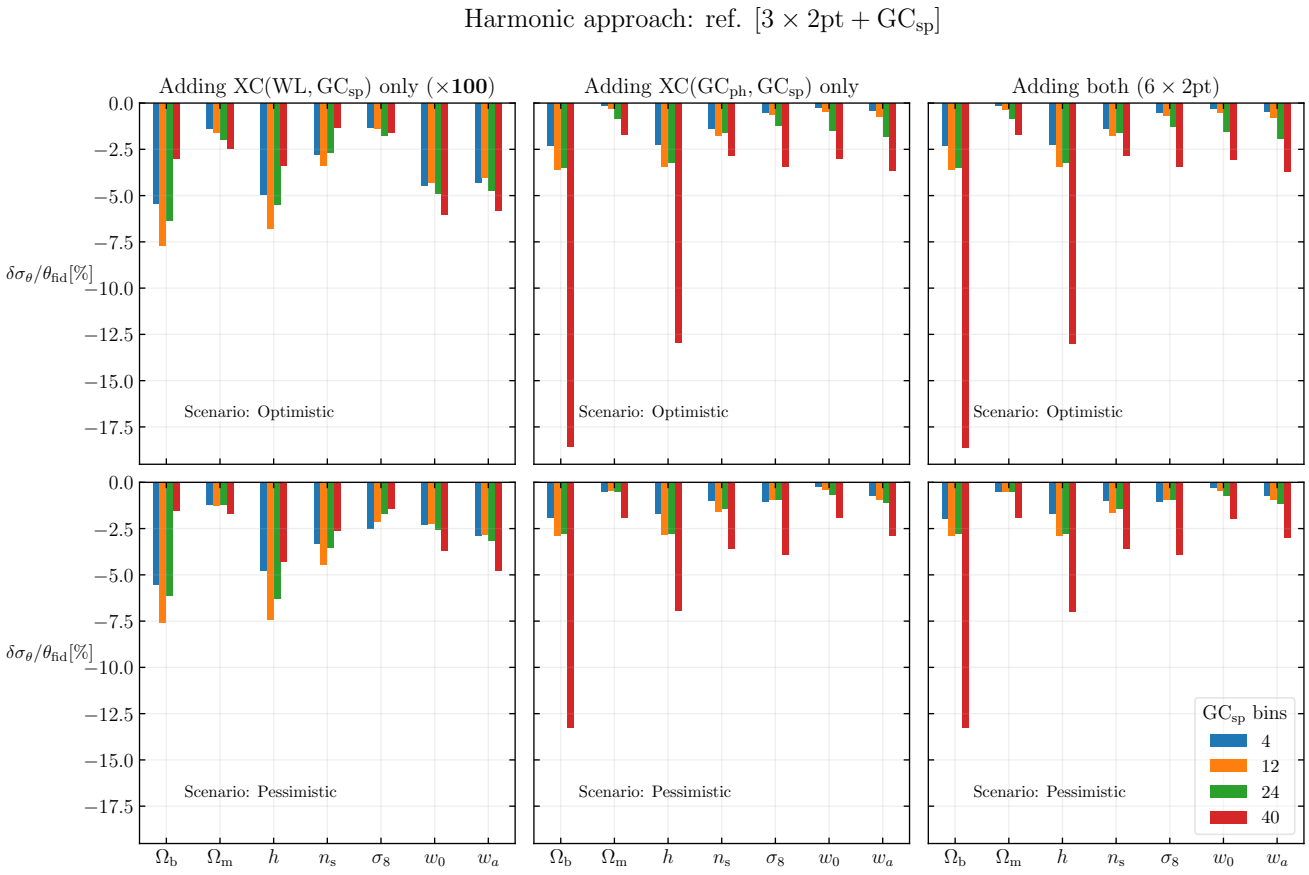

Fig. 15: Impact of the XC(GC$_{ph}$, GC$_{sp}$) and XC(WL, GC$_{sp}$) cross-correlations on marginalized 1–σ uncertainties, with respect to the constraints given by the [3×2pt + GC$_{sp}$] Fisher matrix, in which the cross-covariance between 3×2pt statistics and GC$_{sp}$ is taken into account. The top panels refer to the optimistic scenario, while the bottom panels refer to the pessimistic one. The percentage differences related to XC(WL, GC$_{sp}$) have been multiplied by 100 to make them visible when using a single scale on the y axis.

Hybrid approach – adding XC(GC$_{ph}$, GC$_{sp}$) In the hybrid approach the impact of the XC(GC$_{ph}$, GC$_{sp}$) cross-correlation on the constraints from [3×2pt + XC(GC$_{ph}$, GC$_{sp}$)] + [GC$_{sp}$(P_k)], relative to [3×2pt] + [GC$_{sp}$(P_k)], is slightly smaller than in the harmonic one with 4 spectroscopic bins. Fig. 17 shows that the absolute percentage differences on all constraints is always below 2%. The gain on the FoM is ∼ 1% both in the optimistic and the pessimistic scenario. The parameters whose uncertainties are affected the most are Ω_b and h, with a gain of 1.5% at most in the pessimistic scenario, and less than 0.5% in the optimistic scenario.

Hybrid approach – the 6×2pt statistics The constraints given by the hybrid 6×2pt statistics are similar to the ones given by the inclusion of the XC(GC$_{ph}$, GC$_{sp}$) cross-correlation only. This is manifest in Fig. 17. Nonetheless, in the hybrid approach the inclusion of the XC(GC$_{ph}$, GC$_{sp}$) cross-correlation has a negligible impact on the constraints, as discussed in the above paragraph. Therefore, the Fisher matrix of the hybrid 6×2pt statistics produces constraints that are almost equivalent to the [3×2pt] + [GC$_{sp}$(P_k)] Fisher matrix.

5.3. The 6×2pt statistics: hybrid approach vs harmonic approach

For the 6×2pt statistics the hybrid approach performs better than the harmonic one, especially when a small number of spectroscopic bins is used for the latter. The comparison of the two approaches is reported in Fig. 18. In this case, the reference adopted is the Fisher matrix of the harmonic approach, Eq. (44). The hybrid approach produces a FoM that is 20% (40%) larger than the harmonic one in the optimistic (pessimistic) scenario, when 4 spectroscopic bins are used for the latter. When using 40 bins, the harmonic approach performs instead slightly better (∼ 6%) than the hybrid one in the optimistic scenario, while it is equivalent to it in the pessimistic scenario.

Regarding the marginalized 1–σ uncertainties on the dark energy parameters, w_0-w_a, the hybrid approach always provides better constraints than the harmonic one, regardless of the number of spectroscopic bins used for the latter. However, the harmonic approach with 40 bins produces a slightly higher FoM than the hybrid one in the optimistic scenario.

Fig. 18 shows that the hybrid approach performs drastically better in constraining h, producing a 1–σ uncertainty on it which is always more than 70% smaller than the one in the harmonic approach. The hybrid approach gives better uncertainties than the harmonic one for n_s and Ω_b too. For n_s the uncertainty of the hybrid approach is always smaller than the one of the harmonic approach by 30-40%. For Ω_b the hybrid approach gives a 60% smaller uncertainty than the harmonic approach with 4 bins, while the difference is about 20% with 40 bins. Concerning the uncertainty on Ω_m the two approaches produce results that are always comparable within 5%. Finally, on σ_8 the harmonic approach with 12 bins performs slightly better than the

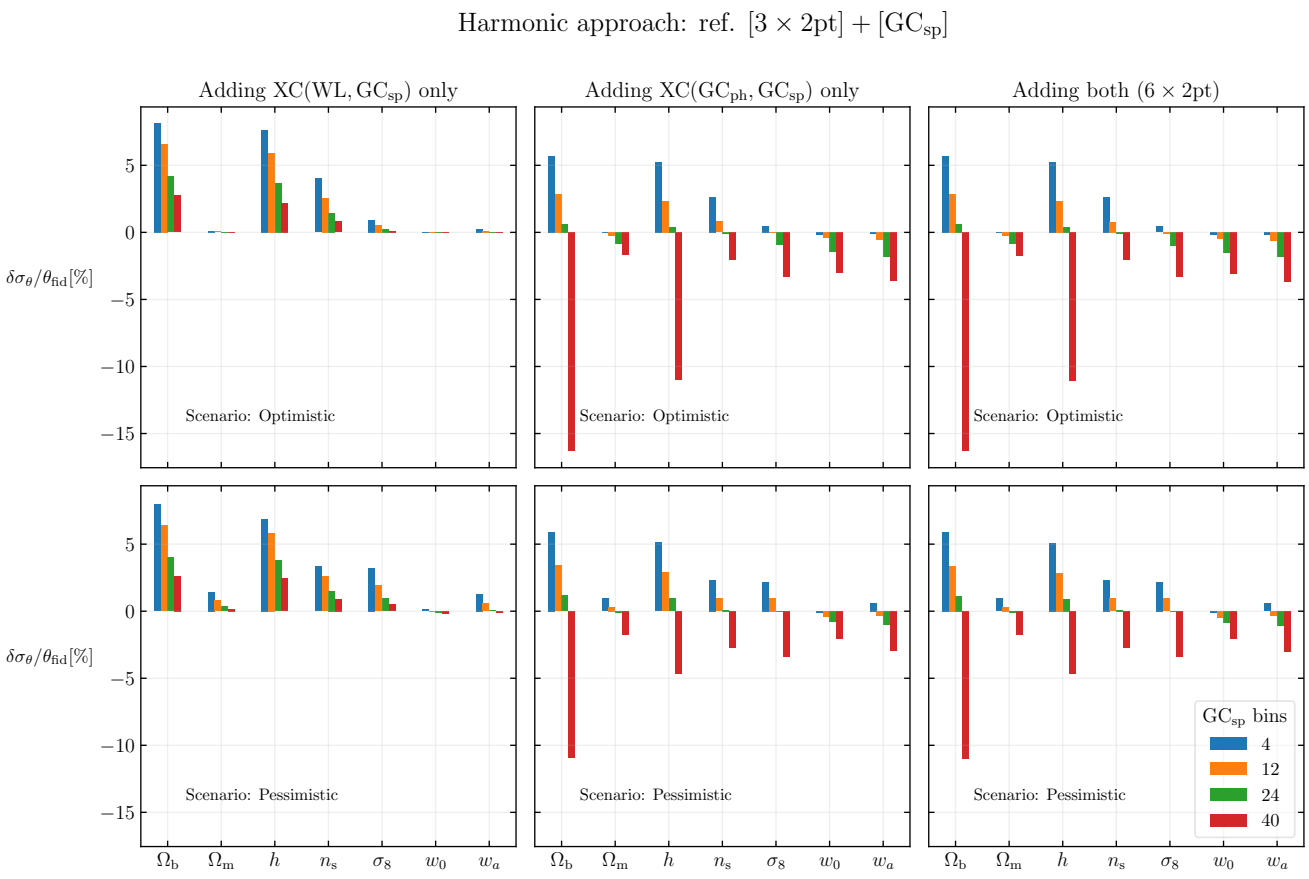

Fig. 16: Impact of the XC(GC$_{ph}$, GC$_{sp}$) and XC(WL, GC$_{sp}$) cross-correlations on marginalized 1–σ uncertainties, with respect to the constraints given by [3×2pt] + [GC$_{sp}$], 3×2pt and GC$_{sp}$ are combined as independent. The top panels refer to the optimistic scenario, while the bottom panels refer to the pessimistic one.

hybrid one. In the optimistic scenario the uncertainties on σ_8 are always comparable, while in the pessimistic case the harmonic approach produces a 10% smaller uncertainty when using 40 tomographic bins.

6. Main results and conclusions

In this work we presented the results of the first *Euclid* forecasts that include all the pairwise correlations between the main probes: weak lensing (WL), photometric galaxy clustering (GC$_{ph}$), and spectroscopic galaxy clustering (GC$_{sp}$). We have studied these correlations from two points of view. First, off-diagonal terms of the covariance matrix, the cross-covariances, that account for the statistical correlation between two different probes. Second, as additional observables, the cross-correlation signals which can be sensitive to cosmological parameters.

This work is a natural extension of the *Euclid* IST forecast EP-VII, considering WL and GC$_{ph}$ and their correlation in the 2D harmonic domain. The GC$_{sp}$ was instead studied in the 3D Fourier domain, and to a first approximation was assumed to be independent on the other two probes. Here we extend the harmonic formalism also to GC$_{sp}$, with the aim of including the XC(GC$_{ph}$, GC$_{sp}$) and XC(WL, GC$_{sp}$) correlations in the analysis as well. Differently, a work complementary to this one introduces a new data vector, essentially the ratio of the correlation of the two samples. Since this data set is free from sampling variance, it aims to achieve a significant improvement in the final constraints on the cosmological parameters Dournac et al. (2024).

We have considered two different approaches to include the cross-correlations in the analysis: the harmonic approach and the hybrid approach.

In the harmonic approach all the observables – the two-point correlation functions – are treated in the harmonic domain, i.e., using the $C(\ell)$'s formalism. This approach allows us to naturally include all cross-covariances between the observables, computed via Eq. (23). Nonetheless, it has the disadvantage of significantly lowering the constraining power of GC$_{sp}$, since the integral along the line of sight prevents to fully exploit the accurate radial information provided by the spectroscopic clustering. In order to recover such information, we tried to refine the tomographic binning of the projected GC$_{sp}$, from 4 bins (the baseline setting) up to a maximum of 40 bins, but in any case we neglected RSD in the angular GC$_{sp}$ power spectra.

In the hybrid approach, all the observables are studied in the harmonic domain – including XC(WL, GC$_{sp}$) and XC(GC$_{ph}$, GC$_{sp}$) – except for the GC$_{sp}$ auto-correlation function. We have considered it as an independent observable, adding the GC$_{sp}$ Fisher matrix that had been computed in EP-VII, using the 3D Fourier power spectrum as observable. The main advantage of this approach is that it fully exploits the potential of GC$_{sp}$, keeping the information from radial BAO and RSD available thanks to accurate spectroscopic redshift measurements. At the same time the XC(GC$_{ph}$, GC$_{sp}$) and XC(WL, GC$_{sp}$) cross-correlations are correctly included in the analysis as harmonic

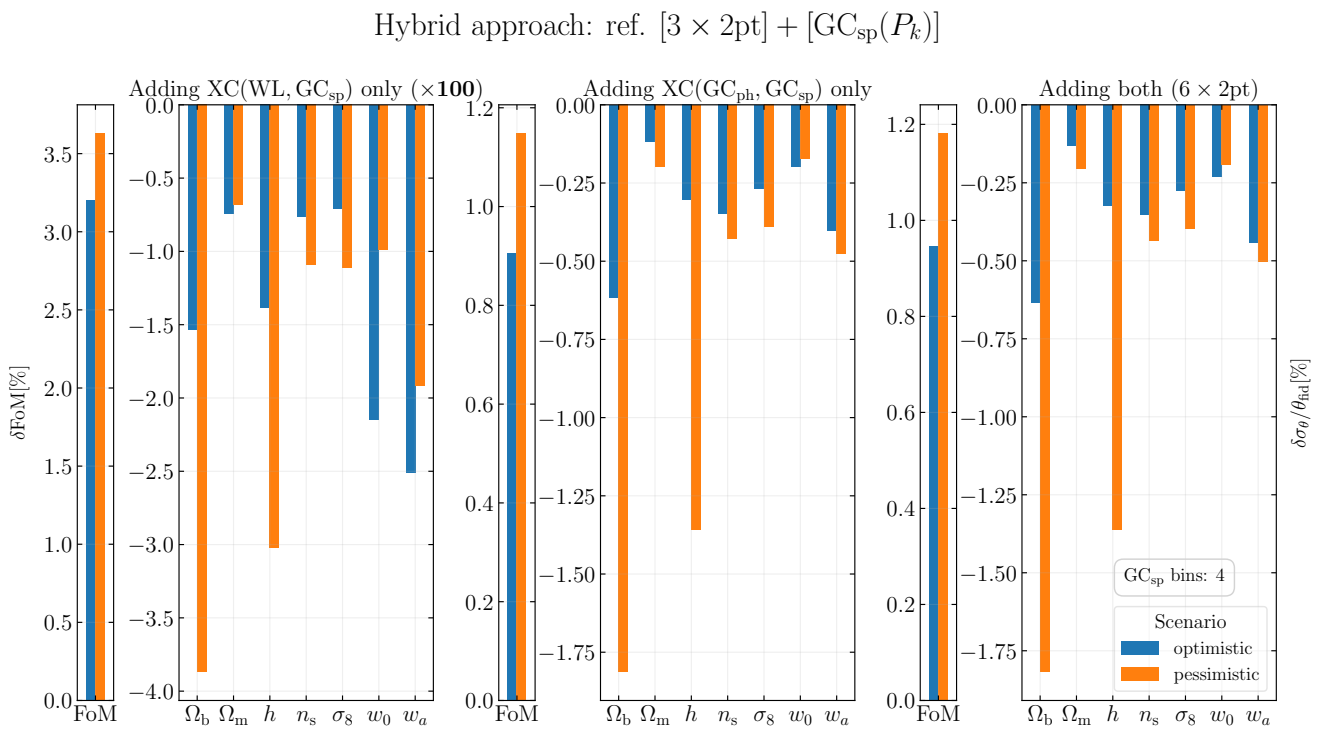

Fig. 17: Impact on FoM and marginalized 1–σ errors, of the XC($\mathrm{GC_{ph}}$, $\mathrm{GC_{sp}}$) and XC(WL, $\mathrm{GC_{sp}}$) cross-correlations in the hybrid approach. The reference for the percentage differences is [WL + $\mathrm{GC_{ph}}$ + XC(WL, $\mathrm{GC_{ph}}$)] + [$\mathrm{GC_{sp}}(P_k)$]. In any case the cross-correlations are always considered to be covariant with the 3×2pt statistics observables. The percentage differences in the left panel have been multiplied by 10, to make them visible to the naked eye. Note the opposite sign of the percentage differences for FoM and uncertainties.

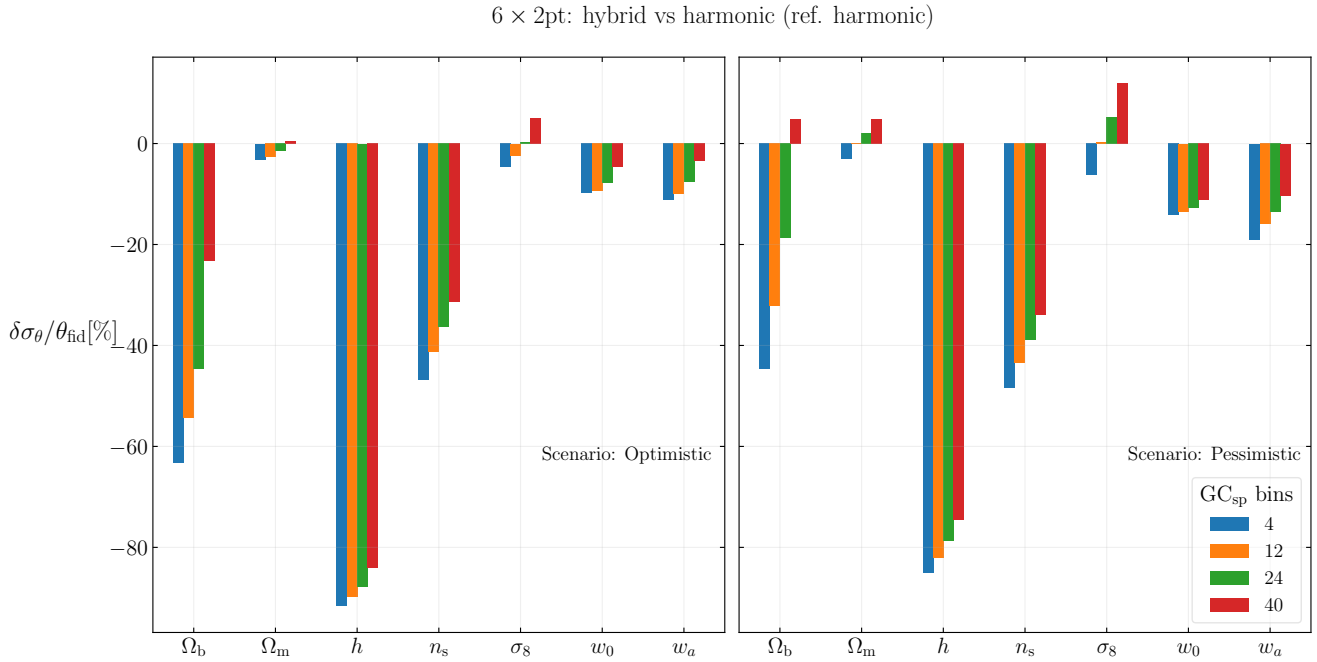

Fig. 18: Comparison between marginalized 1–σ uncertainties of the hybrid 6×2pt and the harmonic 6×2pt statistics, quantified using percentage differences taking the latter as reference.

two-point functions, i.e., $C(\ell)$'s. However, this approach comes with a drawback.

It is not obvious how to compute the cross-covariance terms between the 3D $\mathrm{GC_{sp}}$ auto-correlation and the 2D 3×2pt observables. Therefore, according to the conclusions from the analysis in the harmonic domain (which correctly accounts for the projected part of such cross-covariances), indicating that the impact of this "projected" cross-covariance on the *Euclid* performance is negligible, and assuming that it is a good approximation of the full 3D-2D covariance (especially because the 3×2pt statistics only depends on transverse modes), in the hybrid approach we neglect the cross-covariances between 3D and 2D probes. How-

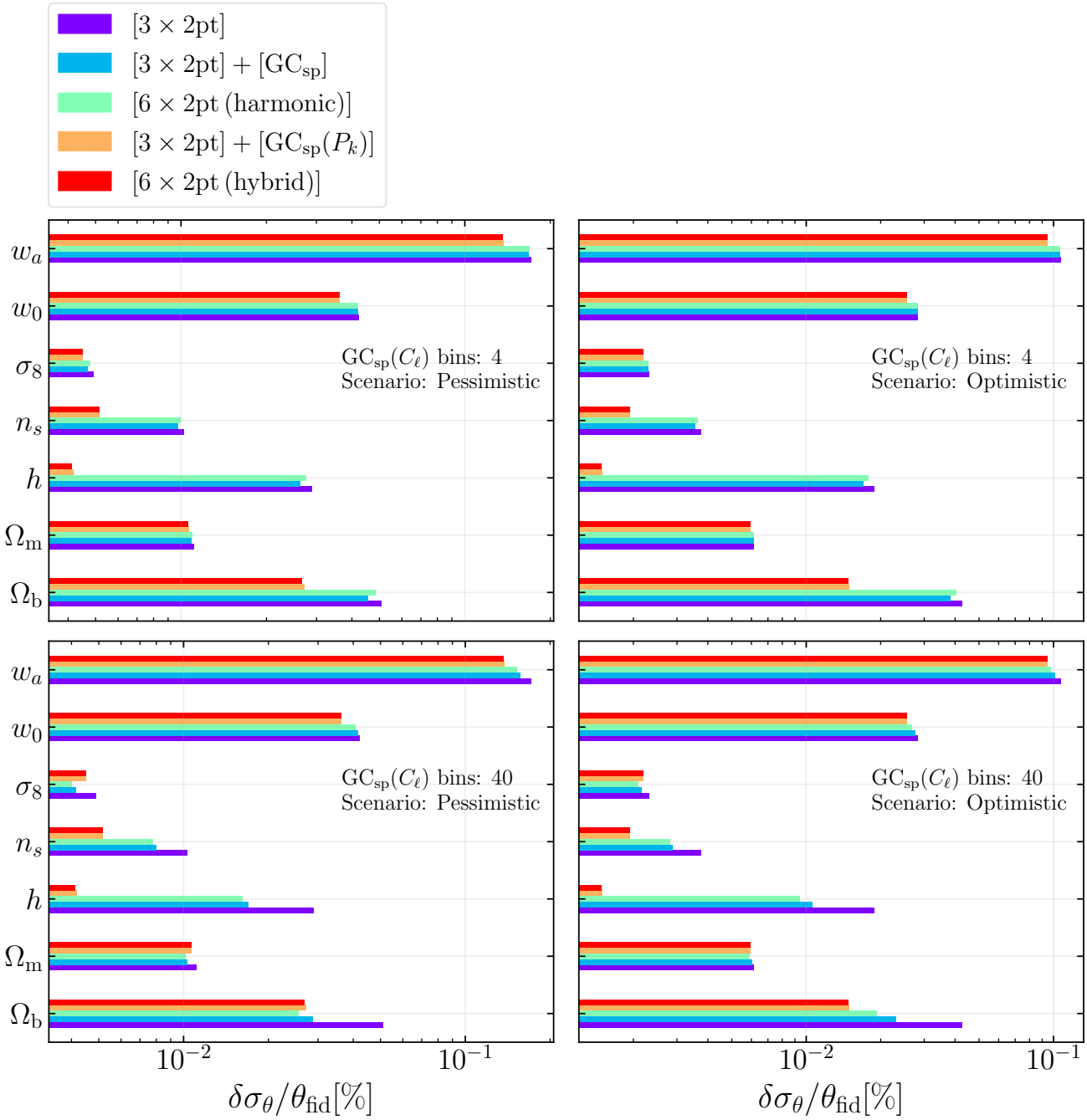

Fig. 19: Comparison between harmonic and hybrid approaches for the case of 6×2pt statistics. The left panels refer to the pessimistic scenario, while the right panels refer to the optimistic one.

ever, we would like to point out that the methodology presented in this paper is not meant to be used with forthcoming Euclid data, but as a tool to forecast the impact of cross-correlations and covariances among the Euclid photometric and spectroscopic probes.

We summarize the results of our analysis in the three cases considered: the combination of GC$_{ph}$ and GC$_{sp}$, the combination of WL and GC$_{sp}$, and the so-called 6×2pt, i.e., the full combination of WL, GC$_{ph}$, GC$_{sp}$ altogether. In the latter case – which is the most interesting one for the *Euclid* data analysis – we present the results in an optimistic and pessimistic scenarios. Instead, for the two pairwise combinations GC$_{ph}$-GC$_{sp}$ and WL-GC$_{sp}$, we report the results for the optimistic scenario alone.

Combination of GC$_{ph}$ *and* GC$_{sp}$ In the harmonic approach, the full analysis, [GC$_{ph}$ + GC$_{sp}$ + XC(GC$_{ph}$, GC$_{sp}$)], i.e., including the cross-covariance and cross-spectrum, provides a FoM of 69 in the baseline setting of 4 spectroscopic bins. For the combination of GC$_{ph}$ and GC$_{sp}$, the cross-covariance between the two can be considered practically negligible, as it does not change the uncertainties on the cosmological parameters by more than 6% and the FoM (computed considering only the 3×2pt statistics associated with GC) by more than 3%, with respect to the refer-

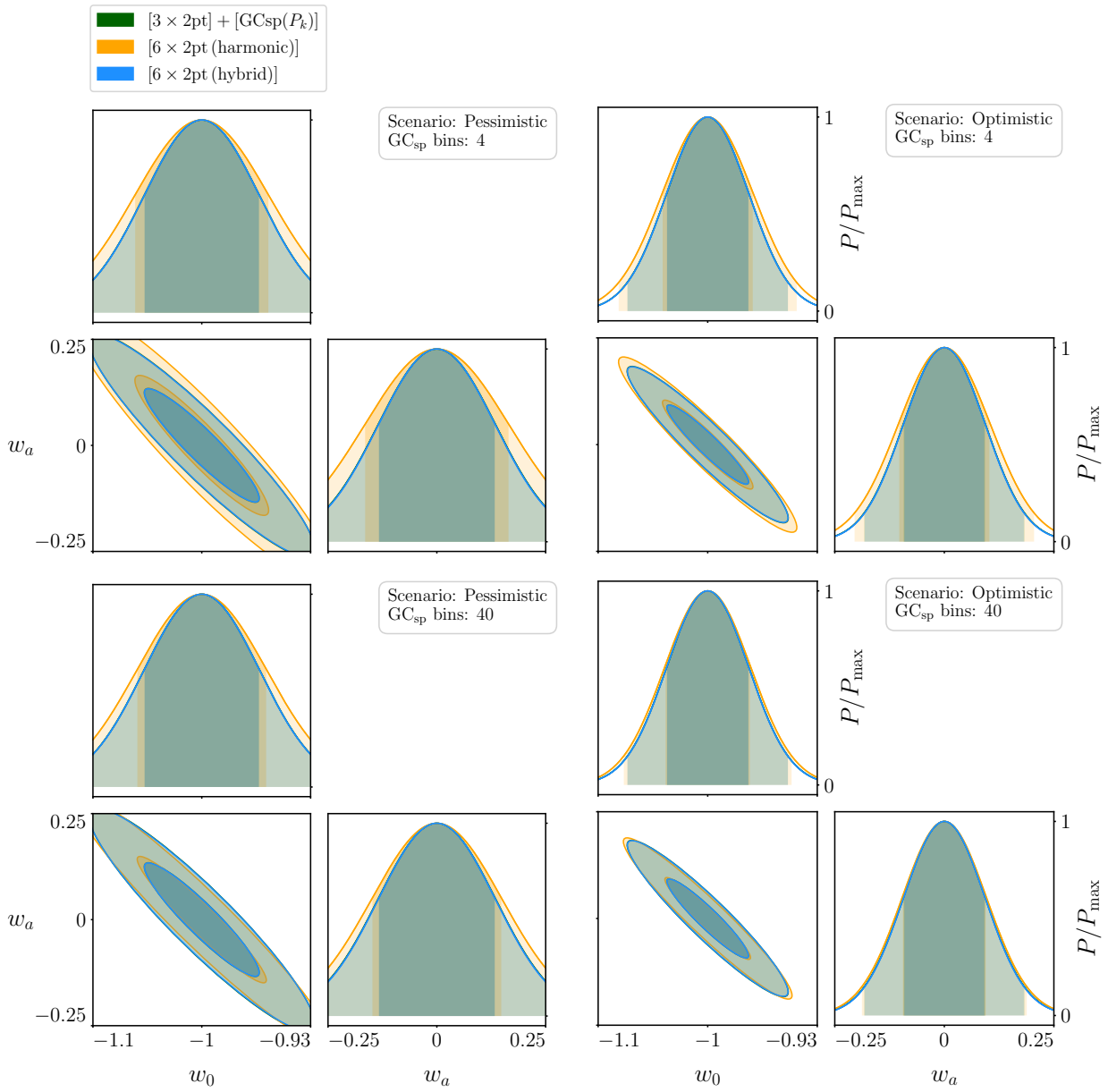

Fig. 20: Contour plots showing the comparison between the two approaches in the case of the 6×2pt statistics.

ence combination in the harmonic domain, [GC_{ph}] + [GC_{sp}], of the two probes taken as independent. In the harmonic approach, the XC(GC_{ph}, GC_{sp}) cross-correlation signal starts to be significant only when using 40 bins, yielding a maximum FoM of 153, which is 38% higher than for the [GC_{ph}] + [GC_{sp}] combination. Regarding the uncertainties on w_0 and w_a, the improvement given by the XC(GC_{ph}, GC_{sp}) cross-correlation is 5 and 6% respectively in the baseline 4 bins setting, while it is 23% and 25% when using 40 bins. The gain on the uncertainties on the other parameters is less than 5% with 4 bins and ranges from 10% to 20% with 40 bins.

In the hybrid approach, the full analysis, [GC_{ph} + XC(GC_{ph}, GC_{sp})] + [$GC_{sp}(P_k)$], including the cross-spectrum but neglecting the cross-covariance, gives instead a FoM of 234, which is much higher than in the harmonic case. However, in the hybrid case the impact of the XC(GC_{ph}, GC_{sp}) signal is negligible, since combining the probes as independent, [GC_{ph}] + [$GC_{sp}(P_k)$], provides a FoM of 230, which is only 1.7% lower than in the full case. The gain on the marginalized uncertainties is even smaller, being always less than 1%. Therefore, it is possible to conclude that the XC(GC_{ph}, GC_{sp}) cross-correlation can be neglected in the combination of GC_{ph} with GC_{sp}.

Combination of WL *and* GC_{sp} In the harmonic approach, the full analysis, [WL + GC_{sp} + XC(WL, GC_{sp})], i.e., including the cross-covariance and cross-spectrum, provides a FoM of 103 in the baseline setting of 4 spectroscopic bins. For the combination of WL and GC_{sp}, the cross-covariance is even more negligible than for the GC case above, impacting the constraints always by less than 1% with respect to the independent combination, [WL] + [GC_{sp}], computed in the harmonic domain. In this domain, the XC(WL, GC_{sp}) cross-correlation signal improves the constraints almost independently of the number of tomographic bins used for GC_{sp}. The percentage gain on the corresponding

Table 7: FoM of the 6×2pt statistics in the harmonic and hybrid approaches.

bins	Fisher matrix	FoM	ΔFoM	ΔFoM (%)
	6×2pt FoM forecasts			
	Optimistic scenario			
4	[3×2pt] + [$GC_{sp}(P_k)$]	1216.16	–	–
	6×2pt hybrid	1227.69	11.53	+0.95%
	6×2pt harmonic	1018.43	−197.73	−16.26%
12	6×2pt harmonic	1073.31	−142.85	−11.75%
24	6×2pt harmonic	1151.13	−65.03	−5.35%
40	6×2pt harmonic	1296.44	80.28	+6.60%
	Pessimistic scenario			
4	[3×2pt] + [$GC_{sp}(P_k)$]	549.37	–	–
	6×2pt hybrid	555.87	6.50	+1.18%
	6×2pt harmonic	379.85	−169.52	−30.86%
12	6×2pt harmonic	434.00	−115.37	−21.00%
24	6×2pt harmonic	486.40	−62.97	−11.46%
40	6×2pt harmonic	550.82	1.45	+0.26%

Notes. The ΔFoM columns quantify the differences with respect to the [3×2pt] + [$GC_{sp}(P_k)$] combination, which is used as reference to assess the impact on the FoM of the XC(GC_{ph}, GC_{sp}) and XC(WL, GC_{sp}) cross-correlations.

FoM, produced by the XC inclusion, is 38% and 33% with 4 and 40 bins, respectively. This seemingly counterintuitive trend has been explained in Sect. 4.2: it is due to the fact that the performance of the harmonic GC_{sp} auto-spectrum alone improves faster than for XC(WL, GC_{sp}) when refining the spectroscopic binning. The value of the FoM provided by the full combination, [WL + GC_{sp} + XC(WL, GC_{sp})], increases to 188 with 40 bins, i.e., by ∼ 45% with respect to the baseline 4-bin setting.

The XC(WL, GC_{sp}) signal also improves the uncertainties on Ω_m and σ_8, by 12%–18% for the former and 11%–16% for the latter. The error decrease for Ω_b and n_s ranges instead from 5% to 8% for the former and from 5% to 2% on the latter. Finally, the uncertainty on h is the only exception to this trend, with an improvement only by 1%–4%.

In the hybrid approach, the full analysis, [WL + XC(WL, GC_{sp})] + [$GC_{sp}(P_k)$] provides a FoM of 183, which is comparable to the harmonic case for the 40-bin setting, but is ∼ 56% larger than the 4-bin case. In the hybrid approach, the impact of the XC(WL, GC_{sp}) signal is not negligible, since the FoM is 15% larger than for the independent combination, [WL] + [$GC_{sp}(P_k)$], of the two probes. The improvements on the marginalized uncertainties are all in the range between 4% and 8%, with no significant differences between the parameters. The uncertainty on Ω_m improves the most, by about 8%, while the smallest improvement is on n_s, with an error decreasing by slightly less than 5%.

Combination of WL, GC_{ph}, GC_{sp} *and the 6×2pt statistics* In the harmonic approach, the full 6×2pt analysis, Eq. (44), i.e., including all cross-covariances and cross-spectra, provides a *Euclid* FoM of 1018 in the baseline 4-bin setting. The overall impact of the cross-covariances between the angular GC_{sp} and the 3×2pt statistics, with respect to the independent combination [3×2pt] + [GC_{sp}], is slightly higher than for the pairwise combinations GC_{ph}-GC_{sp} and WL-GC_{sp}, reported above. This is presumably due to the cumulative effect of three independent off-diagonal covariance blocks. However, the increase on parameter uncertainties is never larger than 8%, as Fig. 14 shows.

Concerning the impact of the cross-correlation signals between GC_{sp} and 2D probes, this is always negligible both in the harmonic and hybrid approaches. Here below we summarize the different contributions.

- XC(WL, GC_{sp}) case:
  - In the harmonic approach, the XC(WL, GC_{sp}) is definitely negligible both in the optimistic and pessimistic scenarios: it always improves parameter constraints by less than 0.05%, with respect to the independent combination, [3×2pt] + [GC_{sp}], computed in the same approach. This is because the contribution brought by the XC(WL, GC_{sp}) is dominated by the XC(WL, GC_{ph}), which is already present in the Fisher matrix used as reference.
  - In the hybrid approach, similarly the XC(WL, GC_{sp}) cross-correlation improves both the FoM and the uncertainties by always less than 0.05% with respect to the independent [3×2pt] + [$GC_{sp}(P_k)$] combination.
- XC(GC_{ph}, GC_{sp}) case:
  - In the harmonic approach, the performance improvement due to XC(GC_{ph}, GC_{sp}) is always below 5% when compared to [3×2pt + GC_{sp}], while it is dominated by the covariance effect when compared to [3×2pt] + [GC_{sp}]. The only exception is when using 40 bins for GC_{sp}: in this case the FoM improves by about 10%, while the marginalized uncertainties on Ω_b and h decrease by ∼ 15%. The uncertainties on the other parameters decrease by always less than 5% instead.
  - In the hybrid approach, the XC(GC_{ph}, GC_{sp}) improvement is always below 2%, for both FoM and uncertainties with respect to the independent combination [3×2pt] + [$GC_{sp}(P_k)$], since, in this case, only the baseline setting of 4 spectroscopic bins can be used for consistency with the official 3D spectroscopic galaxy clustering approach.

In general, the effect of the XC(GC_{ph}, GC_{sp}) is larger than for XC(WL, GC_{sp}), both in the optimistic and pessimistic scenarios and both in the harmonic and in the hybrid approaches. For this reason the 6×2pt statistics is essentially equivalent to adding XC(GC_{ph}, GC_{sp}) only. Nonetheless, the improvement on the constraints produced by the XC(GC_{ph}, GC_{sp}) cross-correlation is almost always smaller than 10%.

Finally, looking at the absolute performance, the values of the FoM are reported in Table 7, and summarized as follows:

1. the independent combination in flat space, [3×2pt] + [$GC_{sp}(P_k)$], from EP-VII is taken as reference, and it gives a FoM of 1216 (549) in the optimistic (pessimistic) scenario;
2. in the harmonic domain, the angular 6×2pt statistics with 40 spectroscopic bins provides a total FoM of 1296 (550) in the optimistic (pessimistic) scenario, which is only 6.6% (0.26%) better than 1. When using the standard 4 spectroscopic bins it gives a FoM of 1018 (380) in the optimistic (pessimistic) scenario, which instead is 15% (31%) worse than 1.
3. The hybrid 6×2pt statistics is essentially equivalent to the [3×2pt] + [$GC_{sp}(P_k)$] case, with a FoM of 1228 (556) in the

optimistic (pessimistic) scenario, i.e., only 1.18% (0.95%) better than 1.

Therefore, we can affirm that the XC(GC_{ph}, GC_{sp}) and XC(WL, GC_{sp}) cross-correlations have negligible impact on the *Euclid* performance when added to the combination of GC_{sp} and the 3×2pt statistics, both in the harmonic and hybrid approaches.

In conclusion, either the cross-covariances (here computed only in the harmonic approach) or the cross-correlations (computed both in the harmonic and hybrid approaches) between the two *Euclid* main probes, i.e., GC_{sp} and the so-called 3×2pt statistics, have a negligible impact on the cosmological parameter constraints and, therefore, on the *Euclid* performance. Regarding the cross-covariance impact, this issue was addressed also in Taylor & Markovič (2022), but following a different approach: they derived an analytical expression for the Gaussian cross-covariance between the 3×2pt statistics and the GC_{sp} multipoles. Also this approach leads to a negligible impact of the cross-covariance, hence corroborating our findings.

In the case of the hybrid approach, we attribute this result to the effect of the XC(WL, GC_{ph}) cross-correlation which is dominant with respect to the other cross-correlations, and to the higher performance of the full anisotropic 3D GC_{sp} probe with respect to the projected one.

In the case of the 2D harmonic approach, we attribute this result to two main limitations of the 2D projected GC_{sp} approximation: the high shot noise and the limited redshift range of the sample, with respect to the 3×2pt statistics, together with the suppression of radial information, as RSD. We have found that, under two conditions, GC_{sp} in harmonic space becomes equivalent to GC_{ph} in terms of constraining power, as it can be seen from Fig. 7. The first condition is to reduce the shot noise of GC_{sp} to the same level of GC_{ph}. The second is to restrict the tomographic bins of GC_{ph} to the 4 photometric bins contained in the GC_{sp} redshift range. Under these same conditions, XC(WL, GC_{sp}) and XC(WL, GC_{ph}) equally contribute to the *Euclid* performance, as we show in Fig. 12. Nonetheless, these conditions are not realistic.

Finally, we would like to point out to the reader that in our work we focused on the impact of the Euclid photometric and spectroscopic probes on the cosmological parameters' determination, neglecting the implications for systematics. For instance, as studied in Newman (2008), it is possible to use the photometric and spectroscopic cross-correlations to calibrate the photometric galaxy density. On the same side, with a 6×2pt pt analysis it is possible to perform the so-called "shear-ratio test" (Jain & Taylor 2003); although there is not a great deal of cosmological information encoded in these data, they can be used to calibrate the shears and redshifts of the photometric sources (Johnson et al. 2017).

Future extensions of this work will overcome some approximations that have been made. First, we have computed the $C(\ell)$'s making use of the Limber approximation. It has been shown in Fang et al. (2020) that this may result in a biased analysis. Using the exact expression for computing the angular power spectra would help to prevent this issue. Second, we have computed the $C(\ell)$'s covariance with Eq. (23) as in EP-VII, and this formula only accounts for the Gaussian contributions. Comparison with covariances estimated from *N*-body simulations showed that the inclusion of non-Gaussian effects may be necessary in order to reach a better agreement with simulations (Krause et al. 2017). In order to obtain a more realistic signal-to-noise ratio we have performed some forecasts including the SSC contribution as computed in Lacasa & Grain (2019): the results of this study are not modified, as we found both the cross-covariance and the cross-correlation between the photometric and spectroscopic probes to be negligible even in this scenario. Third, in what we have called the hybrid approach we have neglected the covariances between the Fourier GC_{sp} auto-correlation and the 3×2pt probe. Our calculations in harmonic space suggest that these terms may be negligible. Nonetheless, providing analytical modeling of these terms when GC_{sp} is studied in 3D Fourier space would surely help to confirm our findings.

Acknowledgements. MB acknowledges financial support from the ASI agreement n. I/023/12/0 "Euclid attività relativa alla fase B2/C". SC acknowledges support from the Italian Ministry of University and Research (MUR), PRIN 2022 'EXSKALIBUR – Euclid-Cross-SKA: Likelihood Inference Building for Universe's Research', Grant No. 20222BBYB9, CUP C53D2300131 0006, and from the European Union – Next Generation EU. SD acknowledges support from the Italian Ministry of University and Research, PRIN 2022 'LaScaLa – Large Scale Lab', (grant no. 20222JBEKN), and from the European Union – Next Generation EU. The Euclid Consortium acknowledges the European Space Agency and a number of agencies and institutes that have supported the development of *Euclid*, in particular the Agenzia Spaziale Italiana, the Austrian Forschungsförderungsgesellschaft funded through BMK, the Belgian Science Policy, the Canadian Euclid Consortium, the Deutsches Zentrum für Luft- und Raumfahrt, the DTU Space and the Niels Bohr Institute in Denmark, the French Centre National d'Etudes Spatiales, the Fundação para a Ciência e a Tecnologia, the Hungarian Academy of Sciences, the Ministerio de Ciencia, Innovación y Universidades, the National Aeronautics and Space Administration, the National Astronomical Observatory of Japan, the Netherlandse Onderzoekschool Voor Astronomie, the Norwegian Space Agency, the Research Council of Finland, the Romanian Space Agency, the State Secretariat for Education, Research, and Innovation (SERI) at the Swiss Space Office (SSO), and the United Kingdom Space Agency. A complete and detailed list is available on the *Euclid* web site (www.euclid-ec.org).

References

Asorey, J., Crocce, M., Gaztañaga, E., & Lewis, A. 2012, MNRAS, 427, 1891
Bacon, D. J., Refregier, A. R., & Ellis, R. S. 2000, MNRAS, 318, 625
Baldauf, T., Seljak, U., Smith, R. E., Hamaus, N., & Desjacques, V. 2013, Phys. Rev. D, 88, 083507
Bird, S., Viel, M., & Haehnelt, M. G. 2012, MNRAS, 420, 2551
Bridle, S. & King, L. 2007, New J. Phys., 9, 444
Camera, S., Fonseca, J., Maartens, R., & Santos, M. G. 2018, MNRAS, 481, 1251
Chevallier, M. & Polarski, D. 2001, Int. J. Mod. Phys., D, 10, 213
Cropper, M., Pottinger, S., Niemi, S., et al. 2016, in Society of Photo-Optical Instrumentation Engineers (SPIE) Conference Series, Vol. 9904, Space Telescopes and Instrumentation 2016: Optical, Infrared, and Millimeter Wave, ed. H. A. MacEwen, G. G. Fazio, M. Lystrup, N. Batalha, N. Siegler, & E. C. Tong, 99040Q
Dournac, F. et al. 2024, A&A, 690, A30
Eriksen, M. & Gaztanaga, E. 2015, MNRAS, 452, 2149
Euclid Collaboration: Blanchard, A. et al. 2020, A&A, 642, A191
Euclid Collaboration: Cropper, M. et al. 2024, arXiv:2405.13492
Euclid Collaboration: Jahnke, K. et al. 2024, arXiv:2405.13493
Euclid Collaboration: Mellier, Y. et al. 2024, arXiv:2405.13491
Fang, X., Krause, E., Eifler, T., & MacCrann, N. 2020, JCAP, 05, 010
Grasshorn Gebhardt, H. S. & Jeong, D. 2020, Phys. Rev. D, 102, 083521
Gupta A. K., N. D. K. 2000, Matrix Variate Distributions (Chapman & Hall)
Jain, B. & Taylor, A. 2003, Phys. Rev. Lett., 91, 141302
Joachimi, B., Cacciato, M., Kitching, T. D., et al. 2015, Space Sci. Rev., 193, 1
Joachimi, B. et al. 2021, A&A, 646, A129
Johnson, A. et al. 2017, MNRAS, 465, 4118
Joudaki, S. et al. 2018, MNRAS, 474, 4894
Kaiser, N. 1992, ApJ, 388, 272
Kaiser, N., Wilson, G., & Luppino, G. A. 2000, arXiv:0003338
Kiessling, A., Cacciato, M., Joachimi, B., et al. 2015, Space Sci. Rev., 193, 67, [Erratum: Space Sci.Rev. 193, 137 (2015)]
Kirk, D., Brown, M. L., Hoekstra, H., et al. 2015, Space Sci. Rev., 193, 139
Kitching, T. D., Alsing, J., Heavens, A. F., et al. 2017, MNRAS, 469, 2737
Krause, E., Eifler, T., Zuntz, J., et al. 2017, arXiv:1706.09359
Lacasa, F. & Grain, J. 2019, A&A, 624, A61
Laureijs, R., Amiaux, J., Arduini, S., et al. 2011, arXiv:1110.3193
Lemos, P., Challinor, A., & Efstathiou, G. 2017, JCAP, 05, 014

Linder, E. V. 2002, Phys. Rev. Lett., 90, 4
Loureiro, A. et al. 2019, MNRAS, 485, 326
Maciaszek, T., Ealet, A., Gillard, W., et al. 2022, in Society of Photo-Optical Instrumentation Engineers (SPIE) Conference Series, Vol. 12180, Space Telescopes and Instrumentation 2022: Optical, Infrared, and Millimeter Wave, ed. L. E. Coyle, S. Matsuura, & M. D. Perrin, 121801K
Newman, J. A. 2008, ApJ, 684, 88
Nock, K., Percival, W. J., & Ross, A. J. 2010, MNRAS, 407, 520
Pozzetti, L., Hirata, C., Geach, J., et al. 2016, A&A, 590, A3
Stebbins, A. 1996, arXiv:9609149
Takahashi, R., Sato, M., Nishimichi, T., Taruya, A., & Oguri, M. 2012, ApJ, 761, 152
Taylor, P. L. & Markovič, K. 2022, Phys. Rev. D, 106, 063536
Taylor, P. L., Markovič, K., Pourtsidou, A., & Huff, E. 2022, Phys. Rev. D, 105, 084007

[1] Dipartimento di Fisica, Università degli studi di Genova, and INFN-Sezione di Genova, via Dodecaneso 33, 16146, Genova, Italy
[2] INAF-IASF Milano, Via Alfonso Corti 12, 20133 Milano, Italy
[3] Dipartimento di Fisica, Università degli Studi di Torino, Via P. Giuria 1, 10125 Torino, Italy
[4] INFN-Sezione di Torino, Via P. Giuria 1, 10125 Torino, Italy
[5] INAF-Osservatorio Astrofisico di Torino, Via Osservatorio 20, 10025 Pino Torinese (TO), Italy
[6] Institut de Recherche en Astrophysique et Planétologie (IRAP), Université de Toulouse, CNRS, UPS, CNES, 14 Av. Edouard Belin, 31400 Toulouse, France
[7] Université de Genève, Département de Physique Théorique and Centre for Astroparticle Physics, 24 quai Ernest-Ansermet, CH-1211 Genève 4, Switzerland
[8] Institute of Space Sciences (ICE, CSIC), Campus UAB, Carrer de Can Magrans, s/n, 08193 Barcelona, Spain
[9] Institut d'Estudis Espacials de Catalunya (IEEC), Edifici RDIT, Campus UPC, 08860 Castelldefels, Barcelona, Spain
[10] INFN-Sezione di Genova, Via Dodecaneso 33, 16146, Genova, Italy
[11] Aix-Marseille Université, Université de Toulon, CNRS, CPT, Marseille, France
[12] Dipartimento di Fisica, Università di Genova, Via Dodecaneso 33, 16146, Genova, Italy
[13] INAF-Osservatorio Astronomico di Brera, Via Brera 28, 20122 Milano, Italy
[14] Dipartimento di Fisica, Sapienza Università di Roma, Piazzale Aldo Moro 2, 00185 Roma, Italy
[15] INAF-Osservatorio Astronomico di Roma, Via Frascati 33, 00078 Monteporzio Catone, Italy
[16] INFN-Sezione di Roma, Piazzale Aldo Moro, 2 - c/o Dipartimento di Fisica, Edificio G. Marconi, 00185 Roma, Italy
[17] Departamento de Física, FCFM, Universidad de Chile, Blanco Encalada 2008, Santiago, Chile
[18] Institut für Theoretische Physik, University of Heidelberg, Philosophenweg 16, 69120 Heidelberg, Germany
[19] Université St Joseph; Faculty of Sciences, Beirut, Lebanon
[20] School of Mathematics and Physics, University of Surrey, Guildford, Surrey, GU2 7XH, UK
[21] INAF-Osservatorio di Astrofisica e Scienza dello Spazio di Bologna, Via Piero Gobetti 93/3, 40129 Bologna, Italy
[22] SISSA, International School for Advanced Studies, Via Bonomea 265, 34136 Trieste TS, Italy
[23] INAF-Osservatorio Astronomico di Trieste, Via G. B. Tiepolo 11, 34143 Trieste, Italy
[24] INFN, Sezione di Trieste, Via Valerio 2, 34127 Trieste TS, Italy
[25] IFPU, Institute for Fundamental Physics of the Universe, via Beirut 2, 34151 Trieste, Italy
[26] Dipartimento di Fisica e Astronomia, Università di Bologna, Via Gobetti 93/2, 40129 Bologna, Italy
[27] INFN-Sezione di Bologna, Viale Berti Pichat 6/2, 40127 Bologna, Italy
[28] Max Planck Institute for Extraterrestrial Physics, Giessenbachstr. 1, 85748 Garching, Germany
[29] Universitäts-Sternwarte München, Fakultät für Physik, Ludwig-Maximilians-Universität München, Scheinerstr. 1, 81679 München, Germany
[30] Institut de Physique Théorique, CEA, CNRS, Université Paris-Saclay 91191 Gif-sur-Yvette Cedex, France
[31] Institut d'Astrophysique de Paris, UMR 7095, CNRS, and Sorbonne Université, 98 bis boulevard Arago, 75014 Paris, France
[32] Department of Physics "E. Pancini", University Federico II, Via Cinthia 6, 80126, Napoli, Italy
[33] INAF-Osservatorio Astronomico di Capodimonte, Via Moiariello 16, 80131 Napoli, Italy
[34] INFN section of Naples, Via Cinthia 6, 80126, Napoli, Italy
[35] Instituto de Astrofísica e Ciências do Espaço, Universidade do Porto, CAUP, Rua das Estrelas, PT4150-762 Porto, Portugal
[36] Institut de Física d'Altes Energies (IFAE), The Barcelona Institute of Science and Technology, Campus UAB, 08193 Bellaterra (Barcelona), Spain
[37] Port d'Informació Científica, Campus UAB, C. Albareda s/n, 08193 Bellaterra (Barcelona), Spain
[38] Institute for Theoretical Particle Physics and Cosmology (TTK), RWTH Aachen University, 52056 Aachen, Germany
[39] Dipartimento di Fisica e Astronomia "Augusto Righi" - Alma Mater Studiorum Università di Bologna, via Piero Gobetti 93/2, 40129 Bologna, Italy
[40] European Space Agency/ESTEC, Keplerlaan 1, 2201 AZ Noordwijk, The Netherlands
[41] Institute Lorentz, Leiden University, Niels Bohrweg 2, 2333 CA Leiden, The Netherlands
[42] Institute for Astronomy, University of Hawaii, 2680 Woodlawn Drive, Honolulu, HI 96822, USA
[43] Dipartimento di Fisica e Astronomia "Augusto Righi" - Alma Mater Studiorum Università di Bologna, Viale Berti Pichat 6/2, 40127 Bologna, Italy
[44] Instituto de Astrofísica de Canarias, E-38205 La Laguna, Tenerife, Spain
[45] Institute for Astronomy, University of Edinburgh, Royal Observatory, Blackford Hill, Edinburgh EH9 3HJ, UK
[46] Jodrell Bank Centre for Astrophysics, Department of Physics and Astronomy, University of Manchester, Oxford Road, Manchester M13 9PL, UK
[47] European Space Agency/ESRIN, Largo Galileo Galilei 1, 00044 Frascati, Roma, Italy
[48] ESAC/ESA, Camino Bajo del Castillo, s/n., Urb. Villafranca del Castillo, 28692 Villanueva de la Cañada, Madrid, Spain
[49] Université Claude Bernard Lyon 1, CNRS/IN2P3, IP2I Lyon, UMR 5822, Villeurbanne, F-69100, France
[50] Aix-Marseille Université, CNRS, CNES, LAM, Marseille, France
[51] Institute of Physics, Laboratory of Astrophysics, Ecole Polytechnique Fédérale de Lausanne (EPFL), Observatoire de Sauverny, 1290 Versoix, Switzerland
[52] UCB Lyon 1, CNRS/IN2P3, IUF, IP2I Lyon, 4 rue Enrico Fermi, 69622 Villeurbanne, France
[53] Institut de Ciencies de l'Espai (IEEC-CSIC), Campus UAB, Carrer de Can Magrans, s/n Cerdanyola del Vallés, 08193 Barcelona, Spain
[54] Mullard Space Science Laboratory, University College London, Holmbury St Mary, Dorking, Surrey RH5 6NT, UK
[55] Departamento de Física, Faculdade de Ciências, Universidade de Lisboa, Edifício C8, Campo Grande, PT1749-016 Lisboa, Portugal
[56] Instituto de Astrofísica e Ciências do Espaço, Faculdade de Ciências, Universidade de Lisboa, Campo Grande, 1749-016 Lisboa, Portugal
[57] Department of Astronomy, University of Geneva, ch. d'Ecogia 16, 1290 Versoix, Switzerland
[58] INAF-Istituto di Astrofisica e Planetologia Spaziali, via del Fosso del Cavaliere, 100, 00100 Roma, Italy
[59] Université Paris-Saclay, CNRS, Institut d'astrophysique spatiale, 91405, Orsay, France
[60] Department of Physics, Oxford University, Keble Road, Oxford OX1 3RH, UK

[61] INFN-Padova, Via Marzolo 8, 35131 Padova, Italy
[62] Aix-Marseille Université, CNRS/IN2P3, CPPM, Marseille, France
[63] Université Paris-Saclay, Université Paris Cité, CEA, CNRS, AIM, 91191, Gif-sur-Yvette, France
[64] INFN-Bologna, Via Irnerio 46, 40126 Bologna, Italy
[65] Istituto Nazionale di Fisica Nucleare, Sezione di Bologna, Via Irnerio 46, 40126 Bologna, Italy
[66] INAF-Osservatorio Astronomico di Padova, Via dell'Osservatorio 5, 35122 Padova, Italy
[67] Dipartimento di Fisica "Aldo Pontremoli", Università degli Studi di Milano, Via Celoria 16, 20133 Milano, Italy
[68] INFN-Sezione di Milano, Via Celoria 16, 20133 Milano, Italy
[69] Institute of Theoretical Astrophysics, University of Oslo, P.O. Box 1029 Blindern, 0315 Oslo, Norway
[70] Jet Propulsion Laboratory, California Institute of Technology, 4800 Oak Grove Drive, Pasadena, CA, 91109, USA
[71] Department of Physics, Lancaster University, Lancaster, LA1 4YB, UK
[72] von Hoerner & Sulger GmbH, Schlossplatz 8, 68723 Schwetzingen, Germany
[73] Technical University of Denmark, Elektrovej 327, 2800 Kgs. Lyngby, Denmark
[74] Cosmic Dawn Center (DAWN), Denmark
[75] Université Paris-Saclay, CNRS/IN2P3, IJCLab, 91405 Orsay, France
[76] Centre National d'Etudes Spatiales – Centre spatial de Toulouse, 18 avenue Edouard Belin, 31401 Toulouse Cedex 9, France
[77] Max-Planck-Institut für Astronomie, Königstuhl 17, 69117 Heidelberg, Germany
[78] Department of Physics and Astronomy, University College London, Gower Street, London WC1E 6BT, UK
[79] Department of Physics and Helsinki Institute of Physics, Gustaf Hällströmin katu 2, University of Helsinki, 00014 Helsinki, Finland
[80] Department of Physics, P.O. Box 64, University of Helsinki, 00014 Helsinki, Finland
[81] Helsinki Institute of Physics, Gustaf Hällströmin katu 2, University of Helsinki, 00014 Helsinki, Finland
[82] NOVA optical infrared instrumentation group at ASTRON, Oude Hoogeveensedijk 4, 7991PD, Dwingeloo, The Netherlands
[83] Centre de Calcul de l'IN2P3/CNRS, 21 avenue Pierre de Coubertin 69627 Villeurbanne Cedex, France
[84] Universität Bonn, Argelander-Institut für Astronomie, Auf dem Hügel 71, 53121 Bonn, Germany
[85] Department of Physics, Institute for Computational Cosmology, Durham University, South Road, Durham, DH1 3LE, UK
[86] Université Paris Cité, CNRS, Astroparticule et Cosmologie, 75013 Paris, France
[87] Institut d'Astrophysique de Paris, 98bis Boulevard Arago, 75014, Paris, France
[88] School of Mathematics, Statistics and Physics, Newcastle University, Herschel Building, Newcastle-upon-Tyne, NE1 7RU, UK
[89] Department of Physics and Astronomy, University of Aarhus, Ny Munkegade 120, DK-8000 Aarhus C, Denmark
[90] Waterloo Centre for Astrophysics, University of Waterloo, Waterloo, Ontario N2L 3G1, Canada
[91] Department of Physics and Astronomy, University of Waterloo, Waterloo, Ontario N2L 3G1, Canada
[92] Perimeter Institute for Theoretical Physics, Waterloo, Ontario N2L 2Y5, Canada
[93] Space Science Data Center, Italian Space Agency, via del Politecnico snc, 00133 Roma, Italy
[94] Institute of Space Science, Str. Atomistilor, nr. 409 Măgurele, Ilfov, 077125, Romania
[95] Universidad de La Laguna, Dpto. Astrofísica, E-38206 La Laguna, Tenerife, Spain
[96] Dipartimento di Fisica e Astronomia "G. Galilei", Università di Padova, Via Marzolo 8, 35131 Padova, Italy
[97] Universität Innsbruck, Institut für Astro- und Teilchenphysik, Technikerstr. 25/8, 6020 Innsbruck, Austria
[98] Satlantis, University Science Park, Sede Bld 48940, Leioa-Bilbao, Spain
[99] Centro de Investigaciones Energéticas, Medioambientales y Tecnológicas (CIEMAT), Avenida Complutense 40, 28040 Madrid, Spain
[100] Instituto de Astrofísica e Ciências do Espaço, Faculdade de Ciências, Universidade de Lisboa, Tapada da Ajuda, 1349-018 Lisboa, Portugal
[101] Niels Bohr Institute, University of Copenhagen, Jagtvej 128, 2200 Copenhagen, Denmark
[102] Cosmic Dawn Center (DAWN)
[103] Universidad Politécnica de Cartagena, Departamento de Electrónica y Tecnología de Computadoras, Plaza del Hospital 1, 30202 Cartagena, Spain
[104] Kapteyn Astronomical Institute, University of Groningen, PO Box 800, 9700 AV Groningen, The Netherlands
[105] Infrared Processing and Analysis Center, California Institute of Technology, Pasadena, CA 91125, USA
[106] INAF, Istituto di Radioastronomia, Via Piero Gobetti 101, 40129 Bologna, Italy
[107] Astronomical Observatory of the Autonomous Region of the Aosta Valley (OAVdA), Loc. Lignan 39, I-11020, Nus (Aosta Valley), Italy
[108] Center for Computational Astrophysics, Flatiron Institute, 162 5th Avenue, 10010, New York, NY, USA
[109] School of Physics and Astronomy, Cardiff University, The Parade, Cardiff, CF24 3AA, UK
[110] ICL, Junia, Université Catholique de Lille, LITL, 59000 Lille, France
[111] ICSC - Centro Nazionale di Ricerca in High Performance Computing, Big Data e Quantum Computing, Via Magnanelli 2, Bologna, Italy
[112] Instituto de Física Teórica UAM-CSIC, Campus de Cantoblanco, 28049 Madrid, Spain
[113] CERCA/ISO, Department of Physics, Case Western Reserve University, 10900 Euclid Avenue, Cleveland, OH 44106, USA
[114] Laboratoire Univers et Théorie, Observatoire de Paris, Université PSL, Université Paris Cité, CNRS, 92190 Meudon, France
[115] Dipartimento di Fisica e Scienze della Terra, Università degli Studi di Ferrara, Via Giuseppe Saragat 1, 44122 Ferrara, Italy
[116] Istituto Nazionale di Fisica Nucleare, Sezione di Ferrara, Via Giuseppe Saragat 1, 44122 Ferrara, Italy
[117] Dipartimento di Fisica - Sezione di Astronomia, Università di Trieste, Via Tiepolo 11, 34131 Trieste, Italy
[118] Minnesota Institute for Astrophysics, University of Minnesota, 116 Church St SE, Minneapolis, MN 55455, USA
[119] Université Côte d'Azur, Observatoire de la Côte d'Azur, CNRS, Laboratoire Lagrange, Bd de l'Observatoire, CS 34229, 06304 Nice cedex 4, France
[120] Department of Physics & Astronomy, University of California Irvine, Irvine CA 92697, USA
[121] Department of Astronomy & Physics and Institute for Computational Astrophysics, Saint Mary's University, 923 Robie Street, Halifax, Nova Scotia, B3H 3C3, Canada
[122] Departamento Física Aplicada, Universidad Politécnica de Cartagena, Campus Muralla del Mar, 30202 Cartagena, Murcia, Spain
[123] Institute of Cosmology and Gravitation, University of Portsmouth, Portsmouth PO1 3FX, UK
[124] Department of Computer Science, Aalto University, PO Box 15400, Espoo, FI-00 076, Finland
[125] Ruhr University Bochum, Faculty of Physics and Astronomy, Astronomical Institute (AIRUB), German Centre for Cosmological Lensing (GCCL), 44780 Bochum, Germany
[126] DARK, Niels Bohr Institute, University of Copenhagen, Jagtvej 155, 2200 Copenhagen, Denmark
[127] Department of Physics and Astronomy, Vesilinnantie 5, University of Turku, 20014 Turku, Finland
[128] Serco for European Space Agency (ESA), Camino bajo del Castillo, s/n, Urbanizacion Villafranca del Castillo, Villanueva de la Cañada, 28692 Madrid, Spain

[129] ARC Centre of Excellence for Dark Matter Particle Physics, Melbourne, Australia
[130] Centre for Astrophysics & Supercomputing, Swinburne University of Technology, Hawthorn, Victoria 3122, Australia
[131] W.M. Keck Observatory, 65-1120 Mamalahoa Hwy, Kamuela, HI, USA
[132] School of Physics and Astronomy, Queen Mary University of London, Mile End Road, London E1 4NS, UK
[133] Department of Physics and Astronomy, University of the Western Cape, Bellville, Cape Town, 7535, South Africa
[134] ICTP South American Institute for Fundamental Research, Instituto de Física Teórica, Universidade Estadual Paulista, São Paulo, Brazil
[135] Oskar Klein Centre for Cosmoparticle Physics, Department of Physics, Stockholm University, Stockholm, SE-106 91, Sweden
[136] Astrophysics Group, Blackett Laboratory, Imperial College London, London SW7 2AZ, UK
[137] Univ. Grenoble Alpes, CNRS, Grenoble INP, LPSC-IN2P3, 53, Avenue des Martyrs, 38000, Grenoble, France
[138] INAF-Osservatorio Astrofisico di Arcetri, Largo E. Fermi 5, 50125, Firenze, Italy
[139] Centro de Astrofísica da Universidade do Porto, Rua das Estrelas, 4150-762 Porto, Portugal
[140] Dipartimento di Fisica, Università di Roma Tor Vergata, Via della Ricerca Scientifica 1, Roma, Italy
[141] INFN, Sezione di Roma 2, Via della Ricerca Scientifica 1, Roma, Italy
[142] Department of Astrophysics, University of Zurich, Winterthurerstrasse 190, 8057 Zurich, Switzerland
[143] Theoretical astrophysics, Department of Physics and Astronomy, Uppsala University, Box 516, 751 37 Uppsala, Sweden
[144] Department of Astrophysical Sciences, Peyton Hall, Princeton University, Princeton, NJ 08544, USA
[145] Center for Cosmology and Particle Physics, Department of Physics, New York University, New York, NY 10003, USA

Appendix A: Details of the cross-covariance

There are three possible angular power spectra that can be constructed from two probes A and B:

- auto power spectrum of A, $C^{\rm AA}(\ell)$;
- auto power spectrum of B, $C^{\rm BB}(\ell)$;
- cross power spectrum between A and B, $C^{\rm AB}(\ell)$.

As a concrete example, consider A = $\rm GC_{ph}$ and B = WL.

Combining $\rm GC_{ph}$ *and* WL *as independent probes* When assuming $\rm GC_{ph}$ and WL to be independent, the resulting Fisher matrix will be given by the sum of the Fishers of the two single probes. According to the conventions explained in Sect. 3.2, the resulting Fisher is denoted as [$\rm GC_{ph}$]+[WL]. This case is equivalent to building a data-vector including the two auto-correlations

$$\mathbf{C}(\ell) = \left\{\mathbf{C}^{\rm phph}(\ell), \mathbf{C}^{\rm wlwl}(\ell)\right\} \,. \tag{A.1}$$

and setting to zero the off-diagonal blocks of the associated covariance matrix

$$\begin{aligned}&{\rm Cov}\left[\mathbf{C}(\ell), \mathbf{C}(\ell)\right] = \\ &\begin{pmatrix} {\rm Cov}\left[\mathbf{C}^{\rm phph}(\ell), \mathbf{C}^{\rm phph}(\ell)\right] & 0 \\ 0 & {\rm Cov}\left[\mathbf{C}^{\rm wlwl}(\ell), \mathbf{C}^{\rm wlwl}(\ell)\right] \end{pmatrix} .\end{aligned} \tag{A.2}$$

This is equivalent to neglecting the cross-covariance between the auto-correlations of the two single probes, which is given by the block

$${\rm Cov}\left[\mathbf{C}^{\rm phph}(\ell), \mathbf{C}^{\rm wlwl}(\ell)\right] \,.$$

Since the matrix in Eq. (A.2) is block diagonal, its inverse is of the same form:

$$\begin{pmatrix} A & 0 \\ 0 & B \end{pmatrix}^{-1} = \begin{pmatrix} A^{-1} & 0 \\ 0 & B^{-1} \end{pmatrix} . \tag{A.3}$$

Therefore the matrix product entering the Fisher matrix element is simply given by the bilinear form between $(\mathbf{C}^{\rm phph}(\ell)_{,\alpha}, \mathbf{C}^{\rm wlwl}(\ell)_{,\alpha})^{\rm T}$ and a block-diagonal covariance matrix, whose diagonal blocks are ${\rm Cov}\left[\mathbf{C}^{\rm phph}(\ell), \mathbf{C}^{\rm phph}(\ell)\right]^{-1}$ and ${\rm Cov}\left[\mathbf{C}^{\rm wlwl}(\ell), \mathbf{C}^{\rm wlwl}(\ell)\right]^{-1}$. The resulting Fisher matrix element is

$$\begin{aligned} F_{\alpha\beta}^{\rm GC_{ph}+WL}(\ell) &= \left[\mathbf{C}^{\rm phph}(\ell)_{,\alpha}\right]^T \, {\rm Cov}\left[\mathbf{C}^{\rm phph}(\ell), \mathbf{C}^{\rm phph}(\ell)\right]^{-1} \, \mathbf{C}^{\rm phph}(\ell)_{,\beta} \\ &+ \left[\mathbf{C}^{\rm wlwl}(\ell)_{,\alpha}\right]^T \, {\rm Cov}\left[\mathbf{C}^{\rm wlwl}(\ell), \mathbf{C}^{\rm wlwl}(\ell)\right]^{-1} \, \mathbf{C}^{\rm wlwl}(\ell)_{,\beta} \\ &= F_{\alpha\beta}^{\rm GC_{ph}}(\ell) + F_{\alpha\beta}^{\rm WL}(\ell) \,. \end{aligned} \tag{A.4}$$

which is the simple sum of the fisher elements associated with the single probes.

Combining $\rm GC_{ph}$ *and* WL *with cross-covariance* The Fisher matrix in this case is denoted as [$\rm GC_{ph}$ + WL]. The data-vector is the same as the previous one (Eq. A.1), but the off-diagonal blocks of the covariance matrix are taken into account

$$\begin{aligned}&{\rm Cov}\left[\mathbf{C}(\ell), \mathbf{C}(\ell)\right] = \\ &\begin{pmatrix} {\rm Cov}\left[\mathbf{C}^{\rm phph}(\ell), \mathbf{C}^{\rm phph}(\ell)\right] & {\rm Cov}\left[\mathbf{C}^{\rm phph}(\ell), \mathbf{C}^{\rm wlwl}(\ell)\right] \\ {\rm Cov}\left[\mathbf{C}^{\rm wlwl}(\ell), \mathbf{C}^{\rm phph}(\ell)\right] & {\rm Cov}\left[\mathbf{C}^{\rm wlwl}(\ell), \mathbf{C}^{\rm wlwl}(\ell)\right] \end{pmatrix} .\end{aligned} \tag{A.5}$$

This matrix is not block-diagonal, hence, when inverting it, the blocks will mix with each other. There exist some formulas based on the Schur complement (Gupta A. K. 2000) for the inverse of a 2×2 block matrix, but writing it down does not help to enlighten what happens in this case. From an intuitive point of view, the cross-covariance between two observables should worsen the constraints with respect to combining the two probes as independent. This can be understood with the following argument. If two observables exhibit a non-zero cross-covariance, there will be a mutual correlation between the two. In particular, a change in one of the two – for example induced by a variation of the cosmological parameters – will statistically induce a corresponding variation in the other. This in turn means that the two observables will share an amount of cosmological information, and therefore the total information coming from their combination will be less than the direct sum of the two pieces of information carried individually by the two of them.

Combining $\rm GC_{ph}$, WL *and their cross-correlation* Here both the covariance and the cross-correlation between $\rm GC_{ph}$ and WL are taken into account. The resulting Fisher matrix is denoted as [$\rm GC_{ph}$ + WL + XC($\rm GC_{ph}$, WL)], and the data-vector includes accordingly the maximal set of the available $C(\ell)$'s

$$\mathbf{C}(\ell) = \left\{\mathbf{C}^{\rm phph}(\ell), \mathbf{C}^{\rm phwl}(\ell), \mathbf{C}^{\rm wlwl}(\ell)\right\} \,, \tag{A.6}$$

and the covariance is the full 3×3 block matrix associated with this data-vector has the following entries

$$\begin{aligned}
{\rm Cov}\left[\mathbf{C}(\ell), \mathbf{C}(\ell)\right]_{11} &= {\rm Cov}\left[\mathbf{C}^{\rm phph}(\ell), \mathbf{C}^{\rm phph}(\ell)\right] \\
{\rm Cov}\left[\mathbf{C}(\ell), \mathbf{C}(\ell)\right]_{12} &= {\rm Cov}\left[\mathbf{C}^{\rm phph}(\ell), \mathbf{C}^{\rm phwl}(\ell)\right] \\
{\rm Cov}\left[\mathbf{C}(\ell), \mathbf{C}(\ell)\right]_{12} &= {\rm Cov}\left[\mathbf{C}^{\rm phph}(\ell), \mathbf{C}^{\rm wlwl}(\ell)\right] \\
{\rm Cov}\left[\mathbf{C}(\ell), \mathbf{C}(\ell)\right]_{22} &= {\rm Cov}\left[\mathbf{C}^{\rm phwl}(\ell), \mathbf{C}^{\rm phwl}(\ell)\right] \\
{\rm Cov}\left[\mathbf{C}(\ell), \mathbf{C}(\ell)\right]_{13} &= {\rm Cov}\left[\mathbf{C}^{\rm phwl}(\ell), \mathbf{C}^{\rm wlwl}(\ell)\right] \\
{\rm Cov}\left[\mathbf{C}(\ell), \mathbf{C}(\ell)\right]_{33} &= {\rm Cov}\left[\mathbf{C}^{\rm wlwl}(\ell), \mathbf{C}^{\rm wlwl}(\ell)\right] \,.
\end{aligned} \tag{A.7}$$

In this case the new information coming from the cross-correlation is added to the data-vector, and this contribution is expected to tighten the resulting constraints with respect to the uncorrelated sum. In particular, the cross-correlation is itself a function of the cosmological parameters, meaning that its value is be sensitive to a variation of the parameters themselves. In this sense it is said that adding the cross-correlation signal is expected to provide more cosmological information, therefore improving the combined constraints. On the other hand, also all the cross-covariances between the $C(\ell)$'s are being considered in this case, and this tends to worsen the constraints, as explained in the previous paragraph. So there are two concurring effects, and in principle it is not obvious which of the two is dominant. The forecasts performed in this work show that the tightest constraints are actually obtained when both the cross-covariance and cross-correlation are included.

Appendix A.1: Hybrid approach cross-covariance

The hybrid approach is equivalent to using the data vector

$$\mathbf{D} = \left\{\mathbf{C}^{\mathrm{phsp}}(\ell_1, \ldots, \ell_N),\, \mathbf{C}^{\mathrm{phsp}}(\ell_1, \ldots, \ell_N),\, \mathrm{GC}_{\mathrm{sp}}(P_k)\right\} , \tag{A.8}$$

and computing the Fisher matrix with Eq. (22) by using a covariance matrix that can be symbolically written as

$$\begin{pmatrix} \mathrm{Cov}\,[\mathrm{phph}, \mathrm{phph}] & \mathrm{Cov}\,[\mathrm{phph}, \mathrm{phsp}] & 0 \\ \mathrm{Cov}\,[\mathrm{phsp}, \mathrm{phph}] & \mathrm{Cov}\,[\mathrm{phsp}, \mathrm{phsp}] & 0 \\ 0 & 0 & \mathrm{Cov}\,[\mathrm{spsp}, \mathrm{spsp}] \end{pmatrix} . \tag{A.9}$$

The upper left 2×2 sector contains the covariances between the elements of the $C^{\mathrm{phph}}(\ell)$ and $C^{\mathrm{phsp}}(\ell)$ matrices, organized in block-diagonal form for all multipoles as in Eq. (27). Analogously, the lower right corner block represents the auto-covariance of the spectroscopic galaxy Fourier power spectrum for all wave-numbers and redshifts considered. The zeroes correspond to the elements containing the unknown covariances between the 2D and 3D power spectra, which are therefore neglected.

Dear Editor and Referee,

thank you for the time spent reading our manuscript. Here is a list of the comments from the referee with the relative answer. When there was a major change to tha paper text, we have added the new sentence here as well. All changes have been highlighted in a latex-diff.pdf we have uploaded. We think that we have answered to all the points from the referee.
Thanks again for your time,
Marco Bonici (on behalf of the authors)

Dear Editor and Authors,

I finished reading the manuscript "Euclid preparation: 6×2pt analysis of Euclid's spectroscopic and photometric data sets". This paper is a natural continuation of the Fisher matrix analysis of the Euclid paper EP-VII by considering in a consistent way the cross-correlation and cross-covariance contributions of the galaxy clustering spectroscopic sample (GCsp) with the photometric galaxy clustering (GCph) and weak lensing (WL) observables coming from the traditional 3x2pt (GCph, WL and cross-correlation of the two) analysis. It also agrees with the findings of alternative aproaches in the literature like the Taylor & Markovic 2022, where it was shown that the cross-covariances between spectroscopic and photometric data are negligible. In detail, the main focus of the paper here is to study the combination of the GCsp sample on top of the 3x2pt in two new ways: One is the harmonic 6x2pt, where the GCsp auto-correlation and the cross-correlation (GCsp+GCph) as well as the cross-correlation (GCsp+WL) is performed with the harmonic 2D spectrum. The second, a hybrid 6x2pt, is now keeping the cross-correlations (GCsp+GCph) and (GCsp+WL) in harmonic 2D space and just adding the GCsp auto-correlation as from the traditional 3D Fourier analysis, but now ignoring cross-covariances between 2D and 3D statistics. The authors have showed that in each of the two approaches the extra cross-correlations and cross-covariances are in any case negligible on the constraining power of the cosmological parameters. They have performed a case-by-case study on the various cross terms (correlations and covariances) and how they impact the Figure-of-Merit and the marginalized constraints of the parameters.
Overall, I would consider the manuscript well-written, original, and clear. However, I have attached a few minor comments that may help to strengthen the presentation of the manuscript. Therefore, I believe that this work warrants publication in the A&A journal once the authors make these minor revisions by addressing the comments below.

Please find below my comments on the manuscript.

Section 2:

1) Regarding equation 1 and 2: It would be better introduce the parameters w0, wa ,Omega_m, H0, h, ns, M_v in the main text rather than the in table caption.

Answer: as suggested I introduced the cosmological parameters right after Eq. 1 and referred to Table 1 for the fiducial values (after removing the reference to Omb and Omm in the caption).

2) Equation 6; Please, introduce 'c' as the speed of light, wavenumber 'k' and state that 'r(z)' is the radial comoving distance for a flat cosmology.

Answer: done as suggested.

Section 2.3:

3) In the paragraph following equation 17. It would be better to elaborate a bit on the reason why the RSD are not included in the harmonic space 2D spectrum of the GCsp. Although it is true that some RSD information is lost due to the line-of-sight integration in the projected 2D harmonic spectra, what is left could still be relevant for top-hat bins. This point, in fact, could be even more relevant especially in the case where more and thinner tomographic bins are considered (like 24 or 40).

Answer: The referee correctly pointed out that while some RSD information is lost due to line-of-sight integration in projected 2D harmonic spectra, the remaining signal could be relevant, particularly with thinner tomographic bins. So, although it is possible there is a signal we neglected, our approach is supported by two key considerations:

1. Taylor & Markovic (2022) conducted a similar analysis that included RSD and found results consistent with ours, suggesting that the omission of RSD does not significantly impact our main conclusions regarding the minimal effect of cross-covariances.
2. Our results on GCsp in harmonic space align with the IST:F forecasts for Euclid, which did include RSD, further corroborating our findings
3. It is possible to perform measurements by using the approach of Nock et al. 2010 (arxiv 1003.0896), by binning in apparent galaxy pair-centre rather than galaxy position. Such an approach would actually suppress the effect of RSDs, making our analysis way closer to the actual measurements.

We acknowledge that with thinner tomographic bins (such as 24 or 40 as you suggest), the relevance of RSD might increase. While we believe the signal loss in our current analysis is likely small, we recognize this as a limitation of our work. We plan to investigate this thoroughly in a follow-up study using simulations that include all relevant effects, which will allow us to quantify precisely any information gain from including RSD with varying bin widths.

We have added a sentence to the manuscript in the paragraph following Eq. (17) to clarify the reasoning behind omitting RSD and to acknowledge the referee's point about potential residual signal in thinner bins.

"While some residual RSD information could, in principle, remain in the projected 2D spectra, especially for thinner tomographic bins, we neglect RSD in this analysis; however, a previous study that included RSD found similar results~\citep{Taylor:2022rgy}, suggesting that any impact on our conclusions is minimal. Furthermore, if one were to carry a harmonic analysis for the GCsp sample as we suggest here, it is possible to make the measurement with an approach similar to Nock at al. 2010; such an approach reduces the RSD signal in the measured summary statistics, hence removing a possible mismatch between data and

modelling. We leave a detailed investigation of RSD effects to future work, which will leverage a dedicated suite of simulations incorporating all relevant observational effects.

Section 3:

4) Equation 2: The transpose symbol is needed on the data vector of the first derivative (left part).

Answer: added the transpose symbol as suggested

Section 3.1:

5) Table 4: In the Baseline GCsp the shot noise should refer to equation 37 and not equation 41.

Answer: corrected the reference in Table 4.

Section 5:

6) Paragraph 4: It would be nice to have also a plot of the alternative GCph binning with only 4 photometric bins.

Answer: we would prefer to avoid adding such a figure because the bins we are using for that scenario are simply a subset of the bins used for the other analysis (hence the plot would not add any additional information). For completeness, here is the plot that would be produced if we were tho show the alternative binning

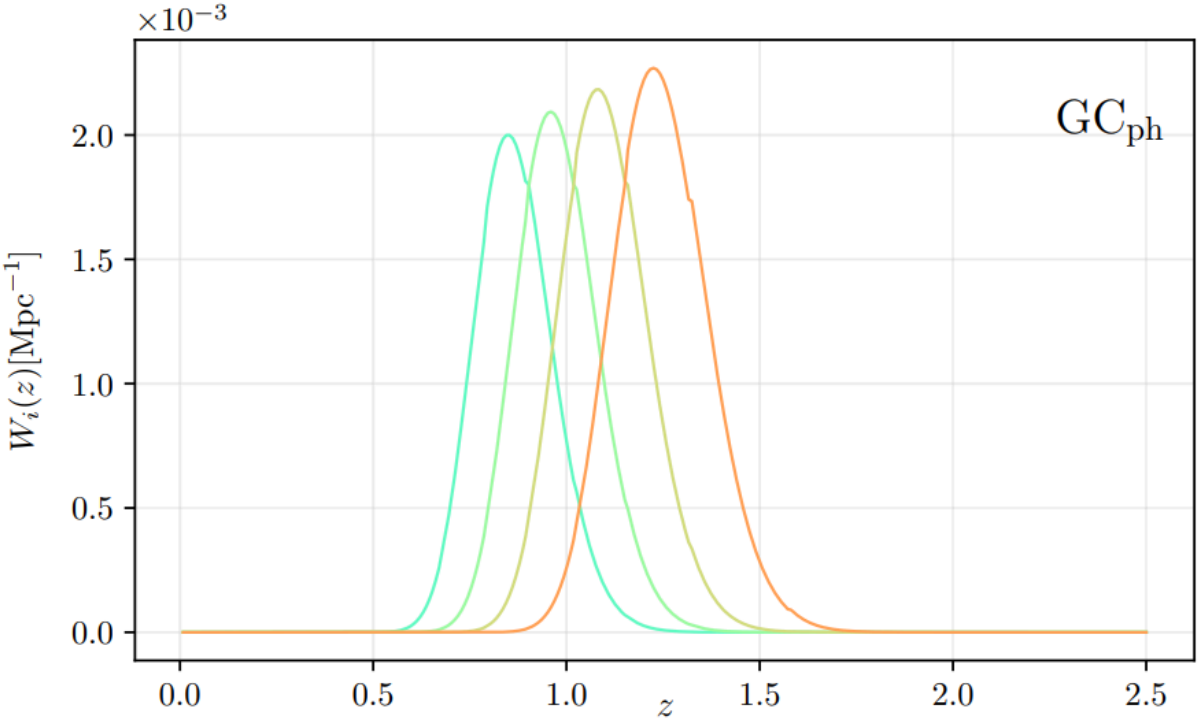

Section 4.1.1:

7) Fig.7 is mentioned in the text straight after Fig.2. I think it would be better if it was renamed as Fig.3 and then change the names of the rest of the figures accordingly.

Answer: as suggested from the referee, Fig. 7 was moved right after Fig. 2.

8) In the second paragraph of section 4.1.1 : It looks from Fig.7 that the [GCph + GCsp] Fisher matrix is shown with cyan and not blue and also [GCph] + [GCsp] with green and not cyan.

Answer: the referee is right, there is a mismatch between the used colors and the description in the text. The text has been corrected.

Section 4.1.2:

9) Line 7: Similarly to the previous point; It looks from Fig.7 that the [GCph + GCsp + XC(GCph , GCsp)] Fisher matrix is shown with orange and not green.

Answer: the referee is right, there is a mismatch between the used color and the description in the text. The text has been corrected.

10) Fig.4 caption mentions "baseline optimistic scenario" but the figure label says "Scenario: Pessimistic".

Answer: the referee is right. We fixed the figure label, which now correctly says “Scenario: optimistic”.

Section 4.1.3:

11) Paragraph second to last of 4.1.3: 'Figure 6 shows also the two probes in the baseline configuration,'. I see now that "figure" is now referred to as 'Figure' and not as 'Fig.' which is elsewhere. It should be homogenized.

Answer: corrected the notational inconsistency

Section 5.1:

12) In the second line 'Fig. 14' is mentioned however, 'Fig. 13' is never mentioned in the text before.

Answer: we have added a sentence referencing to Fig 13 before the one referencing to Fig. 14.
Finally, Fig. 13 shows a comparison between the harmonic and hybrid approach. As can be seen from the plot, when increasing the number of bins in the harmonic case, the constraints approach that of the hybrid case.

Section 5.2:

13) Page 19: "Figure 16 shows that when the independent combination..." Same thing about 'Fig.' and 'Figure' references. Please homogenize.

Answer: corrected the notational inconsistency

Section 5.2:
14) Page 20: Same thing about the 'Figure 17' reference.

Answer: corrected the notational inconsistency

Section 5.3:

15) Page 21: Same thing about the 'Figure 18' reference.

Answer: corrected the notational inconsistency

Section 6:

16) Page 22: Space needed in '3×2ptobservables'.

Answer: space added.

17) Caption of Fig. 19: 'The top panels refer to the optimistic scenario, while the bottom panels refer to the pessimistic one.' --> 'The left panels refer to the pessimistic scenario, while the right panels refer to the optimistic one.'

Answer: corrected the notational inconsistency